

OPTICAL IMAGING OF EMBRYONIC CARDIAC CONDUCTION

BY

PEI MA

Submitted in partial fulfillment of the requirements  
For the degree of Doctor of Philosophy

Dissertation Adviser: Andrew M. Rollins, Ph.D.

Department of Biomedical Engineering  
CASE WESTERN RESERVE UNIVERSITY

August, 2016

**CASE WESTERN RESERVE UNIVERSITY**  
**SCHOOL OF GRADUATE STUDIES**

We hereby approve the thesis/dissertation of

**Pei Ma**

candidate for the degree of **Doctor of Philosophy**.

Committee Chair

**Xin Yu**

Committee Member

**Andrew M. Rollins (Dissertation Adviser)**

Committee Member

**Kenneth D. Singer**

Committee Member

**Michiko Watanabe**

Committee Member

**Michael W. Jenkins**

Date of Defense

**Apr. 13<sup>th</sup> 2016**

\*We also certify that written approval has been obtained  
for any proprietary material contained therein.

## Table of Contents

List of Tables .....	7
List of Figures .....	8
Acknowledgements .....	15
List of Abbreviations .....	16
Abstract .....	17
<b>Chapter 1. Background</b> .....	<b>19</b>
1.1 CHDs and embryonic cardiovascular research .....	19
1.1.1 Fetal alcohol syndrome and the neural crest .....	20
1.1.2 Cardiac conduction system .....	22
1.1.3 The avian model .....	24
1.2 Optical mapping .....	24
1.2.1 Voltage-sensitive Fluorescence Dye .....	25
1.2.2 OM system .....	30
1.2.3 OM applications in the heart .....	32
1.2.3.1 OM of adult heart .....	33
1.2.3.2 OM of the developing heart .....	33
1.2.3.3 OM signal and image processing in cardiac applications .....	35
1.2.4 Current limitations of OM .....	36
1.2.4.1 Motion artifacts .....	36
1.2.4.2 Depth-resolved OM .....	37
1.2.5 Reliable pacing scheme .....	39
1.3 Optical coherence tomography .....	40

1.3.1 Michelson interferometer and time domain OCT .....	41
1.3.2 Fourier domain OCT .....	43
1.3.3 Doppler OCT .....	46
1.3.4 OCT in embryonic research .....	48
1.4 Light-sheet microscopy .....	50
1.4.1 3D fluorescence microscopy .....	51
1.4.2 Light-sheet microscopy concept and scheme .....	52
1.4.2.1 Illumination scheme .....	53
1.4.2.2 Detection scheme .....	54
1.4.2.3 Illumination-detection-coupled light-sheet microscopy .....	55
1.4.2.4 Advantages of light-sheet microscopy .....	56
1.4.3 Light sheet microscopy application in developmental biology .....	56
1.5 Aims of this dissertation .....	57
<b>Chapter 2. Integrated OM and OCT .....</b>	<b>59</b>
2.1 Introduction .....	59
2.2 Material and Methods .....	62
2.2.1 Embryonic heart preparation .....	62
2.2.2 Design of a compact OCT scanner .....	62
2.2.3 Integrated OCT/OM system .....	65
2.2.4 Image processing and data analysis .....	67
2.2.5 3D conduction velocity correction algorithm .....	68
2.2.6 Validation and Evaluation .....	70
2.3 Results .....	71

2.4 Discussion .....	77
<b>Chapter 3. 4D OM with Light-sheet Microscopy .....</b>	<b>84</b>
3.1 Introduction.....	84
3.2 Materials and Methods .....	86
3.2.1 Optical system .....	86
3.2.1.1 Illumination path .....	87
3.2.1.2 Detection path – Objective, tube lens and camera .....	89
3.2.1.3 Detection path – ETL .....	91
3.2.1.4 Optical pacing implementation .....	95
3.2.2 Sample preparation for OM experiments .....	96
3.2.3 4D data acquisition and image processing .....	96
3.3 Results of 4D OM .....	97
3.4 Discussion .....	100
<b>Chapter 4. Heart motion correction in OM using image registration .....</b>	<b>104</b>
4.1 Heart motion in OM .....	104
4.2 Image registration .....	105
4.3 Methods .....	107
4.3.1 Sample preparation .....	107
4.3.2 Image acquisition .....	107
4.3.3 Registration methods for time-series images .....	107
4.4 Results and discussion .....	110
<b>Chapter 5. Cardiac neural crest ablation model .....</b>	<b>114</b>
5.1. Introduction .....	114

5.2 Materials and Methods .....	117
5.2.1 Embryo preparation and CNCC ablation .....	117
5.2.2 Imaging and analysis of late-stage septated hearts .....	120
5.2.3 Structural and functional imaging of embryos at the cardiac looping stage ....	122
5.2.4 Statistical analysis .....	122
5.3. Results .....	123
5.3.1 Great vessel defects .....	123
5.3.2 Left atrioventricular valvular defects .....	126
5.3.3 Body flexure abnormalities at early stages .....	128
5.3.4 Abnormal flow at cardiac looping stages .....	130
5.3.5 Abnormal cardiac cushions at cardiac looping stages .....	132
5.3.6 Potential links between two early-stage defects .....	135
5.4. Discussion .....	136
<b>Chapter 6. Summary and future work .....</b>	<b>144</b>
6.1 Summary .....	144
6.2 Future work .....	147
6.2.1 4D OM in beating embryonic heart and <i>in vivo</i> OM .....	147
6.2.2 Software toolbox for 4D membrane potentials .....	151
6.2.3 Link 4D conduction maps with cardiac structures and gene expression .....	152
<b>Appendix A Movie Description .....</b>	<b>154</b>
<b>Appendix B Compact OCT scanner Part List .....</b>	<b>155</b>
<b>Appendix C Integrated OCT and OM Image Processing using MATLAB .....</b>	<b>160</b>
<b>Appendix D Light-sheet Microscopy System Part List .....</b>	<b>162</b>

<b>Appendix E Light-sheet OM Protocol .....</b>	<b>164</b>
<b>Bibliography .....</b>	<b>172</b>

## List of Tables

**Table 2.1** Modeling results from four settings of the resolution switchable scanner. (P. 64)

**Table 3.1** Resolution and FOV with different optical settings. (P. 91)

**Table 4.1** Conduction velocity measurements with and without motion correction. (P. 113)

**Table 5.1** A summary of operation, assay and post processing performed on a cohort of embryos for day 8 analysis and a cohort of embryos for day 3 analysis. (P. 121)

**Table 5.2** Day 8 (HH stage 34) Embryo Phenotypes. (P. 124)

**Table 5.3** Heart rate of the control and CNCC-ablated embryos were not significantly different. A significant portion of CNCC-ablated embryos present moderately-twisted body flexures or severely-twisted body flexures. (P. 129)

**Table 5.4** Analysis of cardiac cushion phenotypes including the gap phenotype between cushions at the AVJ and reduced outflow tract cushion coverage phenotype of the luminal surface. (P. 134)

**Table 5.5** Correlation between AV cushion gap and flow shoulder phenotype. (P. 136)

## List of Figures

**Fig. 1.1** Transitions of conduction pattern during cardiac development. A: uniform conduction at straight heart tube stage. B: the development of AV-delay and the slow-fast-slow conduction pattern at cardiac looping stage. C: base-to-apex conduction pattern during interventricular septation. D: apex-to-base conduction pattern due to the maturation of the His–Purkinje fibers. Figure adapted from Mikawa and Hurtado, 2007. (P. 23)

**Fig.1.2** Voltage-sensitive dye mechanism. A: electrochromic mechanism is based on Stark effect. The dye spectra shifts by a small amount when the membrane depolarizes. B: an example of spectra shift of electrochromic dyes. The spectra can represent excitation or emission spectra. Either one may represent before and after voltage changes. s1: spectrum 1, s2: spectrum 2. C: voltage-sensitive dye based on FRET mechanism. Distance between the two fluorophore changes as the membrane depolarizes therefore the intensity of collected signal is altered. D: PeT voltage-sensitive dyes have electron wires to transfer electron and quenches fluorescence. Depolarization decreases electron transfer rate therefore increases fluorescence. Redrawn and modified from Miller et al. 2007. (P. 28)

**Fig. 1.3** Schematic diagram of an OM system. (P. 31)

**Fig. 1.4** Integrated OM and OP. Fluorescence images, action potential recordings, activation maps and action potential duration maps are shown for examples of unpaced and paced 2-day and 5-day embryonic hearts. Adapted from Wang et al., 2014. (P. 40)

**Fig. 1.5** Michelson interferometer and TDOCT. (P. 42)

**Fig. 1.6** Beam scanning in OCT. A: collimated light is focused on the sample through an objective lens. The 3D relationship of A-scan, B-scan and volume-scan. B: An A-scan from the indicated location in a B-scan (red arrow in C). C: a B-scan of a dissected embryonic heart. The B-scan is from a slice in a volume scan of the heart at the indicated location in D. D: volume rendering of the embryonic heart. (P. 43)

**Fig. 1.7** Two variations of Fourier domain OCT: spectral domain OCT and swept source OCT. A: schematic diagram of a spectral domain OCT system. It uses a broadband light source, a spectrometer and a line scan camera. B: schematic diagram of a swept source OCT system. It uses a swept light source and a balanced detector. C: the Fourier relationship between spectral fringes and the spatial location of a scatterer. (P. 45)

**Fig. 1.8** Flow velocity and the Doppler shift. (P. 47)

**Fig. 1.9** Schematic diagram of light-sheet microscopy. A: orthogonal illumination and detection in light-sheet microscopy. Adapted from Huisken and Stainier, 2009. B: illumination and detection scheme in epi-fluorescence microscopy, LSCM, two-photon microscopy and light-sheet microscopy. Epi-fluorescence microscopy does not have sectioning ability therefore tissue has to be physically sectioned. LSCM offers optical sectioning by rejecting out of focus light. Two-photon microscopy provides optical sectioning through confining excitation only at the focus. Both LSCM and two-photon

microscopy require scanning for a line or a plane of image. Light-sheet microscopy achieves optical sectioning by only illuminating a plane at a time. No scanning is needed for 1D or 2D imaging. (P. 53)

**Fig. 2.1** A: compact scanner design in Zemax. B: point spread function modelled by Zemax (the 12  $\mu\text{m}$  resolution setting). 00: light beam centered.  $X \pm 2.4\text{mm}$ : scan in X direction.  $Y \pm 2.4\text{mm}$ : scan in Y direction. Scale bar: 12  $\mu\text{m}$  C: physical setup of the compact scanner. (P. 64)

**Fig. 2.2** An example image of beam profile analysis result acquired at the focus of the compact scanner (17  $\mu\text{m}$  resolution setting). The FWHM of the beam profile was highlighted with the red box. The beam profile was fitted to Gaussian profiles in two cross sections and ellipticity was reported in the figure. (P. 65)

**Fig. 2.3** A: schematic diagram of the integrated OCT/OM system. B: physical setup of the integrated system. LED: light-emitting diode. SLD: superluminescent diode. C: zoom in view of the red circle in B. A clear view of the integrated OCT and OM system arrangement near the sample. (P. 66)

**Fig. 2.4** Diagram illustrating velocity calculations with the traditional 2D projection method (top) and 3D corrected method (bottom). Fluorescent signals were collected from a 3D heart surface and projected to a 2D plane. This diagram uses a small  $3 \times 3$  patch on the heart surface to demonstrate the process. In the traditional 2D calculation, only velocity components in the projected plane ( $\overline{v}_x, \overline{v}_y$ ) were calculated. In the 3D corrected calculation, 3D structure was used to find the normal vector ( $\vec{n}$ ) by Newell's method. Then the velocity component in the height dimension ( $\overline{v}_z$ ) was calculated and finally 3D conduction velocity ( $\overline{v}_{3D}$ ) was computed. (P. 69)

**Fig. 2.5** OCT/OM registration. Panel A shows an OCT *en face* projection gray scale image of a HH stage 15 embryonic heart before being registered to an OM image. The green contour represents the boundary segmentation of the OCT *en face* projection and the magenta contour represents the boundary segmentation of the corresponding OM image overlaid on the OCT *en face* projection. Panel B shows an OM image which served as the reference for image registration. After registration, boundary contours of OCT (green) and OM (magenta) images can be seen to correspond well. (P. 71)

**Fig. 2.6** Results of OCT measuring various orientations of a flat surface using Newell's method. Standard deviation bars are shown inside the circles. (P. 72)

**Fig. 2.7** Panel A shows raw action potential traces of 3 different pixels from 3 different regions of the heart tube, indicated by arrows from panel B.  $\Delta F/F$  represents the percent change in raw fluorescence signals. The red dot in each trace represents the activation time. Panel B shows a 2D electrical activation map overlaid on a gray scale OM image. Colormap blue to red represents the sequence of activation from early to late. Each isochrone represents 10 milliseconds. Panel C shows the activation map overlaid on the 3D OCT volume surface rendering. This panel shares the same colormap as Panel B. av-atrioventricular junction; v-ventricle; ot-outflow tract. (P. 73)

**Fig. 2.8** Three embryonic hearts were imaged and processed. Panel A shows surface height maps acquired from OCT volume rendering. The relative height of each pixel in microns is represented by the colormap and each contour line represents 15  $\mu\text{m}$ . Panel B shows quiver maps of conduction direction through the hearts. Normalized and  $10 \times 10$  binned arrow heads indicate the directionality only. Panel C shows 3D-corrected conduction velocity maps overlaid on the surfaces of 3D OCT volume rendering. Panel D shows conduction velocity magnitude correction maps showing percent correction from the 2D values to the 3D corrected values. Panel E shows histograms of the necessary correction amount needed for each heart with bins of 5%. av- atrioventricular junction; v-ventricle; ot-outflow tract. (P. 75)

**Fig. 2.9** Panels A and B are 2D (uncorrected) and 3D-corrected conduction velocity maps, respectively, for embryonic heart 1. Square regions of interest from the inner (indicated in green) and outer (indicated in red) curvatures were selected for comparison. Panel C top and bottom are magnified, corresponding images of the AVJ from panels A and B. Panel D shows the averaged conduction velocity of the marked regions in panel C. The results are presented as mean  $\pm$  S.D. Conduction velocity values were compared using Student's t-test (\*  $p < 0.0001$ ). av- atrioventricular junction. (P. 76)

**Fig. 3.1** System setup diagram. Galvo: galvanometer mirror. OP: optical pacing. (P. 87)

**Fig. 3.2** Displacement of the light-sheet location after the cylindrical lens is proportional to the voltage applied on the galvo. (P. 88)

**Fig. 3.3** The left panel presents the method for calibrating the axial resolution of the light-sheet system. The phantom was moved across the light sheet with 1  $\mu\text{m}$  steps. A particle can only be light up when it is in the light-sheet illumination profile. The right panel shows the result of a calibration measurement. The total travel range of 100  $\mu\text{m}$  was interpolated from 100 to 1000 points. (P. 89)

**Fig. 3.4** Fluorescent images of HH stage 14 (A) and 19 (B) YFP quail embryonic hearts acquired using a light-sheet microscope (5X 0.25 NA, 200 mm tube lens). Magenta boarders: segmented heart tube. Yellow arrows: endocardium; green arrow: EMT cells. (P. 92)

**Fig. 3.5** The exact layout of the detection path of the light-sheet system. Because the ETL needs to be mounted horizontally, two mirrors cubes were used to reflect the optical path. Distances labelled between optical components indicate the length of light path at the optical axis. The numbers in green heptagons represent the order of alignment steps. The ETL should be adjusted multiple times to ensure it is centered between  $l_{r1}$  and  $l_{r2}$  and it is laterally centered with respect to the optical axis. The lateral adjustments corrects for the lateral shifts in images as  $1/f_{ETL}$  changes. The alignment step 5 ensures uniform magnification as  $1/f_{ETL}$  changes. (P. 93)

**Fig. 3.6** The linear relationship between the focal power of the ETL and the displacement of image plane. (P. 93)

**Fig. 3.7** Rigid image registration as a metric for optimizing ETL locations. A and B are images acquired under different settings of ETL focal power. A was registered to B. The lateral shifts in both directions can be observed in the dashed-line red boxes. C and D are merging results of A and B displayed using checkerboards. There is no obvious misalignment in the merging results. (P. 94)

**Fig. 3.8** ETL optimization examples. Top panels are before and after an adjustment for correcting magnification. Bottom panels are before and after corrections of lateral shifts of the ETL. Images acquired at different focal power settings were registered to the image at focal power=2.5. Both parameters were reduced after adjustments. (P. 94)

**Fig. 3.9** OM recordings with optically paced heart. The left panel shows a brightfield image of the pacing fiber (pointed by the red arrow) placed on an embryonic heart. The middle panel shows the fluorescence image of another heart. The right panel shows the traces from the selected pixel in the middle panel, labelled with a green dot on the left panel. The intrinsic rate of the heart was approximately 36 beats per minute, and it was paced at 1 Hz. The recording shows a 6 s time period (3000 frames) and the action potentials shows exact 1 Hz. (P. 95)

**Fig. 3.10** Panel A is a fluorescence image of an embryonic heart with voltage-sensitive dye staining. b, c and d are pixels which traces are plotted in B, C and D respectively. Intensity values were normalized. myo: myocardium; endo: endocardium. (P. 98)

**Fig. 3.11** 4D transmembrane potentials shown in 3D and three orthogonal planes. Colored activation wave is overlaid on grayscale heart tube volume reconstruction or cross sectional images. A, E, I, M are 3D transmembrane potential volumes at 0.28s, 0.38s, 0.48s and 0.58s respectively and the locations of the three orthogonal planes are indicated these panels. B, F, J and N are xy-planes at corresponding time points. C, G, K and O are xz-plane at corresponding time points. D, H, L and P are yz-planes at corresponding time points. (P. 99)

**Fig. 3.12** 3D activation map of two HH stage 14 embryonic hearts. (P. 100)

**Fig. 3.13** Projected 2D activation maps from two HH stage 14 embryonic hearts. (P. 100)

**Fig. 3.14** Comparison of SNR between di-4-ANEPPS and FluoVolt. A and E are fluorescence images from two embryos that were stained with each dye. B and F are two representative action potential traces from each example. C and G are SNR maps of the entire hearts. D and H are isochrone maps calculated from each example without any filtering. (P. 102)

**Fig. 4.1** Schematic diagram of multiple-image registration methods. (P. 109)

**Fig. 4.2** An image before and after registration. A and B: the same image before and after registering to a reference frame. C and D: the initial grid and the deformed grid after registration. (P. 110)

**Fig. 4.3** Representative action potential traces before and after motion correction. Blue action potential traces are from OM recordings with motion. Red action potential traces are from key-frame corrected dataset. (P. 111)

**Fig. 4.4** Activation maps of OM recordings with and without motion correction. A: no motion suppression or correction was applied. B: motion eliminated with cytoD. C: motion corrected with first-ref method. D: motion corrected with mid-frame method. E: motion corrected with key-frame method. (P. 112)

**Fig 5.1** CNCC ablation setup diagram. Two thick red lines on the embryo indicate the ablation region, which is from the mid-otic placode to somite 3. FOV: field of view. Microscope FOV is 1.5 mm × 1.5 mm. S1: somite 1. (P. 119)

**Fig. 5.2** A: a bright field image of a HH stage 9 embryo immediately after its CNCCs were ablated. The embryo was stained with neutral red before ablation. S1, 2, 3: somite 1, 2, 3. B: a fluorescent image of the same area as panel A with propidium iodide staining to assess cell viability after CNCC ablation of both sides of the neural folds. (P. 119)

**Fig 5.3** Example of great vessel measurement on a control embryo. A: 3D volume reconstruction image of a sham control embryo. An orthogonal slice cut through the great vessels in this panel indicates a cross-sectional image that was used to measure the great vessel diameters. B: the orthogonal slice in A. The outer diameters of the great vessels are very close to a circular shape. Red double head arrow: great vessel measurements. C and D are images showing the great vessels at different locations in the heart. C shows the proximal end of the great vessels. The aortic and pulmonary trunk are present. D shows a location that the LBA just branched off the aortic trunk. RBA: right brachiocephalic artery, LBA: left brachiocephalic artery, AA: aortic arch, RPA: right pulmonary artery, LPA: left pulmonary artery. LV: left ventricle, RV: right ventricle. (P. 121)

**Fig. 5.4** An example of a heart with PTA. A and B: heart cross sectional images of the chamber. A ventricular septal defect is present and can be observed in A. A large, single trunk is connected to the right ventricle. C and D: orthogonal views for observing the great vessels. C: the proximal end of the great vessels. A common trunk is present. D: five great vessels branched from the common trunk. (P. 125)

**Fig. 5.5** CNCC-related great vessel defects. A-D: 3D OCT volume reconstructions and great vessel segmentation. Green: the aortic trunk vessels, purple: the pulmonary trunk vessels, cyan: branching errors. A: control embryonic heart. B: an example of PTA. The region with cyan color at the great vessels represents the common trunk. Arrow in B: ventricular septal defect. C: an example of incorrect branching. The aortic trunk branches into four vessels instead of three and the pulmonary trunk branches into one instead of two. D: absent great vessel. E: box plot of great vessel outer diameter measurements. The box represents 25% - 75% and the whiskers represent the range. AA and RBA in the CNCC-ablated group are significantly smaller than the control group. \*  $p < 0.05$  Green: the aortic trunk vessels, purple: the pulmonary trunk vessels, blue: branching errors; RBA: right brachiocephalic artery, LBA: left brachiocephalic artery, AA: aortic arch, RPA: right

pulmonary artery, LPA: left pulmonary artery. LV: left ventricle, RV: right ventricle. (P. 126)

**Fig 5.6** CNCC-ablated embryos exhibited left AV valve defects. Panels A-D are 2D OCT cross sections of four-chambered hearts from a sham control embryo (A) and three CNCC-ablated embryos (B-D). Their left AV valve leaflets are outlined by red (septal valve leaflets) and green (mural valve leaflets) dashed lines. A(s)-D(s) are side views of 3D reconstructions of the left AV valve leaflets that correspond to A-D and A(t)-D(t) are views of the atrial side. E shows results of volume measurements of left AV valve leaflets for 9 sham control embryos, 18 CNCC-ablated embryos that do not have PTA and 6 PTA hearts from the CNCC-ablated embryos. Error bar: standard error. \*  $p < 0.05$  LV: left ventricle. (P. 128)

**Fig 5.7** Microscopy images of embryo body flexures. A: control embryo. B and C: CNCC-ablated embryos with moderately twisted bodies. Their heart can be seen, although appears to be different than the controls possibly due to abnormally developed heart or a rotated angle. D and E: severely twisted CNCC-ablated embryos. Their hearts are not visible from the surface. (P. 130)

**Fig 5.8** Whole embryo images demonstrating body flexure (HH stage 19-20). A (a sham control embryo), B and C (two CNCC-ablated embryos) are projection images from 3D OCT volume rendering. A, B and C are the same embryos in Fig. 5.7 A, B and E respectively. Blue arrows point at the limb buds that were used for staging the embryos. Blue dashed-line circles: embryonic hearts (with artifacts due to the beating motion). Heart in C is not visible. The limb morphology indicates that all three embryos are between HH stages 19-20, closer to HH stage 20. (P. 130)

**Fig 5.9** CNCC-ablated embryos have abnormal flow profiles at HH stage 19-20. A-D are pulsed Doppler traces from a sham control embryo (A) and three CNCC-ablated embryos. The prominent shoulder phenotype is point out by arrows in A, B and C. The retrograde flow percentage (indicated in yellow arrows and number in A-C) is calculated as the ratio of negative peak area and the positive peak area. The retrograde flow percentages of the two examples are 10.7% and 20.4% for B and C respectively. D: A pulse Doppler trace from another experimental embryo that exhibited an arrhythmia. E: box plot of retrograde flow percentage for the control group and the experimental group. The box represents 25% - 75% and the whiskers represent the range. \*  $p < 0.05$ . (P. 131)

**Fig. 5.10** CNCC-ablated embryos have abnormal endocardial cushions at HH stage 19-20. Row 1 (A-D) are 2D OCT sections of HH stage 19-20 embryonic hearts. Row 2 (E-H) are 3D OCT volume rendering and cushion segmentations (green: inferior AV cushion, purple: fusion of superior AV cushion and outflow tract cushions). Row 3 (I-L) are the flow traces recorded *in vivo*. Panels in each column shows data from the same control or experimental embryo *in vivo* (pulse Doppler trace) and *ex vivo* (3D heart structural imaging). White arrows: the superior and inferior cushions. Blue arrows: large gaps between the superior and inferior AV cushions in the ablated embryos (B,C,F and G). yellow arrow: reduced cushion coverage in an ablated embryo. D: a CNCC ablated embryo that appeared to have

relatively normal cushions. A: atrium, AVJ: atrioventricular junction, V: ventricle, OFT: outflow tract. (P. 133)

**Fig. 5.11** OCT cross-sectional images of the AV cushions. A: a control embryonic heart. B and C: CNCC-ablated embryonic hearts. Arrow in A: the inferior and superior AV cushions contact each other and fill most of the lumen. Double head arrows: gaps between the inferior and superior AV cushions in ablated hearts. D: gap distance measurements. OFT: outflow tract. AVJ: atrioventricular junction. All three images share the same scale bar on the top left corner. (P. 134)

**Fig. 5.12** Proposed role of cardiac functions for CNCC-related CHDs. CNCC dysfunction causes abnormal early cardiac structures and functions, which compose a feedback loop (black dashed-line box) that may contribute significantly to late stage CHDs. Green solid arrows: previously established links with solid experimental supports. Green dashed arrow: previously suggested links with limited experimental supports. Red solid arrow: links established in this study. Red dashed arrows: suggested links in this study. (P. 142)

## **Acknowledgements**

Here approaching the finish line of this dissertation and my PhD career, I am extremely thankful for the research experience and life experience that I have had at Case. I have acquired knowledge, but more importantly, I developed the ability of solving problems and overcoming challenges. I believe that these will benefit me in the rest of life.

The work of this dissertation would not be possible without the support of many people. My deepest gratitude is to my adviser, Dr. Rollins, who has always trusted me to explore on my own, as well as provided guidance and suggestions whenever I needed. I am thankful to him for carefully editing the innumerable revisions of my scientific manuscripts and encouraging and supporting me to present at international conferences. He has set an example for a good researcher, a good adviser, and a good person.

I am grateful to have another four outstanding professors as my dissertation committee members. Dr. Watanabe, Dr. Jenkins, Dr. Yu and Dr. Singer have provided me with lots of constructive ideas, which have helped me move forward.

I am very fortunate to have a group of lab mates that are intelligent and friendly. I have benefited significantly from discussion with them and I have had countless fun experiences with them.

Most importantly, many thanks to my husband and my parents. They let me pursue my own path, yet never stopped supporting me, even from thousands of miles away. I would not have accomplished anything without them at my back.

## List of abbreviations

$\Delta F/F$	relative fluorescence response
1D	one dimensional
2D	two dimensional
3D	three dimensional
4D	four dimensional
AV	atrioventricular
AVJ	atrioventricular junction
CHD	congenital heart defect
CMOS	complementary metal-oxide semiconductor
CNCC	cardiac neural crest
CytoD	Cytochalasin D
DLSM	digital scanned light-sheet microscopy
DOF	depth of focus
DORV	double outlet right ventricle
EC	excitation contraction
EMCCD	Electron Multiplying Charge Coupled Device
ETL	electrically tunable lens
FAS	fetal alcohol syndrome
FASD	fetal alcohol spectrum disorder
FDOCT	Fourier domain optical coherence tomography
FOV	field of view
FRET	fluorescence resonance energy transfer
GEVI	genetically encoded voltage indicator
HH	Hamburger and Hamilton
LSCM	laser-scanning confocal microscopy
NA	numerical aperture
NCC	neural crest cell
OCT	optical coherence tomography
OM	optical mapping
PeT	photo-induced electron transfer
PTA	persistent truncus arteriosus
SDOCT	spectral domain optical coherence tomography
SHG	second harmonic generation
SNR	signal-to-noise ratio
SSOCT	swept source optical coherence tomography
TDOCT	time domain optical coherence tomography

# Optical Imaging of Embryonic Cardiac Conduction

Abstract

By

PEI MA

Coordinated cardiac conduction plays an important role in cardiogenesis, not only for initiating rhythmic contractions of cardiac myocytes for efficient blood pumping, but also for maintaining normal cardiac development. Optical mapping (OM), which uses fluorescent voltage-sensitive dyes to measure membrane potential is currently the most effective method for electrophysiology studies in early embryonic hearts due to its noninvasiveness and large field-of-view. OM has two major limitations: 1) it projects signals from part of a 3D sample to a 2D map therefore the electrophysiological information is incomplete, orientation-dependent and ignorant of 3D topology of the sample; 2) it requires excitation-contraction (EC) uncoupling drugs to stop the contraction of the heart, yet EC-uncouplers may affect calcium handling, ion channel kinetics and action potential characteristics. This dissertation focuses on overcoming the limitations of OM and improving cardiac conduction imaging in embryonic hearts. First, OM was integrated with optical coherence tomography (OCT), which is capable of capturing the 3D topology of the looped embryonic heart. A 3D conduction velocity correction algorithm was developed. This eliminated underestimation bias in 2D conduction velocity calculation and provided more accurate 3D corrected conduction velocity measurements. Second, 4D OM in the embryonic heart was achieved with light-sheet fluorescence microscopy. We built a fast light-sheet system that illuminated the sample with a sheet of light generated by a cylindrical lens and collected OM signals from an orthogonal direction. OM data from

multiple slices throughout the looping stage quail embryonic hearts were acquired. With this imaging system, complete, orientation independent, four-dimensional transmembrane potentials were demonstrated. Next, correction of motion artifacts in freely beating embryonic hearts was demonstrated using a B-spline nonrigid registration algorithm. Activation maps and conduction velocity measurements calculated from motion-corrected and the motion-free recordings are comparable. Finally, cardiac neural crest cells (CNCCs) were ablated in quail embryos as a congenital heart disease (CHD) model. Structural and functional defects at early and late stages were detected. This model will be applied in the investigation of how abnormalities in the conduction system arises. The imaging tools and CHD model developed here will significantly benefit the investigation of both normal and abnormal developmental cardiac electrophysiology.

## **Chapter 1. Background**

### **1.1 CHDs and embryonic cardiovascular research**

Congenital heart diseases/defects (CHDs) present a global health problem that accounts for about one third of all birth defects. The reported CHD prevalence is about 8.2/1,000 in the United States (US) and Europe, 9.3/1,000 in Asia and 1.9/1,000 in Africa [1, 2]. The low numbers in Africa is likely reflects the consequence of inaccessibility to medical screening and low ascertainment rather than reflecting an actual lower incidence of CHDs. In fact, even in more developed countries, this number of around 1% CHD prevalence only accounts for the easily observed, most common types of structural defects and is still a largely underestimated number. This number also does not include the severe CHDs that caused prenatal demise. Importantly, conduction system defects are not included in this number. Wolff-Parkinson-White syndrome itself accounts for up to 0.3% of the population [3]. Arrhythmias were reported to be the leading cause of morbidity and it has been shown that the incidence of arrhythmias increases as patients with CHD age [4]. The general thought that CHDs can be cured after surgical corrections in newborns is also not accurate. It was documented that over 50% of the total CHD population are adults [1]. Studies of the adult population indicate that CHDs significantly impact the quality of life for patients and their families, public health service utilization and cost [1]. Therefore, it is preferable to be able to prevent CHDs rather than try to correct it in a patient's lifespan.

Numerous developmental cardiovascular studies have been carried out in order to understand the etiology of CHDs. Significant progress has been made. For example, it was discovered that the neural crest derived cells are especially important for the outflow tract development and their dysfunction is likely responsible for many conotruncal heart defects

and valve defects [5, 6]. It has also been noted that CHDs can be induced at very early stages by environmental perturbations as well as genetic defects[7]. The resulting CHDs can start to have abnormal phenotypes as early as cardiac looping stages [8]. However, because of the complexity of heart morphogenesis as well as limited tools for imaging or assaying the developing heart, CHDs are still far away from being completely understood.

Among animal models developed for CHDs, the fetal alcohol syndrome model and the neural crest ablation model are particularly interesting to us because they model diseases of high prevalence in the human population and reflect the spectrum of CHDs frequently observed in in the human population.

#### *1.1.1 Fetal alcohol syndrome and the neural crest*

Prenatal alcohol exposure (PAE) can lead to fetal alcohol syndrome (FAS), which includes mental retardation and birth defects. Even a single dose of alcohol exposure can lead to FAS [9]. The reported FAS prevalence is 0.2-3 per 1000 children in the general U.S. population [10-14]. Fetal alcohol spectrum disorder (FASD), an umbrella term that covers the whole range of outcomes related to all levels of PAE, has the prevalence of 2% - 5% [15]. In addition to the most recognized craniofacial malformations and neurological behavior problems, 54% live-born children diagnosed for FAS also had congenital heart defects (CHDs) including septal defects, valve defects and conotruncal defects [7, 16]. Although it has been studied for many years, the mechanism of alcohol-induced CHDs remain largely unclear.

It was noticed a few decades ago that individuals with DiGeorge syndrome and FAS share common characteristics including abnormalities of the face, cardiovascular system, central nervous system, and immune system [17, 18]. DiGeorge syndrome has long been

recognized to be associated with disorders of the neural crest, which gives rise to a transient, multipotent, migratory cell population involved in the development of many organs and systems [19]. It has been shown that alcohol exposure influences the normal activity of neural crest cells (NCCs), either by increasing apoptosis or impeding NC migration signaling [20-25]. Both cranial and trunk NCCs are reduced, although non-uniformly.[20]. Cardiac neural crest cells (CNCCs), which are NCCs located at the mid-otic placode to somite 3, belong to the caudal most region of the cranial neural crest [26]. Most studies have focused on the craniofacial abnormalities with few investigating the heart defects [20]. The reduction of CNCCs due to alcohol exposure may at least be partially involved in the development of CHDs.

The study of CNCC-related CHDs were primarily performed using chicken CNCC-ablation models [5, 6]. CNCCs migrate out from the neural crest region, arrive at the pharyngeal arches, and a subset eventually enter the outflow tract of the heart. They contribute directly to the great vessel smooth muscle cells, the atrioventricular septum and the valves. They are also necessary for the great vessel remodeling. Lacking of CNCCs results in a spectrum of defects including persistent truncus arteriosus (PTA), double outlet right ventricle (DORV), ventricular septal defects and a variety of great vessel defects. The absence of CNCC also seem to influence many functional aspects. Reduction of contractility, blood pressure, stroke volume, ejection fraction and cardiac output at early developmental stages was related to CNCC-ablation/deletion in more than one animal models [27-29]. Function of calcium channels and excitation-contraction (EC) coupling was compromised at both early and late stages [30-33]. CNCCs were also reported to be involved in the maturation of the conduction system [34, 35]. CNCC-ablated hearts did not

transit into the mature apex-to-base conduction pattern at the expected stage [35]. Yet the understanding about the conduction system in the CNCC-ablation model, especially the early conduction system, is very limited. In addition, these pieces of information cannot be fully associated with each other. For example, the abnormal early functions (decreased contractility) were not directly associated to any specific developmental process, nor were they correlated with any specific late-stage defect type.

### *1.1.2 Cardiac conduction system*

One aspect that has not been extensively studied in the above FAS and DiGeorge Syndrome-like CHD models is the cardiac conduction system. Potentially this is because of the difficulty of setting up appropriate instrumentation, underdeveloped software and some current limitations of the imaging technology itself. These aspects will be discussed later in this chapter. This section will focus on the development of the cardiac conduction system.

Action potentials appear in cardiomyocytes of the heart tube before the heart starts to beat. The conduction pattern transitions through as the heart undergoes morphogenesis, and continues to function throughout life [36]. It is important that the heart maintains a coordinated heart beat as it develops from a tube into the four-chambered form. During development the conduction of the heart is realized through an electrically coupled myocardium while the mature conduction system includes the sinoatrial node, atrioventricular (AV) node and the His–Purkinje fibers [36].

As the heart starts to form, three critical transitions in the impulse propagation pattern happen in sequence, as shown in Fig. 1.1: 1) the development of the AV-delay pattern, which involves a slow conducting AV junction and outflow tract region and an atrial and

ventricular region with significantly increased speed; 2) the dissociation of conduction at the interventricular septum region; 3) the transition of base-to-apex to apex-to-base conduction pattern as the formation of four chambers is completed [36]. The fast and slow conduction in different regions of the hearts is coordinated in part through the distribution of the fast and slow gap junctions [36].

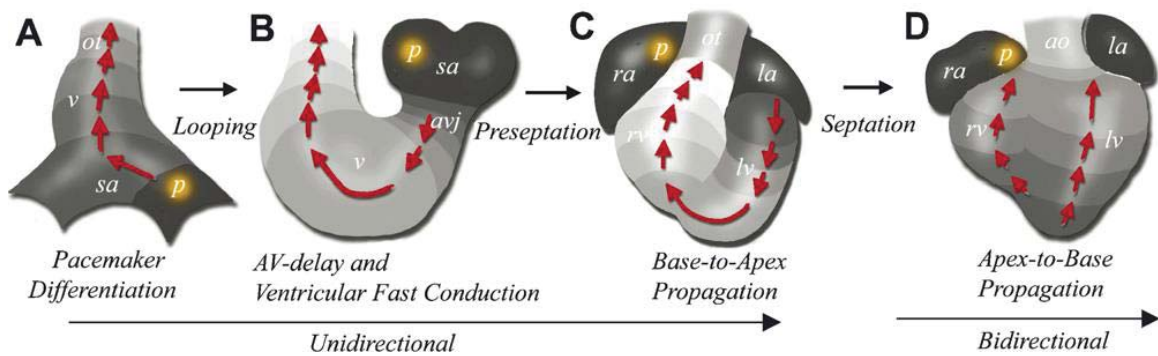


**Fig. 1.1** Transitions of conduction pattern during cardiac development. A: uniform conduction at straight heart tube stage. B: the development of AV-delay and the slow-fast-slow conduction pattern at cardiac looping stage. C: base-to-apex conduction pattern during interventricular septation. D: apex-to-base conduction pattern due to the maturation of the His–Purkinje fibers and the atrioventricular fibrous ring that separates the atrial from ventricular tissues. Figure adapted from Mikawa and Hurtado, 2007 [36].

Abnormal conduction during development lead to CHDs. Chi et al. reported a zebrafish cardiac mutant (*dco<sup>s226</sup>*) study with the finding that abnormal conduction caused heart failure and interrupted cardiac morphogenesis, independent of hemodynamic function or cardiac contraction [37]. Other modification of various types of connexins resulted in arrhythmias as well as structural defects [38-41]. Specifically Cx43 seems to be responsible for the outflow tract defects and neural tube defects [38, 39]. In addition to its independent influences on cardiogenesis, abnormal conduction causes altered hemodynamics and biomechanics, which are also critical factors in the etiology of CHDs [42-44].

One area that does not have abundant information is the interplay between the early conduction system and other cardiogenesis aspects, and how do they eventually cause CHDs. This is partially due to the challenging task of imaging the early conduction system. Improved imaging tools and computational methods are in significant demand and will provide important insights in filling the gaps of the current understanding.

### *1.1.3 The avian model*

The avian model is the earliest and one of the most commonly used models in developmental cardiovascular research [45]. Avian species develop four-chambered hearts, which morphologically and functionally resemble human hearts. The cardiac development of avian embryos is also very similar to that of human [45]. The gestation period of chicken or quail ranges from 19 to 21 days, which is much shorter than human or other animal models. Large quantities of fertilized eggs can be easily and economically acquired and incubated without the need for caring or sacrificing the mother animals in the laboratory setting. The environmental control for growing the eggs is simple – no more than a relatively inexpensive incubator. Chicken/quail embryos are highly accessible. The embryos in the egg, can be observed or manipulated through a hole or window in the eggshell [46]. The embryo is able to grow to hatching by this method. Alternatively, the embryos can be cultured shell-less in Petri dishes, in which they can grow to the last a few days before hatching. The fact that the embryos are on top of the yolk made observation and manipulation straight forward in both culturing methods. For these reasons, the quail embryo will be the targeted animal model in this dissertation. Staging of the embryos are based on the Hamburger and Hamilton (HH) stages [47].

## **1.2 Optical mapping**

Understanding of cardiac electrical activity would not have been possible without the development of technologies including electrodes and optical imaging methods. Optical mapping (OM) is a general term for imaging membrane potentials with optical methods. OM is appealing to cardiac electrophysiologists because it has several advantages over traditional electrode recording [48, 49]. First, OM is capable of acquiring signals from thousands of sites in one imaging session. Because conduction of the heart happens quickly and the whole heart is active, it is obviously beneficial to collect signals from the entire field of view simultaneously. Second, optical recording can achieve high spatial and temporal resolution. Recordings can be made from targets that may be too small for electrodes. Third, OM does not need contact with tissue, therefore ensures the integrity of the sample. It is yet not “non-invasive”. Although it does not cause damage of the tissue through contact, it can affect the sample pharmacologically because the dye used is toxic [50-52].

OM has made enormous contributions in the investigation of cardiac electrophysiology in the past several decades. This section includes an overview of voltage-sensitive dyes, critical components of an OM system, major applications of OM in cardiac electrophysiology and current limitations of OM in embryonic cardiac imaging.

### *1.2.1 Voltage-sensitive fluorescence dye*

The discovery and development of organic voltage-sensitive dyes are the foundation of OM. In the mid-1970s, Cohen et al., screened hundreds of commercial dyes and discovered many of them with voltage-indicating properties [53]. Loew’s lab later developed potentiometric dyes, in which some of them are still extensively used nowadays, such as di-4-ANEPPS [54]. After that, multiple groups have developed many dyes that are based

on different voltage-sensing mechanisms and/or have different properties [55-59]. Overall, the fast and linear responses of the dyes in response to the changes in potentials enabled them to provide a direct measure of electrical activities in excitable tissues. An alternative to these organic voltage-sensitive dyes is genetically encoded voltage indicators (GEVIs) [60, 61]. They will also be briefly discussed in this section.

The chromophore, which interacts with light, is the important portion of any dye. When absorbing a photon within its spectrum the chromophore can be excited from its ground state to the excited state. Then the molecule undergoes a vibrational relaxation process to return to the lowest energy states through emitting a photon or heat releases. Between these two processes there may exist a short, a few nanosecond time period that the molecule stays at the excited state while rearranging its electrons to a more stable configuration. This causes the emitted light to be a longer wavelength than the excitation light, hence introducing fluorescence. Changes in membrane potentials cause the environment of the molecule to alter, therefore resulting in either a direct fluorescence change, or the absorption and emission spectrum of the chromophore to shift. By imaging a proper portion of the spectrum, the shift of the spectrum is also reflected as an intensity change.

Established voltage-sensitive dyes respond to action potentials through several different mechanisms [52, 57]. In the use of voltage-sensitive dyes, some important factors need to be considered: response speed, efficiency of fluorescence, sensitivity to the environment, photostability and phototoxicity. Some of these factors are closely related to the mechanism of dye function.

Three major mechanisms will be described here (illustrated in Fig. 1.2): electrochromic, fluorescence resonance energy transfer (FRET) and photo-induced

electron transfer (PeT). In electrochromic mechanism, electrochromic dyes directly interact with the electric field. Through the Stark effect, the spectra of the chromophore shifts by a small amount when the membrane depolarizes. This process happens very fast, on the femtosecond to picosecond timescale. In this mechanism, the best signal can be acquired at the steepest slope on the spectrum. However, the signal-to-noise ratio (SNR) is usually low due to the small relative response ( $\Delta F/F$ ). Common dyes in this category are di-4-ANEPPS, di-8-ANEPPS and di-4-ANEPPDHQ. In the FRET mechanism, there is a donor fluorophore and an acceptor fluorophore anchored to the cell membrane. When excited, the donor fluorophore transfers its energy to the acceptor fluorophore and longer wavelength light is emitted by the acceptor fluorophore. FRET is a distance related process. Depolarization of the membrane increases the separation between the donor fluorophore and the acceptor fluorophore therefore quenches the fluorescence signal. Dyes of the DiSBAC<sub>x</sub> family and the CC<sub>x</sub> family are examples in this category [62]. The PeT mechanism is relatively new compared to the invention of other two groups, but it has shown promise due to its ability to produce large responses. In the PeT mechanism, a fluorescent reporter is connected to an electron-rich donor through a molecular wire. At the resting potential, electrons are transferred from the donor to the fluorophore through the molecular wire, quenching fluorescence. Depolarization of the membrane hinders this electron transfer therefore brightens the fluorescence. In the PeT mechanism, the response time is on the picosecond to nanosecond timescale, which is magnitudes lower than the electrochromic mechanism. However, the most significant advantage of this mechanism is the large  $\Delta F/F$ , easily over 20%. Also, due to the low background, the SNR is also much higher than many other dyes. VF2.4.Cl is an example in this category [57].

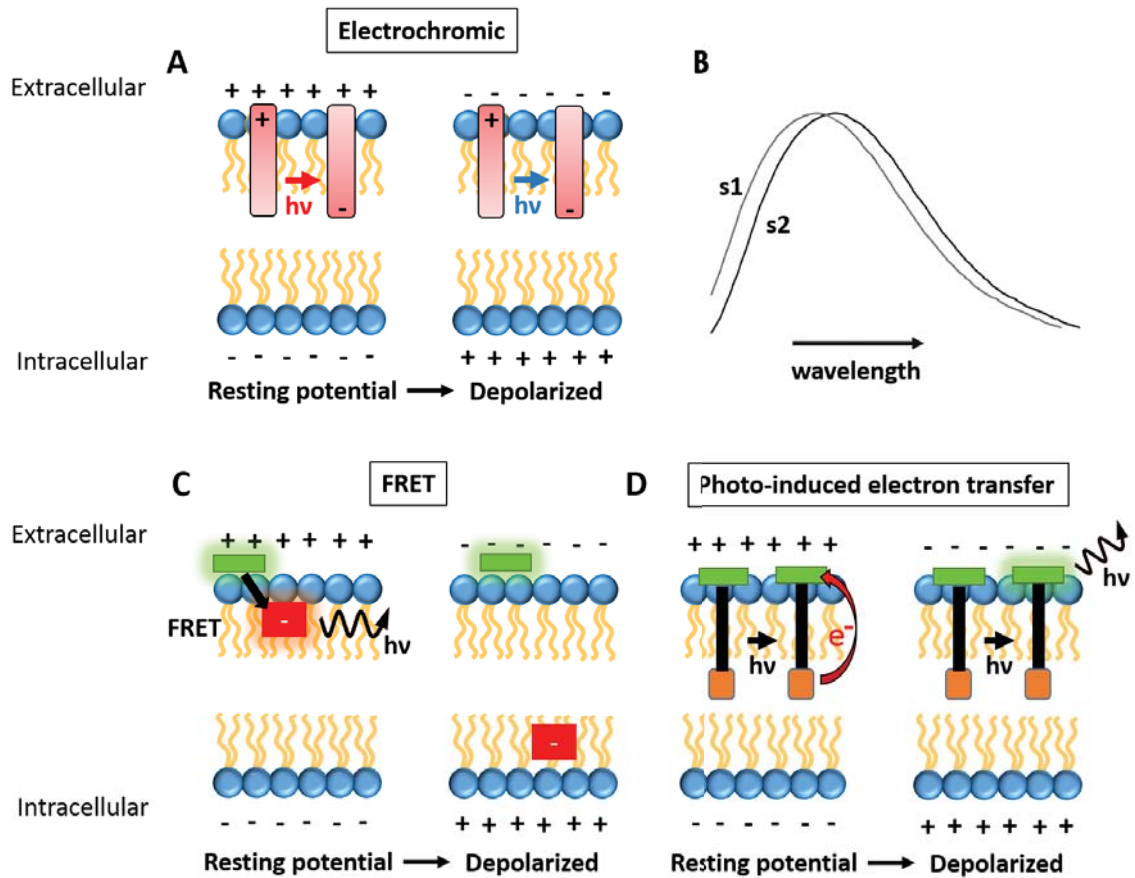


**Fig.1.2** Voltage-sensitive dye mechanism. A: electrochromic mechanism is based on the Stark effect. The dye spectra shifts by a small amount when the membrane depolarizes. B: an example of spectra shift of electrochromic dyes. The spectra can represent excitation or emission spectra. Either one may represent before and after voltage changes. s1: spectrum 1, s2: spectrum 2. C: voltage-sensitive dye based on FRET mechanism. Distance between the two fluorophore changes as the membrane depolarizes therefore the intensity of collected signal is altered. D: PeT voltage-sensitive dyes have electron wires to transfer electron and quenches fluorescence. Depolarization decreases electron transfer rate therefore increases fluorescence. Redrawn and modified from Miller et al. 2007 [52].

The limitations of voltage-sensitive dyes involve photobleaching and phototoxicity. Photobleaching refers to the photo-induced chemical effect on the fluorophore molecule that makes it unable to fluoresce after a limited time of photoactivation [63]. This can diminish SNR greatly and result in unanalyzable data. Voltage-sensitive dyes exposed to light can also introduce free radical products that cause damage or death to the cells [64].

Most voltage-sensitive dyes have phototoxicity to some extent, but some are less toxic than others [64]. The duration of an OM experiment is usually limited by one of these two concerns. Therefore, depending on the tissue type and the environmental condition, the selection of an appropriate voltage-sensitive dye is important and the type of dye selected can significantly vary. The light exposure level of each experiment also needs to be optimized, *i.e.* maximized for the SNR and minimized to avoid the dye being bleached too quickly and lower the phototoxicity for keeping the sample as healthy as possible for as long as possible.

Dyes and mechanisms described above are all based on what is conventionally called one-photon event (excitation, absorption and fluorescence). Because non-linear microscopy (two/multi-photon microscopy, second harmonic generation microscopy) have certain advantages over one-photon processes, researcher started to engineer voltage-sensitive dyes that have such characteristics [52, 65-69]. One thought is that one-photon imaging does not reject out of focus light therefore causes blurring in some regions of the image and optical sectioning ability of non-linear microscopy overcomes this issue. Another reason to consider second harmonic generation (SHG) is that because SHG does not involve an excitation state, it potentially eliminates photobleaching and phototoxicity as in the one-photon processes. Furthermore, two-photon or SHG OM are more suitable for thicker tissue imaging because excitation using infrared wavelengths allow deeper penetration into tissues. In the two-photon process, two photons of approximately twice the wavelength (hence half energy) than the one-photon process need to be absorbed at the same time in order to reach the excited state. The molecule at the excited state then fluorescence the same way as the one-photon process. There is essentially no difference in

the mechanism of voltage sensing and the general setup between two-photon OM and the conventional one-photon OM, except for using a femtosecond laser at about double the desired excitation wavelength and using scanning to acquire the entire field of view. Although two-photon OM provides sectioning ability and deeper penetration, it slows down the imaging significantly due to collecting signals from one site at a time unless a complicated fast two-photon system is developed. SHG is also a non-linear event, but it has fundamental differences compared to the two-photon process. Two photons of the same energy instantaneously transform into a single photon that has exactly twice the energy of the initial photons and no excitation state is involved in this process. SHG OM relies on finding a dye that has good SHG responses. Although such dyes were discovered or developed (di-4-ANEPPS, PY-x probe family, AR-x family and FM-4-64 etc.), the response time (usually slower than a millisecond), sensitivity, or SNR is still not ideal for SHG OM imaging [68, 69].

Because organic voltage-sensitive dyes are non-specific to cell types, genetically encoded voltage indicators (GEVIs) were developed by some groups to overcome this issue. Although GEVIs do not have photo-induced toxicity, they may have other less detrimental pharmacological effects [52]. They were successfully demonstrated in neural and cardiac experiments [61, 70, 71], yet the access is still largely limited and the sensitivity and speed of GEVIs still need to be improved.

### *1.2.2 OM system*

An OM system generally includes a stable light source, appropriate filter sets, basic optics and a fast camera, as shown in Fig. 1.3. The image quality and SNR of the signals are closely related to these components, despite the determining role of the response size of

the dye. As the illumination light intensity is increased from zero, dominant noises of the final result should be shifting from camera read noise to shot noise and eventually to light source excessive intensity noise, but the last state does not often happen in OM because light intensity rarely reaches that level. A good system should be shot noise limited, in which the SNR is proportional to the square root of the number of photons incident on the detector. In this range, the higher the illumination is, the better the SNR will be. Earlier OM experiments used tungsten halogen lamps or arc lamps as the illumination source while recently light-emitting diodes clearly showed advantages in producing clean, stable and bright light. Lasers offer even higher intensities, yet it requires a modified optical setup to generate uniform illumination. Otherwise it only illuminates a point at a time. Also some dyes may produce better signals with broadband illumination. The usage of lasers in OM is mostly in two-photon or second harmonic generation microscopy.

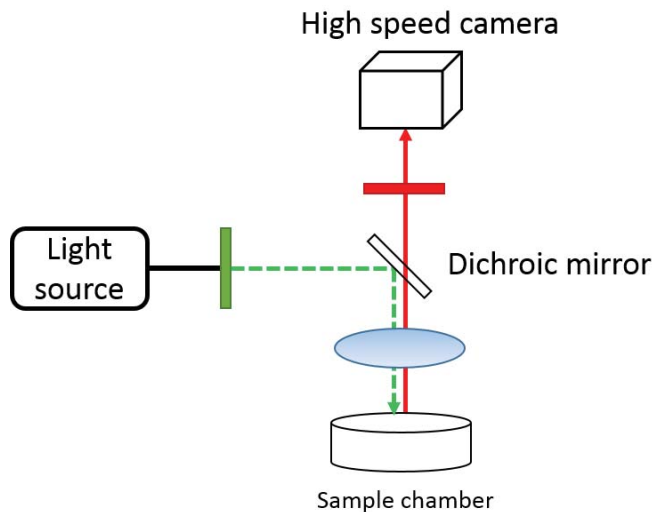


**Fig. 1.3** Schematic diagram of an OM system.

The selection of filters is especially important for imaging with the spectra shift dyes or the usage of SHG responses of dyes. At the peak of excitation/emission spectrum, the

fluorescence signal is the strongest, however, because the useful signal is the fluorescence change due to the spectrum shift, the peak of the spectrum usually gives a small change. In contrast, the largest change is at the inflection point of the spectrum, which does not have the strongest response and may potentially result in a lower SNR. The tradeoff between the size of the fluorescence signal and the size of the response needs to be taken into consideration.

Another way of maximizing the number of photons is choosing objective lenses with high numerical aperture (NA), especially under the situation that the light source has limited power. In conventional OM systems, the excitation and emission light travels through the same objective, therefore the photons reaching the detector is proportional to the 4<sup>th</sup> power of the objective NA [72].

Parameters that need to be considered in selecting a camera are well depth, read noise, quantum efficiency, pixel numbers and speed. Electron Multiplying Charge Coupled Device (EMCCD) has been a popular selection due to its high quantum efficiency, large well depth (this is especially important for high background but low signal situation), very low read noise (this would benefit low light situation) and acceptable speed. Under less demanding situations, complementary metal-oxide semiconductor (CMOS) cameras may be a better choice because they are cheaper, faster than EMCCDs in bigger field of views. Recently scientific CMOS cameras became available on the market and they have much improved performances.

Although more light means higher SNR, there is always the tradeoff between the SNR and the resulting phototoxicity on the sample.

### *1.2.3 OM applications in the heart*

OM has been widely used to study neural and cardiac cell and tissue electrical activity. This section will focus on OM application in the heart, especially embryonic heart.

#### *1.2.3.1 OM of the adult heart*

In the heart, it is especially important to image the entire field of view for the observation of conduction patterns. The most valuable application of OM in adult heart is the characterization of regular and irregular conduction, including arrhythmias and fibrillation. Using OM, Davidenko et al. reported the first demonstrations of the spiral waves in the heart and their role in arrhythmias [73, 74]. Gray et al. developed novel algorithms towards describing the complex patterns of fibrillation and this greatly reduced the amount of data needed [75]. Since then this measurement of phase singularity has been used extensively in both basic and clinical investigations of the mechanisms responsible for atrial and ventricular fibrillation.

#### *1.2.3.2 OM of the developing heart*

Kamino's group started the pioneering work of using OM to characterize the early embryonic cardiac conduction system. They used a tungsten-halogen lamp, merocyanine-rhodanine dyes and a photodiode to probe 7-9 somite stage chick embryonic hearts and measured spontaneous and coordinated transmembrane potentials. At these stages, the chick hearts begins to beat [76-80]. They found that before the heart begins to contract, electrical activities exist. These reports provided the initial understanding of early cardiac electrophysiology as well as deploying OM as a tool for investigating embryonic cardiac electrical activities.

The origin of pacemaking cells has been of interest for decades. OM together with lineage studies in chick embryonic hearts recently supported a hypothesis that mature

pacemaking cells arise from a tertiary heart field [81]. The recruitment of mesodermal cells within this tertiary heart field into the pacemaker lineage involves canonical Wnt signaling.

OM has made significant contributions in identifying when and how the developing heart transit from one conduction pattern to another. In early development the heart does not have a fully specialized conduction system, instead, the conduction is uniformly slow and homogeneous through adjacent myocytes. With the maturation of the heart, the conduction pattern transitions from uniformly conducting, to alternating regions of slow and fast conduction and eventually to the bidirectional apex-to-base propagating manner. Chuck et al. and Sedmera et al. experimentally demonstrated and determined the timing for the latter transitions in embryonic chick hearts [82, 83]. Further characterization of conduction transitions was reported by Gurjarpadhye et al., who developed a quantitative measurement of a “breakthrough angle” in the transition from base-to-apex to apex-to-base sequence. The breakthrough angle at immature base-to-apex stages is at -30 degrees, which is at the left side of the base, while in the mature apex-to-base situation the breakthrough is at the apex (180 degrees). They have also observed that the progression of the breakthrough angle in defected embryos was altered indicating a failure of maturation in the cardiac conduction system [35].

Conduction transitions of the heart are coordinated with structural development [84]. Besides the role of signaling, cardiac structures themselves may have a direct influence in modifying electrical properties of myocytes. In looping stage chick hearts, the development of AV delay and cardiac cushions in conjunction effectively prevent retrograde flow. Recent studies with OM showed that endothelin 1 (Et1) signaling can directly influence the expression of gap junction Cx40, which is the fast conducting gap junction. At the AVJ,

increased physical separation between the endocardium and myocardium by the expansion of the intervening endocardial cushion results in reduced Et1 signaling from the endocardial cells reaching the myocardium therefore the normal growth of the cushions prevents the AVJ myocardium from becoming a fast conducting myocardium [85]. Other regions such as the atria and the ventricle have much thinner cushions. Thus the myocardium in those regions are exposed to more Et1 signaling and become fast conducting. OM provided conduction pattern and conduction velocity measurements, which were critical in supporting the hypothesis.

Chick hearts are one of the most studied models for developmental electrophysiology because of their similarities to human hearts and the convenience of their use. Yet it is limited in that gene manipulation is not readily available. Zebrafish, in contrast, have an extensively sequenced genome and many mutant lines are readily available providing a comprehensive genetic resource. Because of the transparency of the zebrafish embryo, *in vivo* OM experiments can be carried out. This has provided fruitful discoveries in signaling pathways, mechano-electrical feedback of the heart and the identification of electrophysiological contributions from the first/secondary heart fields [86-88].

#### *1.2.3.3 OM signal and image processing in cardiac applications*

It has been a few decades since the use of OM in cardiac electrophysiology. There are some generally accepted image processing and presenting conventions, originally developed in OM studies of the adult heart and then gradually adapted to OM of the embryonic heart. A region of interest is selected first, then signals from each pixel go through processing steps such as normalization, drift (photo bleach) correction and filtering for SNR improvement [89]. Then each action potential trace is used to identify its activation point and

repolarization point for acquiring parameters such as activation time, action potential duration (APD) and conduction velocity. Taking derivative of the action potential is a common way of acquiring these two time points [49, 89]. Our group published a method using two cumulative fitting algorithms to find the activation time [90]. This method is demonstrated to be more robust under low SNR situations. An activation time map is usually created by assigning each pixel its activation time. It is presented in colors representing activation sequence and/or isochrones lines indicating a user-defined time interval. APD is usually presented in color maps. It is important to point out the definition of APD in presenting the data. For example, APD<sub>80</sub> is defined as the duration between the activation time and the time of 80% repolarization. Conduction velocity can be calculated by acquiring the gradient vector of each pixel with its neighboring pixels [91]. This method can suffer when there is a high level of noise under low SNR conditions. As developed by other groups in the application of adult hearts and recently by our group in the application of embryonic hearts, an alternative method for conduction velocity calculation is to use a polynomial surface to fit an activation time kernel around each pixel [90, 92]. The conduction velocity vector is calculated from the gradient of the fitted surface. The display of conduction velocity is often colormaps or quiver maps.

#### *1.2.4 Current limitations of OM*

##### *1.2.4.1 Motion artifacts*

The motion of the contracting heart can obscure OM signals and lead to unanalyzable results, therefore motion correction is required. The most popular method for avoiding motion in OM is to use an excitation-contraction (EC) uncoupler, which eliminates heart motion without stopping activation/conduction. Cytochalasin D (CytoD), blebbistatin and

BDM are the most popular EC-uncouplers [93, 94]. The mechanism of EC-uncoupling of CytoD is that it inhibits the G-actin–cofilin interaction by binding to G-actin and it decreases the rate of actin polymerization [95]. Although using EC-uncouplers has been a standard procedure in OM, they may affect ion channel kinetics, calcium handling, and action potential morphology [96, 97].

Other methods were attempted in suppressing or correcting for cardiac motion without using EC-uncouplers. One method is to immobilize the surface of the heart against a glass plate to reduce the beating motion [98]. Another method is to correct motion artifacts in post processing using image registration [99, 100]. A ratiometric approach was also developed by adding another non-voltage sensitive imaging channel [101]. Theoretically the non-voltage sensitive channel reflects signal changes solely due to the motion of the heart therefore it can be used to subtract the effect of motion in the voltage sensitive channel and bring back clean action potentials. However, each of these methods has their problems and the situations in which they could work are very limited.

#### *1.2.4.2 Depth-resolved OM*

OM has replaced electrodes for electrophysiology studies for many years. This is because investigation of cardiac conduction often requires imaging thousands of sites from a field of view at once. However, this transition from using electrodes to OM caused the loss of an important feature, depth-resolving ability. Because most of the dyes use excitation light in the visible range, the majority of the signal comes from surface cells, with some contributions from sub-layer cells depending on the absorption and scattering properties of the tissue. Events such as arrhythmias can be complicated in 3D. Information from the surface of the tissue may not be able to fully represent the events. Another issue related to

this topic is that OM collects signals from the surface of a 3D object and projects the signals to a 2D plane. This projection can cause biases in interpreting the results.

For the analysis of adult hearts, several approaches were proposed to resolve information from different depths. For example, optrode arrays were developed and used to acquire intramural cardiac transmembrane potentials [102, 103]. This method shares disadvantages that are similar to those of electrode arrays. A non-destructive method uses dual wavelength imaging (di-4-ANEPPS and an near infrared dye di-4-ANBDQBS) to detect transmural heterogeneity in intact rat hearts [104]. Khait et al. proposed a theoretical method of resolving signals from different depths by acquiring and analyzing both the reflection and transmission light based on the diffusion theory [105]. This method requires cutting the sample into slices. It was experimentally demonstrated by Mitrea et al. [106].

To acquire complete surface information, panoramic imaging of adult hearts was developed and applied [107-109]. Two to three cameras were placed around the heart to capture OM signals from different regions. A geometry camera, which was mounted on a rotational motor centered at the heart, rotates 360 degrees to capture surface information of the heart. Images were combined later to form an accurate geometric model of the heart. OM data was then mapped to the heart model and used to create panoramic OM. In some studies, mirrors were used to reflect some views to reduce the number of cameras needed to capture data from more of the surface of the heart [35, 108]. Panoramic OM not only provided complete electrophysiology information, it also offers the topology of the heart for correct conduction velocity calculation, which is highly dependent on accurate distance measurements.

Embryonic hearts have much fewer cell layers than adult hearts, therefore other options can be considered or may be preferred to acquire depth-resolved electrophysiological data. Recently, Hou et al. used 3D spinning disk confocal microscopy to image zebrafish heart with genetically encoded dual-function calcium and voltage reporter CaViar [110]. Both voltage and calcium data were collected in 3D. This was achieved due to the transparency of zebrafish embryos and the small size of zebrafish hearts.

#### *1.2.5 Reliable pacing scheme*

Cardiac electrophysiology parameters, such as action potential duration and conduction velocity are heart rate dependent [111, 112]. It is beneficial to know the exact timing at each site in the field of view compared to an activation initiation spot. Consistent heart rate is especially important for making direct comparisons between different samples. OM in adult hearts often uses electrodes as a point stimulation source [113]. Point stimulation provides conduction signals initiating from a small region, which is similar to the function of the SA node in the heart. Furthermore, point stimulation can be extremely helpful in studying arrhythmia because the pacing spot can be moved to various specific locations [114, 115].

In embryonic hearts it is not feasible to stimulate using electrodes. Embryonic hearts are small and fragile. Using electrodes for stimulation requires contact, therefore likely damages the embryonic heart and alters its function. The artifacts caused by electrode stimulation are also significant and possibly make electrode stimulation a field stimulation method rather than point stimulation. Field stimulation is also not ideal because it may cause initiation over the entire sample. It has been long known that light exposure can change the excitability of tissues[116, 117]. Noninvasive, optical pacing the hearts was

developed as a reliable stimulation method and it was demonstrated with OM, as shown in Fig. 1.4 [118-120].

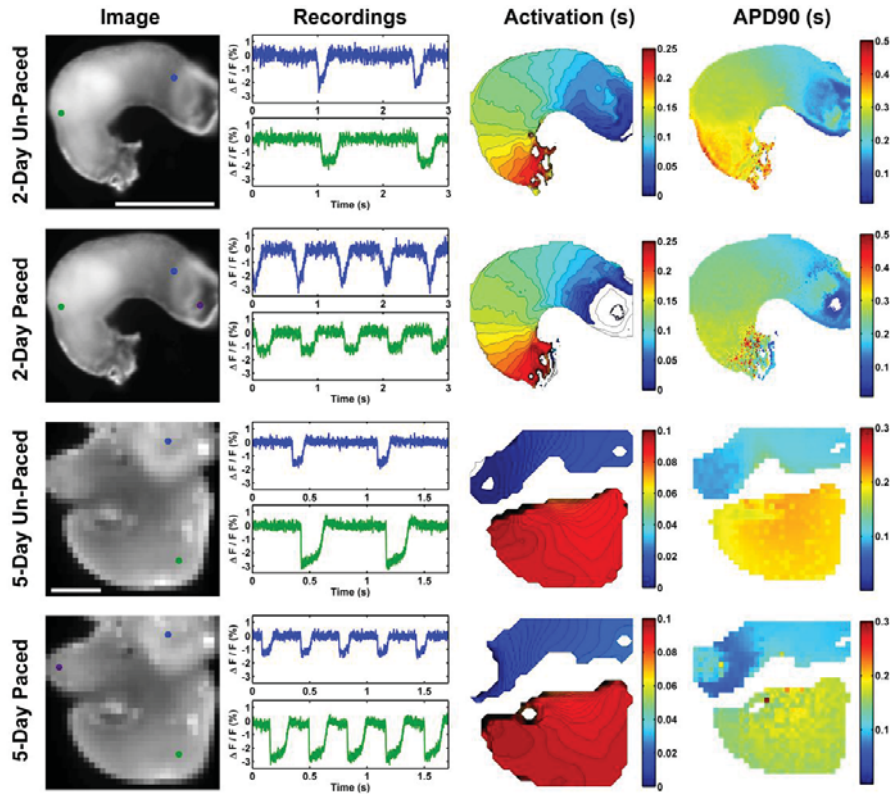


**Fig. 1.4** Integrated OM and OP. Fluorescence images, action potential recordings, activation maps and action potential duration maps are shown for examples of unpaced and paced 2-day and 5-day embryonic hearts. Adapted from Wang et al., 2014 [119].

### 1.3 Optical coherence tomography

Optical coherence tomography (OCT) is an optical imaging modality that has been widely used in biomedical applications since its emergence in 1991 [121]. OCT is analogous to ultrasound except that it delivers light into the tissue instead of sound. OCT performs fast, high-resolution, 3D imaging of *in vivo* biological samples noninvasively. The resolution and field of view of OCT imaging are 1-30  $\mu\text{m}$  and a few millimeters, respectively. Due to this feature, OCT fills the gap between cellular level imaging modalities (high resolution with small penetration depth and field of view, *e.g.* microscopy) and organ/body level

imaging modalities (low resolution with large penetration depth and field of view (FOV), *e.g.* ultrasound, MRI, etc.). The leading clinical application of OCT is in ophthalmology, followed by areas such as cardiology, gastroenterology and dermatology [122-126]. In basic science research, OCT has been extensively used and significantly broadened our understanding in developmental biology due to its 3D, high-speed, high-resolution, large FOV, noninvasive and functional imaging features. This section includes the description and discussion of the basic principles of OCT, three OCT implementations and its applications to the study of developmental biology.

### *1.3.1 Michelson interferometer and time domain OCT*

Time domain OCT (TDOCT) in theory is a low-coherence version of Michelson interferometer (Fig. 1.5). Traditional Michelson interferometer sends monochromatic light to two light paths through a beam splitter. Each path has a mirror to reflect the light, which is then recombined at the beam splitter and directed to a detector. When moving the mirror from one path (reference arm), ongoing fringes can be observed at the detector. This phenomenon is based on the interference property of coherent light.

When using a low-coherence light source in the same setup, because light of each wavelength generates fringes with different spacing, the summation of these fringes forms a much narrower fringe pattern centered at the location where the path lengths from the two arms matches perfectly. The slope of the fringe pattern is called the point spread function (PSF) and the value at the full width of half maximum (FWHM) is the coherence length of the broadband, low-coherence light source, which is also the axial resolution of this low-coherence interferometer. The coherence length ( $l_c$ ) can be theoretically calculated using this equation:  $l_c = \frac{2\ln(2)}{\pi n} \frac{\lambda_0}{\Delta\lambda}$ .

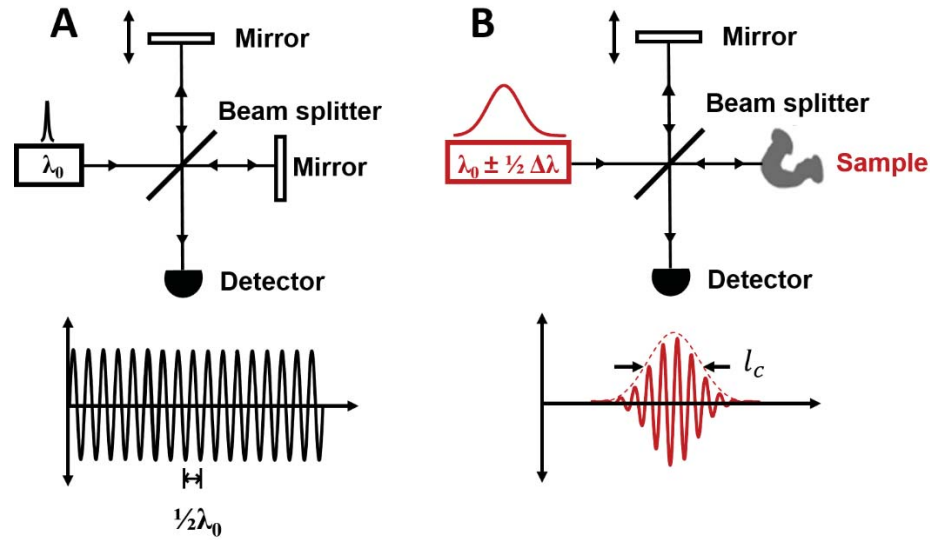


**Fig. 1.5** Michelson interferometer and TDOCT.

TDOCT is based on this scanning, low-coherence interferometer. With one scan trip of the reference mirror, a line in the depth dimension of the sample can be acquired. This line is called an A-scan. Scanning the beam and collecting many A-scans forms an image, which is called a B-scan. This is usually achieved through a galvanometer mirror (galvo) in the sample arm. Acquiring multiple A-scans without scanning the beam is called an M-scan. This can be useful for capturing dynamic events. Further adding another galvo will produce multiple B-scans and achieve volumetric imaging, as shown in Fig. 1.6.

Assuming the beam profile is Gaussian, the lateral resolution is defined as the FWHM of the lateral PSF, which is determined by the optical components in the system:  $Resolution_{lateral} = \left(\frac{4\lambda_0 f}{\pi D}\right)$ , where  $f$  is the focal length of the focusing lens and  $D$  is the collimated beam diameter. Depth of focus (DOF) is what we consider the range of high quality imaging without much resolution degradation. If we define the DOF as the range

where the beam is  $\sqrt{2}$  times larger than the beam waist, the DOF can be calculated as  $DOF = \left(\frac{8\lambda_0}{\pi}\right) \left(\frac{f}{D}\right)^2$ . Here we can see that large DOF comes with low lateral resolution while achieving high lateral resolution means sacrificing DOF. This rule is valid when the beam profile created is Gaussian. Sample arms that use Bessel beam design can extend the narrow focus in the expenses of losing some light intensity. Assuming the galvo is at the focal plane of the focusing lens, the field of view is therefore given by  $FOV_{lateral} = 2f \tan \theta_{max}$ , where  $\theta_{max}$  is the largest scanning angle on one side. These rules regarding lateral resolution, DOF and FOV are also valid for the Fourier domain OCT systems, which will be discussed in the following section.

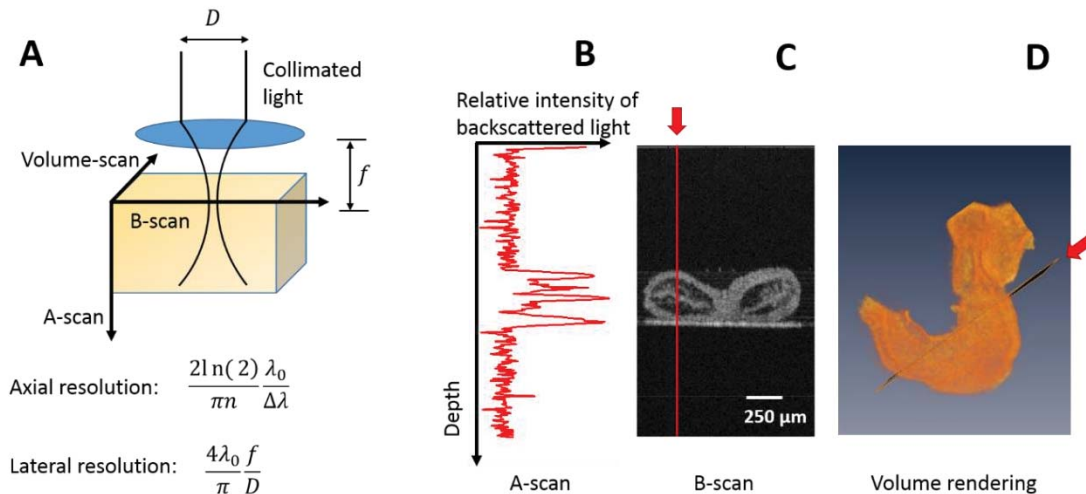


**Fig. 1.6** Beam scanning in OCT. A: collimated light is focused on the sample through an objective lens. The 3D relationship of A-scan, B-scan and volume-scan. B: An A-scan from the indicated location in a B-scan (red arrow in C). C: a B-scan of a dissected embryonic heart. The B-scan is from a slice in a volume scan of the heart at the indicated location in D. D: volume rendering of the embryonic heart.

### 1.3.2 Fourier domain OCT

A major drawback of TDOCT system is the speed due to acquisition of a single point at a time and scanning of the reference mirror for a complete A-scan. Later, almost the entire field switched from TDOCT to Fourier domain OCT (FDOCT), of which there are two

forms: spectral domain OCT (SDOCT) and swept source OCT (SSOCT). A comprehensive review of Fourier domain OCT can be found in a recent book chapter [127]. This section will briefly review the theory of Fourier domain OCT.

In FDOCT, no scanning is need for the reference mirror. Instead of collecting light of all wavelength at the same time and physically change the path length to acquire fringes, FDOCT analyzes the spectral fringes, which is one component in a Fourier pair. The other component is the spatial location of the scatters in the interested sample. The path length mismatch between the reference arm and a scatter from the sample arm causes a spectral modulation. The frequency modulation caused by scatters from multiple layers is integrated and detected. By Fourier transform this signal, the location of scatters can be acquired. Therefore in both methods, the entire A-scan can be acquired simultaneously, therefore significantly increases the speed of data acquisition. Fig. 1.7 shows simplified system diagrams and the mechanism of FDOCT.

In SDOCT, the special part of the system is the way it detects signals. Instead of using a photo detector, the output beam is directed to a spectrometer and then received by a line-scan camera. Each pixel detects a small portion of the spectrum and the spectral resolution  $\delta\lambda$  determines the depth range  $= \lambda_0^2/4n\delta\lambda$ . Although decreasing  $\delta\lambda$  can increase the depth range, we also need to acknowledge that  $\delta\lambda$  is finite, as well as the pixel size. Convolution of the signal with these finite-size components results in sensitivity reduction, also called falloff.

Several aspects are important in SDOCT in producing high quality images. First, the distance of scatters in the sample is the Fourier transform of spatial frequency,  $k = \frac{2\pi}{\lambda}$ , not wavelength. Therefore, a correction from linear-in-wavelength to linear-in-k needs to be

performed. It can be achieved through modifying the spectrometer [128], or an interpolation in software after acquiring all the signals. Second, because SDOCT cannot have heterodyne detection, the DC components needs to be subtracted either by acquiring and subtracting an image with sample arm blocked or simply average A-scans in one image and subtract it. Third, refractive index is a function of wavelength, therefore components such as lenses and fibers can cause dispersion with the usage of broadband light sources. Dispersion results in broadened coherence function. Yet it is a problem only when the amount of dispersion mismatch between the two arms, *i.e.* the two arms have different length of dispersion material. Obviously, one way to minimize dispersion mismatch is to have identical reference and sample arms. Alternatively, dispersion can be corrected in post-processing.

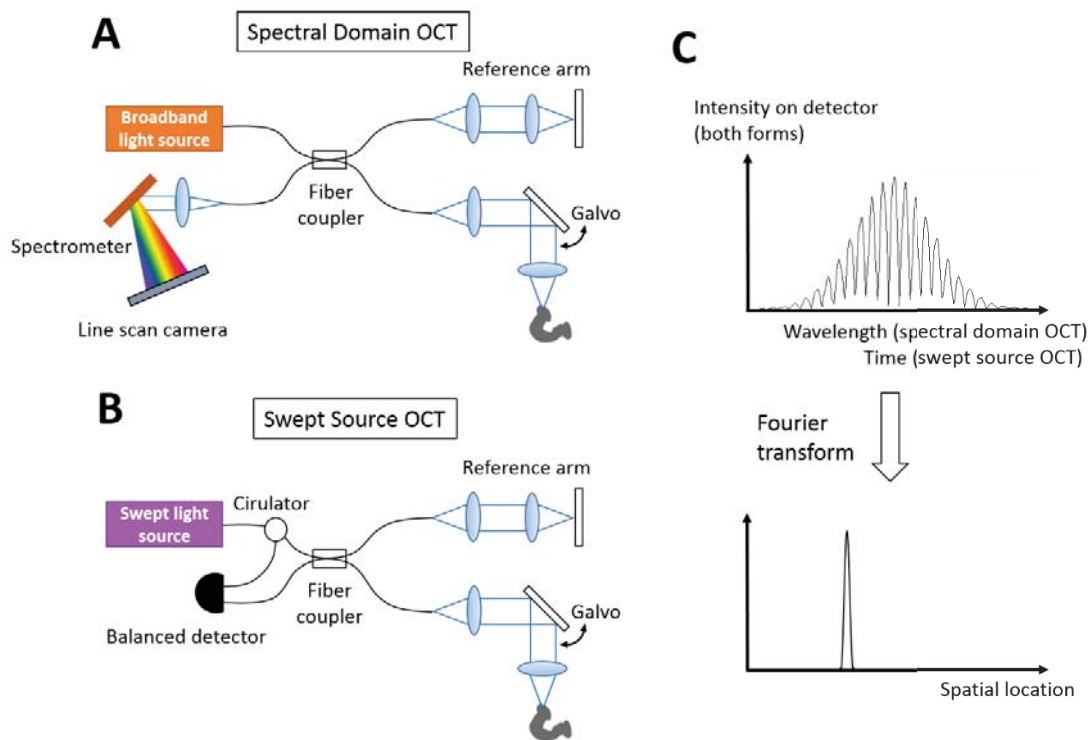


**Fig. 1.7** Two variations of Fourier domain OCT: spectral domain OCT and swept source OCT. A: schematic diagram of a spectral domain OCT system. It uses a broadband light source, a spectrometer and a line scan camera. B: schematic diagram of a swept source

OCT system. It uses a swept light source and a balanced detector. C: the Fourier relationship between spectral fringes and the spatial location of a scatter.

The main different component of an SSOCT system is the light source. Instead of using a broadband, static light source, SSOCT adopts a swept source laser, which sweeps through a range of frequencies with high speed. A regular photo detector is used to detect signals over time. By using balanced photo detector, heterodyne detection can be achieved and DC and AC background can be easily avoided. One sweep of the laser and corresponding signals collected from the detector generates one A-scan. SSOCT faces the situation as SDOCT in the need for linear-k correction and dispersion correction. The difference is that the linear-k correction is not simply an interpolation. Usually, a calibration interferometer is built to help resample data based on its evenly distributed fringes.

Both SDOCT and SSOCT are much faster than TDOCT and they are capable of real-time imaging, even real-time volume imaging. The speed of SDOCT is determined by the camera speed, which is currently in the hundreds kHz line rate range. The speed of SSOCT is determined by the light source. MHz Fourier Domain Mode Locked lasers has been used by a few research groups for a few years [129-131].

In addition to having a static reference arm, FDOCT has an advantage over TDOCT in SNR. In TDOCT, one point is acquired at each reference position. When fast imaging is desired, the time at each point is very limited therefore the signal at the detector is small. In FDOCT, the entire A-scan is collected, the coherent addition of signals from all detection channels results in a much larger signal power than the signal of each channel. This advantage of SNR was demonstrated by three different groups in 2003 [132-134]. Since then, FDOCT started to fully replace TDOCT.

### 1.3.3 Doppler OCT

Similar to ultrasound, Doppler OCT is a functional extension of conventional OCT for measuring flow. Based on the Doppler principle, backscattered light from a moving scatterer interferes with light from the reference arm, a Doppler frequency ( $f_{Dopp}$ ) shift occurs. The mechanism is described in Fig. 1.8.

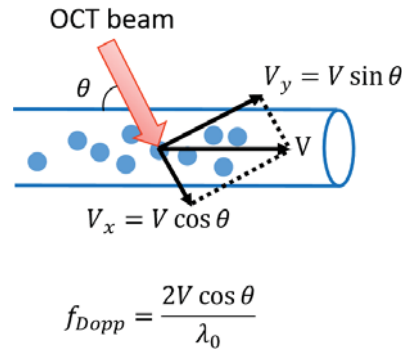


**Fig. 1.8** Flow velocity and the Doppler shift.

There is essentially no difference in the setup between Doppler OCT and OCT. Doppler OCT requires taking more data (several A-scans at each lateral location) at the image acquisition step and additional steps in post processing. After performing fast Fourier transform (FFT), as also required in regular OCT processing, averaged phase change over several A-scans can be calculated with  $\Delta\varphi(z) = \arg \left[ \frac{1}{N} \sum_{j=1}^N [f_j(z) f_{j+1}^*(z)] \right]$ , where N is the number of A-scans and j is the jth A-scan. The Doppler frequency is given by this equation:  $f_{Dopp} = \frac{\Delta\varphi}{2\pi t}$ , where t is the integration time of the camera. If the Doppler angle  $\theta$  is known, absolute velocity can be calculated. It is worth noting that Doppler OCT can only work for measuring flow velocity in solution that has scatters (e.g. blood) and cannot work for clear solution. Furthermore, there is always a range in which Doppler

frequency can be measured. Larger frequency will cause phase wrapping in the image. It is very obvious when phase wrapping happens because the flow profile (color image or trace) appears to have sudden changes of flow direction. Phase unwrapping can be achieved through manual unwrapping or unwrapping algorithms.

#### *1.3.4 OCT in embryonic research*

Imaging plays a significant role in developmental biology research. Conventional imaging modalities include histology, confocal microscopy, magnetic resonance microscopy (MRM), micro-CT, ultrasound, etc. However, each of these methods has drawbacks, such as the need for sacrificing the sample, low resolution and low speed. Embryonic research often requires high-resolution (the samples are small), high-speed (dynamic events), *in vivo* imaging (physiological conditions, longitudinal analysis), which cannot be achieved through a single imaging modality mentioned above.

OCT, which is noninvasive and captures data at high-resolution and high-speed, fills a niche for imaging structural and functional development of embryos. Throughout approximately 20 years, OCT has been used extensively in embryonic research. This section will discuss OCT applications in developmental biology studies, with the emphasis on the studies of the cardiovascular system. Another emerging imaging modality, light-sheet fluorescence microscopy features high-speed, high-resolution, large 3D volume imaging, low phototoxicity and has recently been applied to numerous embryonic studies. This imaging technology will be discussed later in this chapter.

In 1996, Boppart et al. demonstrated OCT imaging in developing structures in *Rana pipiens*, *Xenopus laevis*, and *Brachydanio rerio in vivo* and *in vitro*. OCT was able to resolve small structures, as validated with histology [135, 136]. Following these initial

attempts, cellular resolution OCT imaging was demonstrated *in vivo* in the *Xenopus laevis* tadpole [137]; developing zebrafish embryos were imaged with SDOCT and spectroscopic OCT [138-140]; the brain, gonads, facial features, vertebral column, blood vessels and the heart were imaged *in vivo* with 2.8  $\mu\text{m}$  SDOCT system [141]; mouse and rat embryos and vasculature were imaged with standard SDOCT and Doppler OCT under physiological or near physiological conditions [142-145]; numerous cardiovascular studies were also enabled with faster OCT systems.

The same group that first imaged *Xenopus* embryos also assessed the cardiovascular system of *Xenopus*. They imaged heart morphology in 3D using fixed embryos. Cardiac function was assessed from OCT optical cardiograms, which are M-scans from single locations of the heart [146]. This is because at that time TDOCT was used and the speed of the system is not fast enough for imaging B-scans and volumes of the beating heart. While some studies focused on cardiac morphology [147-149], others started to use Doppler OCT for blood flow assessment [150-152].

The technical development from TDOCT to FDOCT was a significant advance for embryonic cardiovascular research. 2D-over-time and 3D-over-time (4D) embryonic heart imaging became possible with SDOCT and post processing algorithms [153-159]. For example, different gating/synchronization algorithms were developed to realize high temporal resolution 4D imaging of early stage avian embryos [154, 156-160]. Our group used retrospective gating and rearranged images based on accurately knowing the heart cycle information or 2D image similarities [158, 159]. Happel et al. adopted rotational image acquisition and the M-scan of the central A-scan was used to rearrange images [157]. Blood flow profile in looping stage chick embryo heart has been achieved in 4D using

Doppler OCT [161, 162]. Other hemodynamics and vasculature imaged were also reported [155, 163-165]. Biomechanics such as wall motion, wall strain and shear stress were studied extensively in the chick embryo heart, especially in the outflow tract [166-173]. Abnormal cardiac structures and functions were observed with embryonic models of abnormal development [8, 155, 163, 174-176]. Using environmental control imaging chambers ensures physiological conditions for avian embryos, as well as providing the potential for longitudinal imaging [177-179]. Late-stage embryonic hearts (and embryo bodies) scatter light too much and exceed the depth penetration of OCT. Therefore optical clearing was introduced to increase the depth imaging range of OCT for phenotyping studies [180, 181]. Avian and murine cardiovascular systems were utilized in most of the studies because they are similar to human in both structural and functional aspects. Other animal models including *Drosophila* and *Xenopus* have advantages in that their genome is well-studied and accessible for manipulation.

In conclusion, OCT compensates other conventional imaging modalities in embryonic imaging with its high-speed, high-resolution, volumetric and *in vivo* imaging capabilities. The unique functional imaging ability of OCT has made it an important tool for monitoring early cardiac development. OCT is also ideal for fast phenotyping studies and defect screening for both early and late stages because it provides accurate structural imaging of the sample. Overall, OCT has made and will be making significant contributions in our understanding of normal and abnormal cardiogenesis.

#### **1.4 Light-sheet microscopy**

In the past 15 years, light-sheet microscopy became a popular tool for 3D fluorescence imaging in developmental biology. This section will discuss conventional and competing

3D fluorescence imaging modalities, concepts and components of light-sheet microscopy and applications of light-sheet microscopy in developmental biology.

#### *1.4.1 3D fluorescence microscopy*

3D fluorescence imaging is achieved through either physically or optically section the sample. Physical sections can have very high lateral resolution yet there is a limit to how thin the tissue can be sectioned due to the limitation in tissue slicing. This method is also limited in that it can only be applied to dead and fixed samples, which are often destroyed after the imaging. The cutting and mounting of the sample also requires time to develop the skill and a large amount of time and labor. Optical sectioning, in contrast, allows acquisition of images from sectioned planes from intact, live samples and it is usually fast in acquiring the data. Optical sectioning is usually achieved through discarding out-of-focus light (laser-scanning confocal microscopy) or exciting only at the interested plane (two-photon microscopy).

In laser-scanning confocal microscopy (LSCM), optical sectioning is performed using a pinhole in the detection path to filter out out-of-focus light. The entire depth of the sample is illuminated, yet only light at the focus is collected. One point of interest can be imaged without disturbance from scattering from other tissue layers. The laser beam is scanned in 2D to acquire an image. The size of the pinhole is determined by the desired thickness of the section. One limitation of LSCM is the depth penetration due to significant signal drop in deeper planes in heterogeneous samples. As the focal plane moves deeper into a scattering sample, confocality starts to fail due to aberration, and scattering of illumination in any direction degrades the imaging quality. Another drawback of LSCM is the amount of photobleaching and photodamage. Each plane/section is exposed many times and planes

imaged later are exposed much more than planes imaged earlier. Furthermore, a regular LSCM is slow because 3D volume sets are acquired point-by-point. The faster it moves from one point to another, the fewer photons reach the detector. This potentially sacrifice SNR for speed. A spinning disk confocal microscope is much faster, but it still suffers from the other drawbacks. Generally speaking, LSCM is suitable for imaging samples of thickness on the order of 100  $\mu\text{m}$  or less.

Two-photon (and multi-photon) fluorescence microscopy achieve optical sectioning by exciting only the volume of interest. This volume is the confined focal region where two-photon excitation happens. Other regions are excluded from the wavelength of light that can directly cause photobleaching and photodamage. The uses of doubled, infrared wavelength increases the depth penetration of imaging (several hundred  $\mu\text{m}$ ). Yet high power infrared laser light on the entire sample all the time may lead to severe damage of the specimen. Resolution can be a little lower because of the wavelength used. In addition, two-photon fluorescence microscopy share the same drawback in speed as LSCM.

#### *1.4.2 Light-sheet microscopy concept and scheme*

The idea of separating illumination and detection to orthogonal directions in a microscopy can be traced back to 1903. Yet the accelerated development of light-sheet microscopy systems did not happen until after 2004, when Huisken et al. published their work of zebrafish embryo imaging on *Science*.

The concept of all light-sheet-based microscopy is to illuminate the specimen from the side using a focused, thin sheet of light and detecting signals from this plane at an orthogonal direction, as illustrated in Fig. 1.9. This concept has remained the same during

the development of this technology, although many components have had undergone multiple variations.

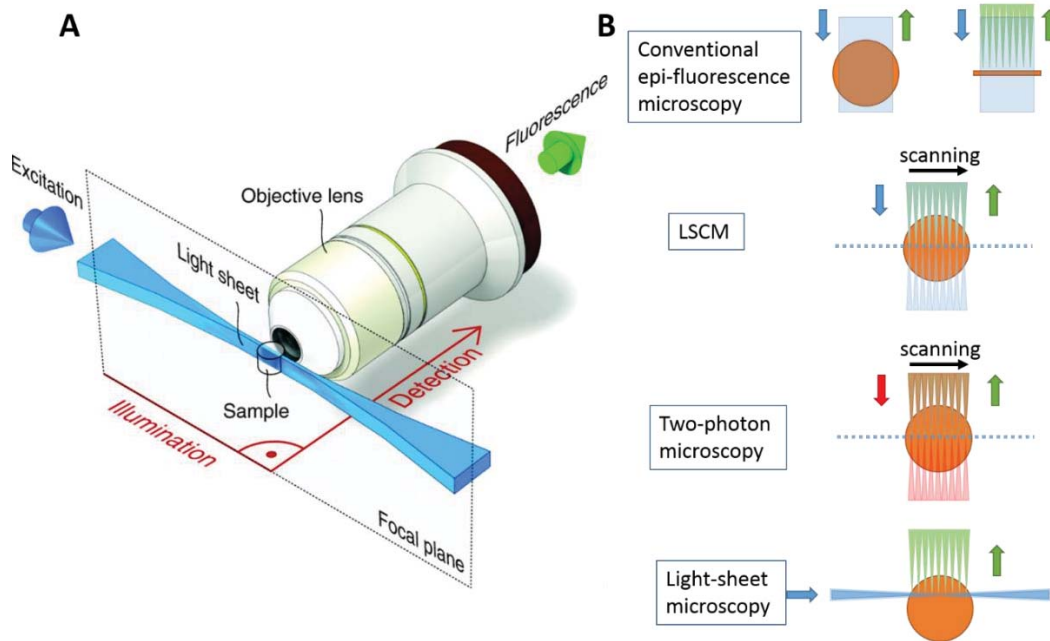


**Fig. 1.9** Schematic diagram of light-sheet microscopy. A: orthogonal illumination and detection in light-sheet microscopy. Adapted from Huisken and Stainier, 2009 [182]. B: illumination and detection scheme in epi-fluorescence microscopy, LSCM, two-photon microscopy and light-sheet microscopy. Epi-fluorescence microscopy does not have sectioning ability therefore tissue has to be physically sectioned. LSCM offers optical sectioning by rejecting out of focus light. Two-photon microscopy provides optical sectioning through confining excitation only at the focus. Both LSCM and two-photon microscopy require scanning for a line or a plane of image. Light-sheet microscopy achieves optical sectioning by only illuminating a plane at a time. No scanning is needed for 1D or 2D imaging.

#### 1.4.2.1 Illumination scheme

The first generation of modern light-sheet microscopes used cylindrical lenses in the illumination path to form a sheet of light on the sample [183]. Following the Gaussian beam theory, the light sheet is thinnest at the line of focus of the cylindrical lens and becomes wider on both sides. Because scattering within the sample causes shadows, the sheet was scanned in plane to reduce this effect [184]. In 2008, digital scanned light-sheet

microscopy (DSLIM) was developed. In DSLIM, a laser beam is directly focused using regular objectives and the beam is scanned in one dimension to form a sheet of light [185]. This change opened a door for many variations/modulations in the illumination of light-sheet microscopy. Extensions include Bessel beam light-sheet microscopy [186], two-photon Bessel beam light-sheet microscopy [187], Airy beam light-sheet microscopy [188], and structured illumination combined with light-sheet microscopy [189]. Another modulation of the illumination beam is creating interference patterns at the sample. Chen et al. reported a lattice light-sheet microscopy with resolution beyond the diffraction limit [190]. Because the energy is spread over the lattice, the peak intensity delivered to the sample is magnitudes smaller, therefore lattice light-sheet excitation benefits *in vivo* imaging significantly due to its exceptionally low phototoxicity and photobleaching.

The side further away from the light source has worse illumination profiles due to light scattering in the sample itself. In order to improve the imaging performance, light-sheet systems that use double-sided and even four-sided illumination were reported [191, 192]. Illumination and detection can be realized through the same objectives, or different objectives [191, 192].

#### *1.4.2.2 Detection scheme*

The detection system in light-sheet microscopy is usually composed of an objective, a tube lens and a high-speed camera. Depending on the number of fluorescence channels, multiple cameras may be needed [183]. In DSLIM, out-of-focus light can be further rejected with a confocal detection achieved through the camera's "rolling shutter" mode [193, 194].

The detection of 3D volume signals is usually performed by either moving the sample step by step [183, 191], or moving the illumination and detection plane simultaneously

[195-197]. Due to the physical movement of the sample, the 3D volume imaging speed of the first method is limited. DSLM often adopts the second method, by simply adding another scanning axis and a piezo stage on the detection objective [195]. To acquire images of an evenly illuminated sample, detection of a rotated sample and fusion of images in post processing is a routine procedure [195, 198, 199]. The second method is faster than the first one, yet the limitation is the speed of the piezo stage. In 2013, Fahrbach et al. built a system which uses an electrically tunable lens (ETL) in the detection path to change the detection focusing plane without physically moving anything in the detection path [200]. The speed of this system can achieve real-time volume imaging of beating zebrafish embryonic heart [200]. The current limitation of this system is that the ETL has an aperture of 10mm, which limits the resolution.

#### *1.4.2.3 Illumination-detection-coupled light-sheet microscopy*

Separating the illumination and detection offers flexibility in customizing the two paths incoherently, yet the separated 90 degree setup can be inconvenient in imaging traditionally prepared samples or dynamic imaging in larger live animals. Therefore continuous efforts have been made to couple the illumination and detection in light-sheet microscopy systems. To image neural activities *in vivo*, Holekamp et al. implemented an objective-coupled light-sheet microscope, in which the illumination path was minimized using fibers and small lenses and the illumination parts were physically coupled to the objective [197]. This illumination-detection arm was able to be placed at any angle with respect to the sample and was moved as one part therefore achieving 3D imaging. Another way of coupling illumination and detection is using only one objective lens for both paths. Work from two groups adopted the same idea, with a slightly different setup [201, 202]. In their designs,

an oblique sheet of excitation light is created by delivering a light sheet through the edge of the objective. Emitted light from the specific sheet is collected through another side of the same objective lens. The light sheet is scanned by a mirror or galvo prior to the objective for 3D imaging. More complicated optical components in the detection path are needed for correcting the oblique property of the images [201, 202].

#### *1.4.2.4 Advantages of light-sheet microscopy*

Compared to conventional 3D fluorescence imaging modalities mention above (LSCM and two-photon microscopy), light-sheet microscopy is advantages in its much higher speed, large field of view, deep penetration, low photobleaching and phototoxicity and the flexibility of determining illumination and detection profiles. All of these benefits are in addition to the possibility of achieving high-resolution in 3D. The low phototoxicity significantly benefits single-cell level imaging [190, 203]. Low photobleaching, large field of view and deep penetration made light-sheet an excellent tool for large, whole-organ level imaging, such as the entire brain neural network [204]. Light-sheet microscopy is also extremely suitable for imaging dynamics in live samples due to its high-speed and low phototoxicity.

#### *1.4.3 Light sheet microscopy application in developmental biology*

Early embryos are particularly well-suited for imaging with light-sheet microscopy because they are relatively transparent therefore whole embryos can be imaged [183, 185]. The first influential light-sheet microscopy publication involves imaging of embryogenesis and development of Medaka and *Drosophila* embryos for up to 3 days without any noticeable detrimental effect [183]. Keller et al. used DSLM to follow nuclei movement in intact normal and abnormal zebrafish embryos over the first 24 hours of their development.

Their comprehensive data of cell division and migratory tracks provided new insights into embryonic body axis identification [185]. The same group tracked early *Drosophila* embryos and built a database for a digital fly embryo [189]. 4D reconstruction of *in vivo* beating zebrafish hearts were demonstrated through different approaches [200, 205, 206]. Imaging of embryogenesis dynamics in *Caenorhabditis elegans* and *Drosophila* at subcellular resolution was demonstrated by lattice light-sheet microscopy [190]. A basic light-sheet microscope for developmental biology is easily accessible and affordable. Open-source platforms are available for researchers to follow to rapidly implement a light-sheet system [207-209].

### **1.5 Aims of this dissertation**

The overall objective of this dissertation is to overcome several current limitations of OM and push forward this technology towards becoming 3D and *in vivo*, as well as develop CHD models that could be studied using the novel OM technology. It was expected that the application of the improved OM technology to the study of the CHD animal models would provide us a better understanding of the mechanisms driving the development of the cardiac conduction system.

Aim 1, integrated OCT and OM system and 3D correction of conduction velocity. Conduction velocity measurement in OM suffers from the 2D projection feature of standard OM. We aim to combine the conduction imaging ability of OM with the 3D imaging feature of OCT to achieve 3D corrected, unbiased conduction velocity calculations in early embryonic hearts.

Aim 2, 4D OM with light-sheet microscopy. 2D images acquired with OM provide incomplete information regarding conduction in the 3D embryonic heart. Light-sheet

microscopy is capable of performing optical sectioning and therefore 3D imaging in the developing heart. We aim to develop a fast light-sheet fluorescence microscope optimized for achieving 4D OM, which enables circumferential, complete acquisition of developmental cardiac electrophysiology.

Aim 3, motion correction in OM based on nonrigid image registration. EC-uncouplers potentially affect the health of the sample and the characteristics of the signal. We aim to acquire useful electrophysiology information in beating embryonic heart without the influence of EC-uncouplers. Motion artifacts in 2D OM images of a beating embryonic heart will be corrected using an image registration based method.

Aim 4, development of a CHD model through CNCC-ablation in quail embryos. The etiology of CHDs has been of great interest. CNCC-ablated chick embryos were reported to have structural, functional and conduction system defects. We will discuss the development of a CNCC-ablation model and the resulted phenotypes at both early and late developmental stages.

## Chapter 2. Integrated OM and OCT

### 2.1. Introduction

Coordinated electrical activation and propagation plays an important role as a heart develops from a linear tube to a complicated four-chambered form, not only for initiating rhythmic contractions of cardiac myocytes for efficient blood pumping, but also for maintaining normal cardiac development [36, 37, 210, 211]. The developmental status of the heterogeneous conduction system in the embryonic heart can be characterized by parameters such as action potential (AP) morphology, activation sequence and conduction velocity. However, due to technology limitations, there has been a very limited number of studies of embryonic heart development that directly measure these electrophysiological parameters. Among the reported studies, AP morphology and activation sequence have been occasionally measured (*e.g.* [81, 83, 87, 212, 213]) while the more quantitative parameter, conduction velocity, has seldom been reported [80, 214-217]. Studies of gene knockout models have shown that defects in expression patterns of connexins, can both modify conduction velocity and lead to congenital heart defects (CHDs), such as ventricular septal defects and conotruncal heart defects [37, 218, 219]. These types of CHDs are common and sometimes life-threatening. As a result of limitations in technology to accurately measure conduction velocity, the mechanisms and the interplay between electrophysiology and heart structure are still poorly understood.

Measuring electrophysiology of the early embryonic heart is very challenging compared to doing the same for adult hearts due to the much smaller size of the embryonic heart. Yet optical mapping (OM) has shown great potential for overcoming the challenge. OM uses a voltage-sensitive fluorescent dye, an excitation light source, an appropriate filter

set, and a fast camera to image transmembrane potentials of the heart with high spatial resolution over a large field of view. Compared to electrode recording, OM enables simultaneous collection of signals from hundreds to thousands of sites, can be used to measure the same parameters (*e.g.* AP morphology, activation sequence and conduction velocity) while avoiding direct contact with delicate tissues. OM has made an enormous impact on the study of both adult and developmental cardiac electrophysiology and has advanced the understanding of mechanisms of electrical propagation [49, 81, 83, 87, 212, 220, 221].

One limitation of OM is that the technique collects information from a 3-dimensional (3D) surface as a 2-dimensional (2D) projection map. While AP morphology analysis and general activation sequence analysis are not affected by such projections, ignoring the curvature of the heart surface results in errors when calculating conduction velocity. Curvature is especially pronounced in early-stage tubular hearts and can vary greatly at different developmental stages and between individual embryos at similar stages. More importantly, in some disease models, affected hearts may differ from healthy embryonic hearts in size and curvature (*e.g.* abnormal looping). Efforts have been made to address this problem in adult heart models. One method is to immobilize the surface of the heart against a glass plate to reduce curvature [98]. This is not applicable to embryo models because embryonic hearts are fragile and very small ( $< 2 \text{ mm} \times 2 \text{ mm}$ ). Another example is panoramic OM, which uses a rotating geometry camera to capture the surface shape of the heart [107-109]. However, because embryonic hearts are very small and the heart curvature is much more complicated than the cone-shaped adult heart, this solution is also not well suited. Therefore, at present, estimation of conduction velocity in embryonic hearts based

on projected 2D mapping is difficult and error-prone. This problem complicates any comparisons made between different hearts and even between different regions of the same heart. As a result of these difficulties, measured conduction velocities of early embryonic hearts utilizing OM have seldom been reported, and the reported measurements are estimations without considering the 3D curvature of the heart [80, 214, 217]. Thus an improved method, which can take the 3D curvature into consideration, is needed to obtain accurate and reproducible conduction velocity measurements.

Optical coherence tomography (OCT) is a powerful non-invasive imaging modality capable of characterizing 3D structure. Since OCT imaging can provide high resolution (2-30 $\mu$ m), sufficient tissue penetration (1-3mm), adequate field of view, and extremely high speed, it is well suited for structural and functional imaging of cardiac development models *in vivo* and *ex vivo* [136, 148, 153, 154, 156, 173, 174]. OCT is particularly well suited for accurately measuring the 3D morphology of the tubular early embryonic heart [136, 148, 153, 154, 156, 174, 222]. Furthermore, OCT uses infrared light, which does not interfere with the visible light used for OM, and it does not require special preparation or orientation of the sample. In combination with OM, OCT can provide the 3D structural data needed to accurately measure conduction velocity in the presence of complicated curvatures.

In this chapter, an integrated OCT and OM imaging system that is capable of imaging structure and conduction signals simultaneously is described. Corrected conduction velocity measurements were demonstrated in looping embryonic quail hearts based on 3D surfaces provided by OCT. Looping embryonic hearts are undergoing important structural and electrophysiological transitions such as the initiation and development of the atrioventricular junction (AVJ) and atrioventricular (AV) delay. Also, the structure of the

heart is becoming more convoluted as it loops from a C- to an S-shape [155, 178, 223]. 3D-corrected conduction velocity calculations will eliminate the underestimation of conduction velocity inherent to 2D optical mapping and therefore provide more accurate measurements and benefit our understanding of cardiac conduction system development.

## **2.2 Material and Methods**

### *2.2.1 Embryonic heart preparation*

Fertilized quail eggs (*Coturnix coturnix*, Boyd's Bird Company, Inc., Pullman, WA) were incubated in a humidified, forced draft incubator (G.Q.F. Manufacturing Co., Savannah, GA) at 38°C for 50 hours. Three Hamburger–Hamilton (HH) stage 15 quail embryos [47, 224] were removed from their eggs. The embryonic hearts were excised and stained with 10 $\mu$ M of di-4-ANEPPS (Life Technologies, Carlsbad, CA) in 300  $\mu$ L Tyrode's solution (Sigma-Aldrich, St. Louis, MO) for 12 minutes at room temperature. The embryonic hearts were then placed in the imaging chamber filled with 1 ml of Tyrode's solution containing 10  $\mu$ M of cytochalasin D (Sigma-Aldrich) to suppress myocardial contraction. The experiment environment was maintained at 38 °C during the subsequent imaging steps.

### *2.2.2 Design of a compact OCT scanner*

A compact OCT scanner was designed and built in order to fit into the limited space of the incubator to image the heart structure. The optical design was performed in Zemax (Zemax, LLC., Kirkland, WA). The scanner was designed to have switchable resolution and working distance through changing objective lenses with quick release magnetic mounts. Four sets of objective lenses were modeled to achieve 12  $\mu$ m to 34  $\mu$ m resolution (the FWHM of the point spread function at the focus). All lenses were commercially available.

This has made the scanner economical and convenient to be reproduced. The scanner was designed to be quasi-telecentric for optimum performance in scanning. To be fully telecentric, the scanning mirror needs to be placed at the front focus of the following optics. Here with two scanning mirrors, it is impossible to place both mirrors at the focus of the following optics. Therefore the design of quasi-telecentric, in which the focus of the following optics was at the middle of the two scanning mirrors was utilized. The quasi-telecentric feature can only be applied to one objective set to not further complicate the mechanical design of the scanner. Therefore the quasi-telecentric design was applied to the most often used objective, which has the highest resolution setting. The resolution, selected commercial lenses, scanning range and working distance of each set are listed in Table 2.1. The point spread function at the focus of the objective lens was validated using a beam profiler (DataRay Inc., Redding, CA) and an example is shown in Fig. 2.2.

The mechanical design of the compact scanner was accomplished using mostly commercially available mounts and several custom parts designed with SolidWorks (Dassault Systèmes SolidWorks Corporation, Waltham, MA). A main board was designed to mount all pieces together and small stages were designed to ensure a common optical axis. A complete part list and mechanical drawings for the custom parts are attached in Appendix B.

Lens set	Resolution	Commercial lens		X range (<5%)	Y range (<5%)	Working distance
1	12 $\mu\text{m}$	A397TM-C	AC254035C LA1608C(75)	4.7mm	4.7mm	17mm
2	17 $\mu\text{m}$	A397TM-C	AC254030C	3.2mm	4.8mm	23mm
3	24 $\mu\text{m}$	A397TM-C	AC254045C	5.2mm	6.6mm	39mm
4	32 $\mu\text{m}$	A397TM-C	AC254060C	7.6mm	10mm	54mm

**Table. 2.1** Modeling results from four settings of the resolution switchable scanner.

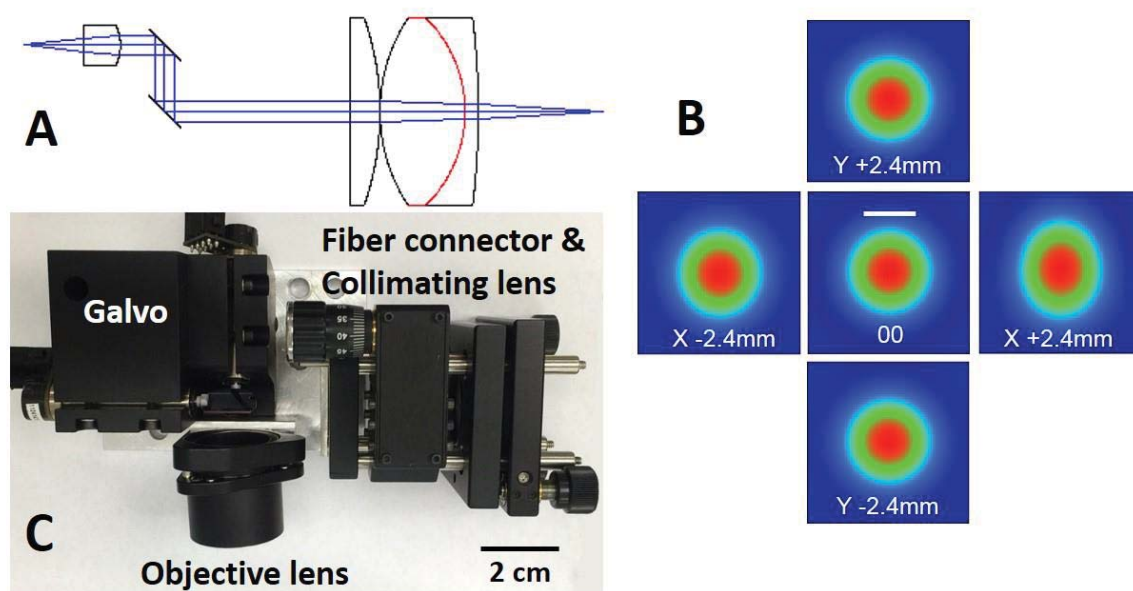


**Fig. 2.1** A: compact scanner design in Zemax. B: point spread function modelled by Zemax (the 12  $\mu\text{m}$  resolution setting). 00: light beam centered.  $X \pm 2.4\text{mm}$ : scan in X direction.  $Y \pm 2.4\text{mm}$ : scan in Y direction. Scale bar: 12  $\mu\text{m}$  C: physical setup of the compact scanner.

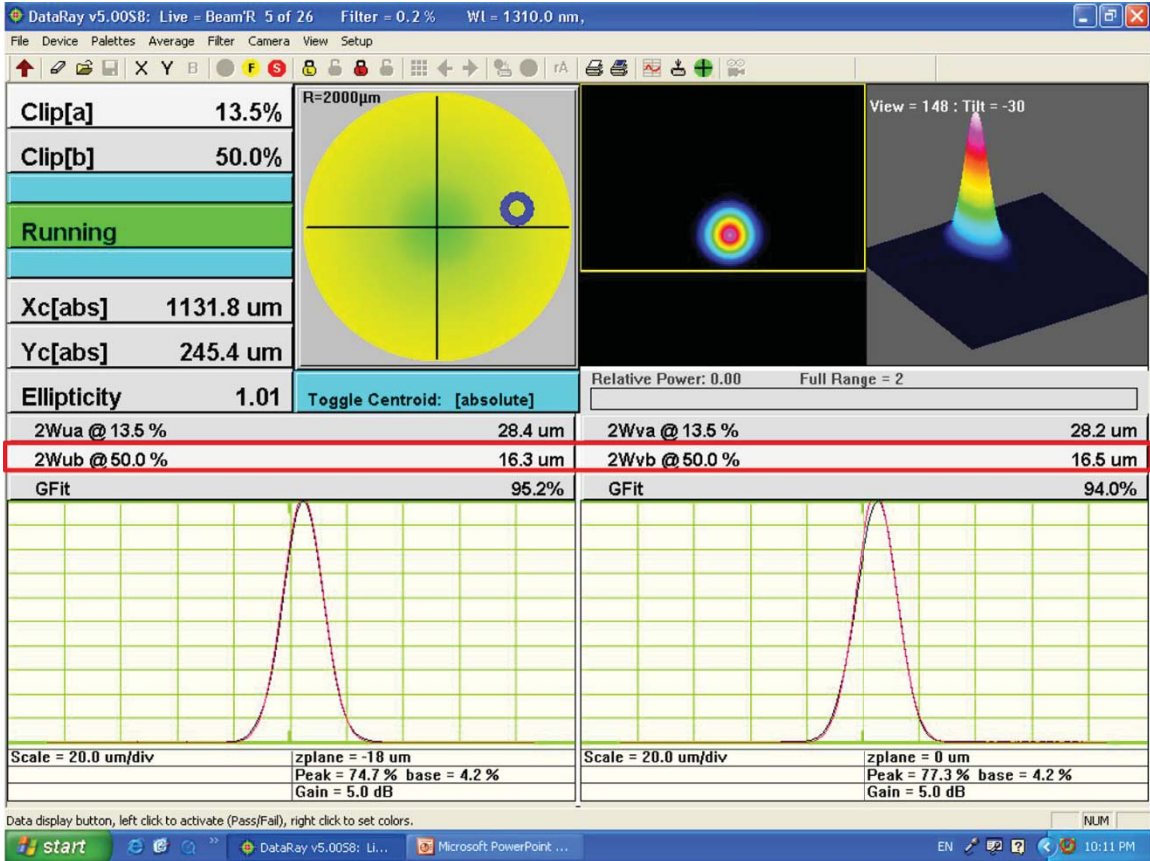


**Fig. 2.2** An example image of beam profile analysis result acquired at the focus of the compact scanner (17  $\mu\text{m}$  resolution setting). The FWHM of the beam profile was highlighted with the red box. The beam profile was fitted to Gaussian profiles in two cross sections and ellipticity was reported in the figure.

### 2.2.3 Integrated OCT/OM system

To image both the structure and electrical activity, we developed a custom integrated OCT/OM system (Fig. 2.3). The custom-built OM system[225] utilized a broadband LED light source (SOLA Light Engine, Lumencor, Beaverton, OR), which provides high intensity, low noise, broadband illumination. A filter and dichroic mirror set (Chroma Technology, Bellows Falls, VT) was used with an excitation wavelength of  $510 \text{ nm} \pm 40 \text{ nm}$ , an emission wavelength of  $685 \text{ nm} \pm 40 \text{ nm}$  and dichroic mirror cutoff wavelength of  $560 \text{ nm}$ . A low noise, high dynamic range EMCCD camera (iXon3 860, Andor

Technology, South Windsor, CT), and an upright microscope (Axio Scope.A1, Carl Zeiss AG, Oberkochen, Germany) were used for signal recording. Demagnifying optics were utilized to control the field of view. The OM system records  $128 \times 128$  pixels at a maximum frame rate of 500 Hz. Depending on the field of view required by the sample, either a 10X objective lens ( $880 \mu\text{m} \times 880 \mu\text{m}$ , C-Apochromat 10X/0.45 M27, Carl Zeiss AG, Oberkochen, Germany) or a 5X objective lens ( $950 \mu\text{m} \times 950 \mu\text{m}$ , Fluar 5X/0.25 M27, Carl Zeiss AG) was employed. The OM imaging system was placed above an imaging chamber, which uses a coverslip as the bottom to hold the sample.

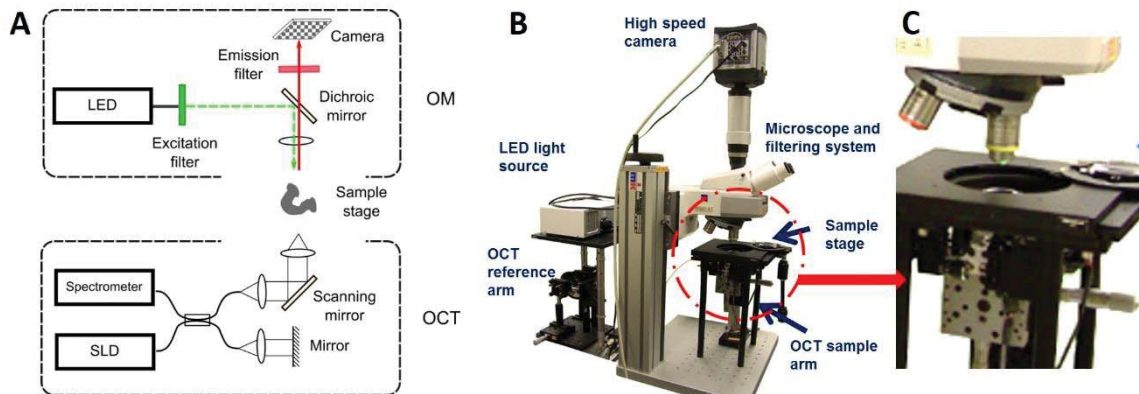


**Fig. 2.3** A: schematic diagram of the integrated OCT/OM system. B: physical setup of the integrated system. LED: light-emitting diode. SLD: superluminescent diode. C: zoom in view of the red circle in B. A clear view of the integrated OCT and OM system arrangement near the sample.

The OCT portion of the integrated system was a custom built spectral domain OCT system[128] with a compact scanner located under the sample stage. The OCT light source has a center wavelength at 1310 nm and a bandwidth of 75 nm full width half maximum. The axial and lateral resolutions of the system were both  $\sim 10 \mu\text{m}$  in air. This system utilizes a linear-in-wavenumber spectrometer as previously described [128]. The line scan camera (Sensors Unlimited, Princeton, NJ) in the OCT spectrometer operates at 47 kHz. The OCT system images through the transparent coverslip bottom of the imaging chamber and the

tissue to acquire full 3D structures. The OCT scanner was tilted  $\sim 5^\circ$  to reduce specular reflections.

The entire system was enclosed in a box to avoid ambient light exposure and to maintain the temperature during experiments. Two 50 W heaters (McMaster-Carr, Aurora, OH) were used for heating and the temperature was monitored by a temperature controller (TC-344B, Warner Instruments, Hamden, CT) with the sensing tip in the solution near the sample.

#### 2.2.4 Image processing and data analysis

Image processing and data analysis were performed with custom software written in MATLAB (MathWorks, Natick, MA). A cumulative normal distribution function was fit to the upstroke of each AP trace. Activation time for each pixel was determined as the inflection point of the cumulative normal distribution function. The middle point of the AP upstroke is conventionally used as the activation time. An electrical activation map was obtained based on the activation time at each pixel.

OCT volume images were acquired simultaneously with OM images. OCT images were corrected for aspect ratio and imaging angle, using the surface of the chamber glass bottom as the reference. Next, the OCT volume images of the heart were projected to an *en face* plane. The OCT *en face* projection image was registered to one of the OM images using a fully automatic partial-affine transformation to match the size, orientation and position [226, 227]. The transformation parameters were two scale parameters (x and y directions), two translation parameters (x and y directions) and one in-plane rotation parameter. The OCT volume image was then transformed accordingly based on the transformation matrix. The OCT volume images were auto-segmented using Amira

(Visualization Sciences Group, FEI) to generate binary masks for surface renderings. The activation map was then projected to the 3D volume mask for geometrically accurate visualization.

### 2.2.5 3D conduction velocity correction algorithm

The binary masks were also used to create a heart surface height map from the top surface, which was used to correct conduction velocity calculations. We followed conventional methods for calculating the 2D ( $x$  and  $y$ ) conduction velocity component vectors, then used the OCT data to determine the third ( $z$ ) velocity component vector (Fig. 2.4). From the OM activation map, 2D conduction velocities were calculated based on the activation time ( $t$ ) gradient vectors in the  $x$  and  $y$  directions which are defined as:

$$\begin{aligned} g_x &= \partial t / \partial x; & g_y &= \partial t / \partial y \\ \vec{g}_{2D} &= \vec{g}_x + \vec{g}_y \end{aligned} \quad 2-1$$

The default window size for calculating gradients was  $3 \times 3$  pixels and the window size was adaptively enlarged with increasing conduction velocity. A high conduction velocity means a low activation time gradient, which generally requires a larger window size for accurate measurement. The velocity vector  $\vec{v}_{2D}$  has the same direction as the gradient vector  $\vec{g}_{2D}$  and its magnitude is the reciprocal of the gradient magnitude  $g_{2D}$ . As described previously [91],  $v_x$  and  $v_y$  were derived as:

$$v_x = g_x / g_{2D}^2; \quad v_y = g_y / g_{2D}^2 \quad 2-2$$

3D correction of the activation map was performed by projecting the 2D activation map from OM onto the matched 3D surface height map acquired from OCT, so that each OM pixel was assigned an associated  $z$ -position value. For each pixel of the height map,

the four neighboring pixels were used to estimate the vector normal to the heart surface,  $\vec{n} = \vec{n}_x + \vec{n}_y + \vec{n}_z$ , by Newell's method [228]. The magnitude of the velocity in the z direction ( $v_z$ ) was derived from  $\vec{n}$  and the known velocity component vector magnitudes  $v_x$  and  $v_y$  using the assumption that the direction of the 3D conduction velocity vector  $\vec{v}_{3D}$  is perpendicular to the surface normal direction, so that

$$\vec{n} \cdot \vec{v}_{3D} = n_x \cdot v_x + n_y \cdot v_y + n_z \cdot v_z = 0,$$

$$\text{and } v_z = -\frac{n_x \cdot v_x + n_y \cdot v_y}{n_z}.$$
2-3

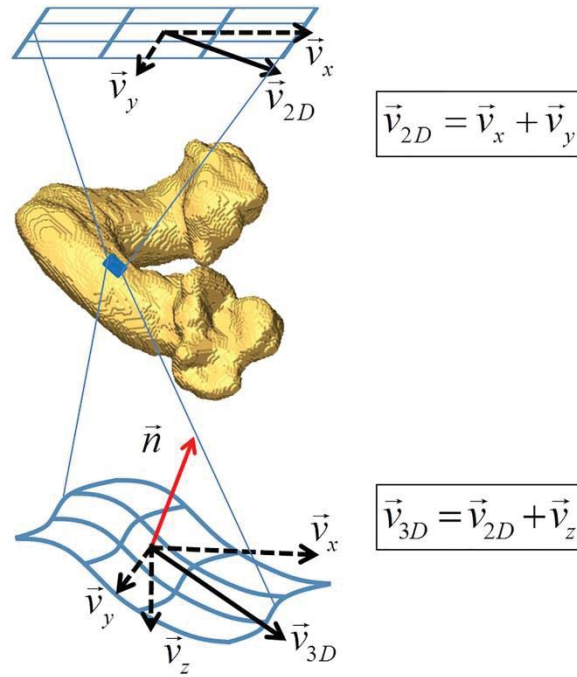


**Fig. 2.4** Diagram illustrating velocity calculations with the traditional 2D projection method (top) and 3D corrected method (bottom). Fluorescent signals were collected from a 3D heart surface and projected to a 2D plane. This diagram uses a small  $3 \times 3$  patch on the heart surface to demonstrate the process. In the traditional 2D calculation, only velocity components in the projected plane ( $\vec{v}_x, \vec{v}_y$ ) were calculated. In the 3D corrected calculation, 3D structure was used to find the normal vector ( $\vec{n}$ ) by Newell's method. Then the velocity component in the height dimension ( $\vec{v}_z$ ) was calculated and finally 3D conduction velocity ( $\vec{v}_{3D}$ ) was computed.

It follows that the 3D corrected conduction velocity at each pixel is  $\vec{v}_{3D} = \vec{v}_x + \vec{v}_y + \vec{v}_z = \vec{v}_{2D} + \vec{v}_z$ . At each pixel in the region of interest, the 3D corrected conduction velocity was calculated, and the magnitude was mapped to the corresponding voxel on the 3D OCT surface. Fig. 2.4 uses a 3×3 pixel area on the 3D heart surface to illustrate the correction process for 3D conduction velocity.

### 2.2.6 Validation and Evaluation

The ability to accurately measure sample orientation from OCT volumes was validated by imaging a plastic slide at various known angles. The plastic slide was oriented at preset angles (0° to 25° at 5° increments) and imaged with OCT. At each angle, a 4.3 mm × 1.5 mm × 0.2 mm volume was recorded by OCT, and the orientation was determined from the normal that was computed using Newell's method, as described above. Each angle was measured multiple times to estimate the error.

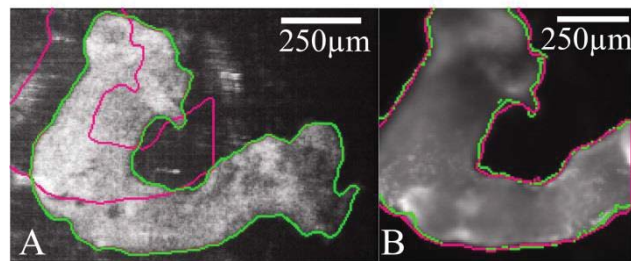
Quantitative comparisons were made between 2D (uncorrected) and 3D (corrected) conduction velocity maps. To evaluate the amount of correction from 2D to 3D-corrected conduction velocity, the relative difference (between 2D and 3D) at each pixel was calculated as  $CV_{difference} = (v_{3D} - v_{2D}) / v_{2D}$ . The result represents the necessary percent correction from 2D to 3D. A conduction velocity correction map was generated for each embryonic heart.

Direct validation of accurate conduction velocity is impossible because there is no gold standard method, and none of the existing methods take 3D distances into consideration. Therefore 2D and 3D calculation results were used as a self-validation. 2D projection can cause non-uniform underestimations because of local structure differences.

Therefore the 2D method can potentially produce artifacts that are not physiologically valid and the 3D-corrected method should be able to eliminate these artifacts. Two regions that were expected to have the same conduction velocities but different slopes were selected for comparison. Their 2D and 3D conduction velocities were measured as averaged values from  $\sim 100$ -pixel regions of interest.

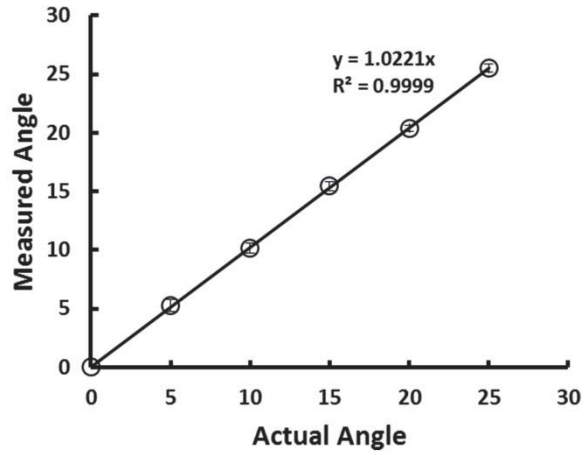
### 2.3 Results

The OCT *en face* projections were registered to OM image sets to accurately match the position, orientation and scale, as described in Methods 2.2.4. As shown in Fig. 2.5, the automatic partial-affine transformation adequately registers the two image sets.



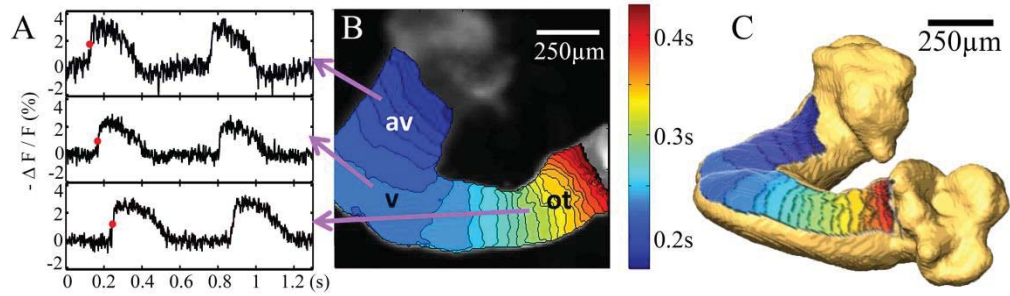
**Fig. 2.5** OCT/OM registration. Panel A shows an OCT *en face* projection gray scale image of a HH stage 15 embryonic heart before being registered to an OM image. The green contour represents the boundary segmentation of the OCT *en face* projection and the magenta contour represents the boundary segmentation of the corresponding OM image overlaid on the OCT *en face* projection. Panel B shows an OM image which served as the reference for image registration. After registration, boundary contours of OCT (green) and OM (magenta) images can be seen to correspond well.

Fig. 2.6 shows the OCT measured angles versus actual angles from the plastic slide experiment to verify OCT measurement of surface orientation. Angles were accurately measured and the errors were all within  $\pm 0.5^\circ$ .



**Fig. 2.6** Results of OCT measuring various orientations of a flat surface using Newell's method. Standard deviation bars are shown inside the circles.

An action potential trace was recorded at each pixel in an OM image. Representative action potential traces from 3 different regions of the heart are shown in Fig. 2.7A. The activation time (defined as the mid-point of the upstroke) was determined at each pixel (red marks on the traces in Fig. 2.7A). An activation isochrone map which displays the activation time at every pixel is shown in Fig. 2.7B. The AVJ and the outflow tract exhibit denser isochrones, meaning slower propagation of action potentials, compared to the ventricular region, which displays sparser isochrones and higher conduction velocity. The same activation isochrone map is projected and overlaid onto the 3D OCT surface rendering of the same embryonic heart in Fig. 2.7C. The geometrically correct activation map can now be visualized in the context of 3D features such as the surface curvature and the looping of the heart.



**Fig. 2.7** Panel A shows raw action potential traces of 3 different pixels from 3 different regions of the heart tube, indicated by arrows from panel B.  $\Delta F/F$  represents the percent change in raw fluorescence signals. The red dot in each trace represents the activation time. Panel B shows a 2D electrical activation map overlaid on a gray scale OM image. Colormap blue to red represents the sequence of activation from early to late. Each isochrone represents 10 milliseconds. Panel C shows the activation map overlaid on the 3D OCT volume surface rendering. This panel shares the same colormap as Panel B. av-atrioventricular junction; v-ventricle; ot-outflow tract.

In order to compute 3D conduction velocities from 2D projections, the  $z$  position of each OM pixel was determined from a co-registered height map generated from the corresponding OCT surface rendering. Three embryonic hearts were imaged, and their height maps, conduction direction quiver maps, 3D-corrected conduction velocity maps, conduction velocity correction maps and percent correction histograms are shown in Fig. 2.8. Height maps (Fig. 2.8A) were computed from 3D OCT volumes after being registered to OM images. From the OCT height maps, the orientation of each heart can be clearly distinguished. Heart 2 was imaged from the ventral side, while hearts 1 and 3 were imaged from the dorsal side but from different angles. Because of orientation differences, the curvatures apparent in the three hearts are not identical. For example, heart 1 shows steep slopes at the AVJ and moderate slopes at the outflow tract. Heart 2 has mostly flat regions at the AVJ, the ventricle and the outflow tract, while slopes are steep between these regions. In heart 3, the AVJ is mostly obscured due to the orientation of the heart, while the

ventricular region is flat and the outflow tract slopes moderately. Quiver maps were generated to indicate the propagation direction of electrical conduction (Fig. 2.8B). The overall conduction direction was parallel to the heart tube, as expected.

3D-corrected conduction velocity maps of the 3 hearts are shown in Fig. 2.8C. All hearts exhibit the lowest conduction velocity at the outflow tract ( $3.6 \pm 0.2$  mm/s), higher conduction velocity at the AVJ ( $6.1 \pm 1.3$  mm/s) and the highest conduction velocity at the ventricle region ( $14.3 \pm 3.8$  mm/s). The conduction velocities at the AVJ and the outflow tract are generally uniformly distributed. The ventricle region shows more heterogeneity. The inner curvature of the ventricle region has much lower conduction velocity (2-10 mm/s) than the outer curvature (10-30 mm/s). Fig. 2.8D shows maps of the percent change in conduction velocity resulting from the 3D correction procedure. All correction values are non-negative because the 2D projection error can only result in an underestimation bias, not overestimation. The correction values vary widely from 0% to more than 100%. The corrections needed for each heart are very different from one another, due to the difference in the morphology of the hearts and/or their orientation when imaged. Heart 1 needed corrections over most of the field of view. Heart 2 mainly needed corrections at the transitions of AVJ to ventricle and ventricle to outflow tract. Heart 3 needed the least correction, mostly at the outflow tract. Histograms of the percent corrections applied to all pixels in each heart with bins of 5% are shown in Fig. 2.8E. In all three hearts, most of the pixels needed small corrections (0% - 20%). 41%, 37% and 12% of the pixels from hearts 1, 2 and 3, respectively, required corrections greater than 20%.

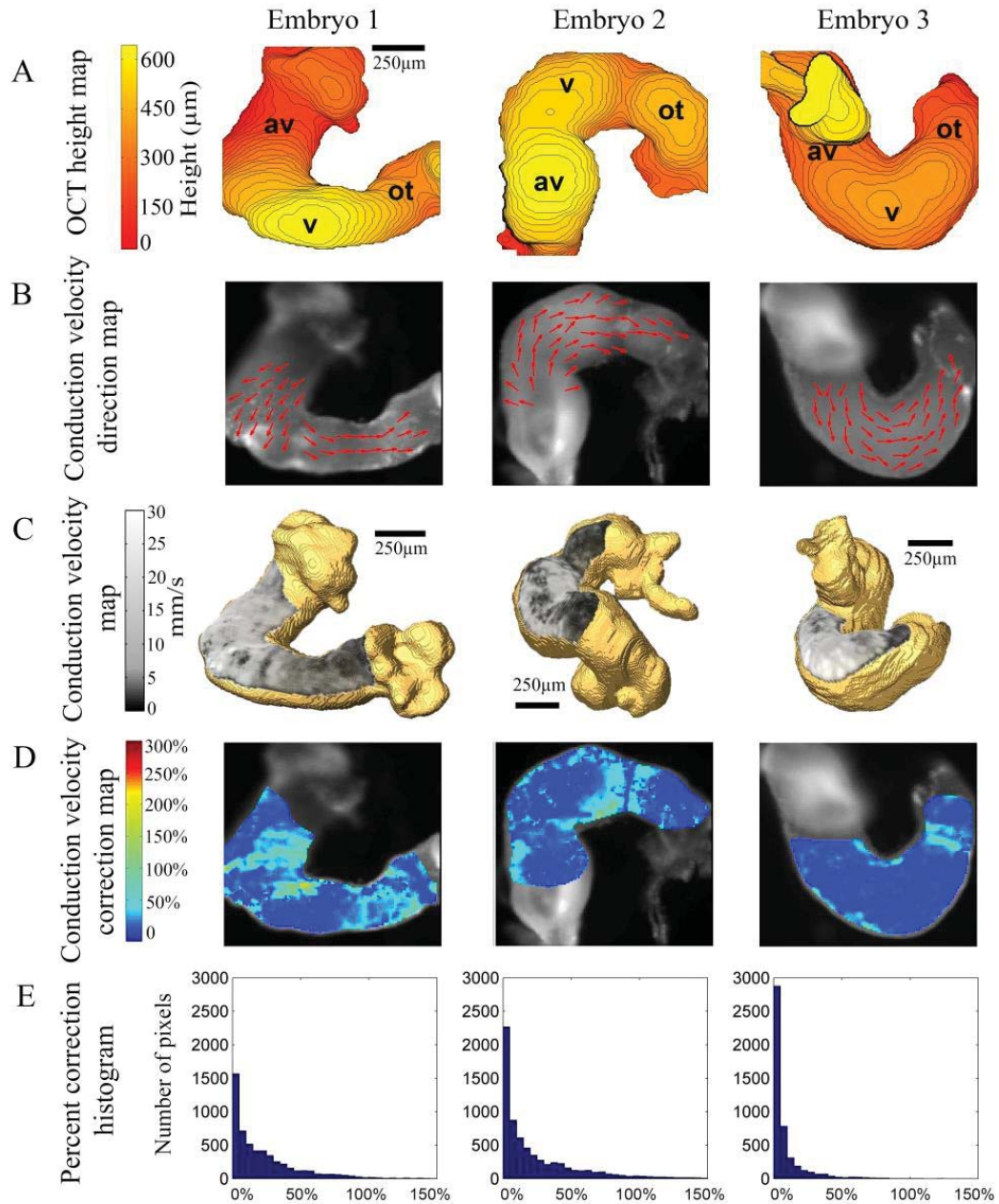


**Fig. 2.8** Three embryonic hearts were imaged and processed. Panel A shows surface height maps acquired from OCT volume rendering. The relative height of each pixel in microns is represented by the colormap and each contour line represents  $15\ \mu\text{m}$ . Panel B shows quiver maps of conduction direction through the hearts. Normalized and  $10 \times 10$  binned arrow heads indicate the directionality only. Panel C shows 3D-corrected conduction velocity maps overlaid on the surfaces of 3D OCT volume rendering. Panel D shows conduction velocity magnitude correction maps showing percent correction from the 2D values to the 3D corrected values. Panel E shows histograms of the necessary correction amount needed for each heart with bins of 5%. av- atrioventricular junction; v-ventricle; ot-outflow tract.

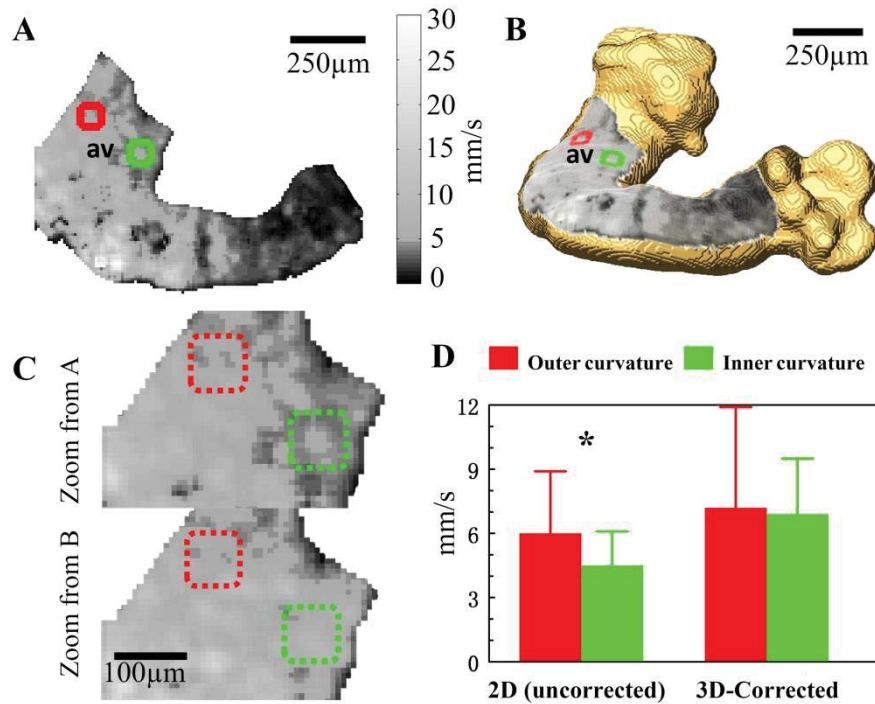


**Fig. 2.9** Panels A and B are 2D (uncorrected) and 3D-corrected conduction velocity maps, respectively, for embryonic heart 1. Square regions of interest from the inner (indicated in green) and outer (indicated in red) curvatures were selected for comparison. Panel C top and bottom are magnified, corresponding images of the AVJ from panels A and B. Panels D shows the averaged conduction velocity of the marked regions in panel C. The results are presented as mean  $\pm$  S.D. Conduction velocity values were compared using Student's *t*-test (\*  $p < 0.0001$ ). av- atrioventricular junction.

2D calculations can produce artificial features, which may lead to misinterpretation of the data. An example is shown in Fig. 2.9. The AVJ, which is a straight tubular structure, is expected to have a uniform conduction velocity across the tube. In the 2D conduction velocity map (Fig. 2.9A, magnified in 7C), the inner (red) and outer (green) curvatures of the AVJ appear to have a significant difference while in the 3D conduction velocity map (Fig. 2.9B, magnified in 7C), they are revealed to be approximately the same. Comparing the regions of interest marked in green and red, the inner curvature showed a 25% lower

conduction velocity than the outer curvature based on the 2D map (Fig. 2.9D). This apparent difference is statistically significant, but it is absent in the 3D-corrected map (Fig. 2.9D), indicating that the difference is an imaging artifact of the 2D calculation, not a true difference.

#### **2.4. Discussion**

We have presented an integrated OCT and OM system. This, for the first time, provides the means to record and directly co-register structural and electrophysiological images of embryonic hearts simultaneously. We have furthermore demonstrated the capability of the system to recover the velocity vector in the  $z$  direction and compute a 3D conduction velocity map that is corrected for surface curvature in the embryonic heart. Imaging samples with the integrated OCT/OM system is fast (*i.e.* no longer than imaging the sample with one modality). Because the two imaging systems are integrated, image registration is very straightforward, which provides high accuracy and saves time in post-processing. Fast imaging is especially important for high-throughput experiments, and therefore is advantageous for phenotyping studies.

The high-resolution 3D structural OCT images directly correlated with OM are also useful in a qualitative way for interpretation of OM data. OM utilizes high NA objective lenses, and out-of-focus regions of the complex heart structure can be difficult to identify. Sometimes, the tissue may fold and overlap, and useful signals can only be recorded from the top surface. The tissue overlap can be difficult to interpret in 2D fluorescence images. With correlated volumetric OCT, the 3D morphology of the samples are clearly visualized and regions of invalid OM data can be readily excluded from analysis.

The process of 3D correction of conduction velocity was carefully verified step-by-step to avoid introducing additional errors or noise to the conduction velocity measurement. First, the OCT system was calibrated carefully and angle measurement verification experiment results (Fig. 2.6) indicate that OCT measures angles correctly with negligible errors. The OCT sample arm scanner was built based on a quasi-telecentric design similar to that previously described [229]. This design minimizes off-axis aberrations, which is a potential cause of inaccurate length and angle measurements. A metal mesh was imaged to verify uniformity across the field of view. Identical on-axis and off-axis grid sizes were observed (data not shown). Second, to avoid deforming the OM images from which the conduction velocity measurements were made, OCT images were registered to OM images instead of the other way around. Boundary segmentation curves on the registered OCT image and the reference OM image correspond well (Fig. 2.5). The registration error on the edge is the most severe and the registration away from the edge will be more accurate. Third, the accuracy of the height map from OCT images is also directly related to the volume segmentation. Automatic segmentation using Amira software was employed with small manual corrections applied after automatic segmentation (total time less than 10 minutes). The performance of the automatic segmentation with correction was always satisfactory when compared to careful manual segmentation.

The heart surface height maps acquired from OCT provides a direct view of the slopes in depth ( $z$ ) and an estimation of the amount of conduction velocity correction needed (Fig. 2.8A). Steeper slopes generally result in larger errors in 2D measurements. However, some steep regions do not necessarily require large corrections, as can be seen by comparing the height maps in Fig. 2.8A with the conduction velocity correction maps in Fig. 2.8D. The

reason is that only  $z$  gradients in the direction of AP propagation cause errors and require correction, while the slopes perpendicular to the direction of conduction do not cause errors. The height maps in Fig. 2.8A and conduction direction maps in Fig. 2.8B together explain the patterns in the conduction velocity correction maps in Fig. 2.8D.

Several other observations can be made from the conduction velocity correction maps and histograms in Fig. 2.8D and E. First, all the corrections are positive, confirming that the 2D maps only underestimate conduction velocity because 2D projections only underestimate distances. Second, the corrections required were not uniform between hearts or even within the same heart. This is related to the morphology of the heart and the orientation of the heart when it was imaged. Third, the correction value histograms from the 3 embryonic hearts show that most pixels do not need much correction because they are either at a flat region, or a region tilted perpendicular to the conduction velocity direction. Also, a wide range of correction values were needed, mainly between 0% to 100%. Corrections larger than 100% are rare, as larger corrections would only be required with a tilt angle greater than  $60^\circ$  along the conduction direction. Structures that have angles larger than  $60^\circ$  will most likely result in blurry OM pixels due to being out of focus and are likely to be excluded during OM image processing.

Among the 3 hearts, heart 2 generally had lower conduction velocity (Fig. 2.8C), which may be because heart 2 was imaged from a different side or because it was less healthy. In all the hearts, the inner curvature of the ventricle regions have lower conduction velocity than the outer curvature because the outer curvature has much longer distance for the conduction wave to travel than the inner curvature. In the middle of each heart, there are some small patches of very low apparent conduction velocity values that are distinct

from surrounding regions. These patches are most likely to be artifacts. The middle region of the heart generally have lower SNR in raw OM fluorescent signals which increased noise in the activation time estimations. This activation time noise may not be readily observed in the activation map (*e.g.* for heart 1, Fig. 2.7B), but the conduction velocity calculation is a gradient estimation, and so it is very sensitive to noise and a small error in activation time could result in a large error in conduction velocity.

Relative conduction velocity can be estimated and compared qualitatively from the activation map. However, absolute conduction velocity values have rarely been reported for embryonic hearts. Kamino *et al.* measured conduction velocities for chick embryonic hearts at the stage of 7-9 somites (HH stage 9-10) using OM. From a series of photodiode readings and estimated 2D distances along the heart tube, conduction velocity was calculated to be 0.7~2 mm/s [80, 214, 216]. Argüello *et al.* reported conduction velocities for 45-47 hour (HH stage 13) chick embryonic heart using electrode recordings from very limited sites (2 points per region: ~7 mm/s at the AVJ and ~17 mm/s at the ventricle, averaged from 4 hearts) [215]. This study used similar stage embryos to those in the demonstration presented here, and their results were comparable to our averaged results (Fig. 2.8C). These previous measurements provide valuable comparisons. However, the technique that they used had low spatial resolution and did not take 3D distances into consideration. Conduction velocity increases significantly at HH stage 24-26, which was measured in 2D by Rothenberg *et al.* using optical mapping [217]. These results are not comparable to the work presented here because of the stage differences, but 3D topology was not taken into account in that study.

Conventional 2D conduction velocity calculations from OM can create artifacts and be misleading when comparing different regions of the same heart. For example, in heart 1, 2D calculations presented an apparent difference in conduction velocity between the inner and outer curvature of the AVJ while 3D corrected calculations correctly showed no significant difference (Fig. 2.9C and D). Both the inner and outer curvatures of the AVJ have relatively steep slopes (Fig. 2.8A, heart 1), however, the slope at the inner curvature is mostly parallel to the conduction direction while the slope at the outer curvature is mostly perpendicular to the conduction direction (Fig. 2.8A and B, heart 1). Therefore more correction was needed at the inner curvature than the outer curvature of the AVJ (Fig. 2.8C). Any uneven curvatures can cause such problems because their projections will result in non-uniform underestimations. Artifacts caused by non-uniform curvatures in conventional 2D conduction velocity calculations can be mitigated by 3D correction.

The instrument described here successfully demonstrated the conduction velocity correction method, but results could be further improved by additional technical development. The main source of conduction velocity noise is the OM recording. Compared to OM measurements of adult heart models, OM of early embryonic hearts suffers from low SNR because each pixel is integrating signals from a much smaller volume (*i.e.* fewer cells). Activation times determined from low-SNR AP traces are relatively noisy and in turn result in noisy calculated conduction velocity. Therefore, optimizing the imaging and post-processing steps for OM will improve the accuracy of calculating conduction velocity. Potential improvements include optimizing the imaging protocol to maximize the SNR of acquired OM data so that the activation time can be more accurately determined and developing gradient estimation methods more robust to low-

SNR signals. For example, instead of using two-point subtraction, a more advanced global or local fitting algorithm may be adopted to estimate the gradients [230]. Another limitation of the instrument described here is that because the heart is imaged by OCT from the opposite side as with OM, the size of hearts that may be accommodated are limited. This means that a limitation in the stage of heart that could be imaged to a maximum of about HH stage 21. This is because the penetration depth of OCT in tissue is limited to about 2mm. This limitation could be overcome by coupling both the OCT and OM light into the same objective lens, allowing OCT and OM imaging from the same side.

The method presented here will reduce experimental variability due to inconsistent heart morphology and orientation. This will enable improved comparisons of conduction velocity between hearts and easier identification of differences caused by diseases and defects. The ability to accurately measure conduction velocity can benefit the study of cardiac development in multiple ways. It may aid the study of ion channels and gap junctions at early stages of development. It may also benefit the study of other animal models. For example, compared to the avian heart, the looping-stage mouse heart exhibits more significant 3D curvature [231]. The Knockout Mouse Phenotyping Project (KOMP) has already found ~10% of transgenic mice have congenital heart defects [232]. It is likely that a large proportion of these defective hearts have conduction abnormalities. Yet these hearts have not been assayed for conduction defects. The methods described here could enable such electrophysiologic assays. Furthermore, the integrated OCT/OM system provides high resolution 3D structural images of the hearts simultaneous with conduction measurements. Important features inside the embryonic heart can be characterized and their influences on conduction velocity can be studied. For example, cardiac cushions, which

are valve progenitors, have been shown to modulate action potentials [233], some common genes and pathways can affect both conduction at the AVJ region and the formation of cardiac cushions [234-237]. The direct correlation between the morphology of the AV cushions and conduction velocity at the AVJ has never been available and may now be investigated with this newly developed integrated OCT/OM system.

In conclusion, we have presented a novel integrated OCT/OM system which can acquire structural and electrophysiological images simultaneously. We have also developed a 3D-corrected conduction velocity calculation method. This can correct conduction velocity underestimations and artifacts caused by 2D projection and provide more accurate measurements and more reliable comparisons for studies of normal and diseased models, thus improving our understanding of the electrophysiology of developing embryonic hearts.

## Chapter 3 4D OM with Light-sheet Microscopy

### 3.1 Introduction

During cardiac development, cardiac electrophysiology is important in coordinating heart beat as well as normal cardiac development [36, 37]. Abnormal conduction during heart development can lead to congenital heart defects (CHDs) in the adult cardiac conduction system itself, as well as in heart morphology and other functions. These CHDs include ventricular septal defects, conotruncal defects and related flow abnormalities [37, 219, 238]. Furthermore, electrical activity and structure of the heart starts to influence each other as early as cardiac looping stages [85]. Although the general conduction patterns at different heart development stages and conduction system development process were known for many years, the timing and etiology of conduction-related CHDs and the interplays among electrical activity, cardiac structure and other functions were still poorly understood. Technology that can better characterize and accurately quantify normal and abnormal early electrical activities is needed to improve our understandings on this topic.

Optical mapping (OM) is the main technology for investigating embryonic and adult cardiac electrophysiology [86, 220]. OM uses a fluorescence microscope and a fast camera to collect signals from either voltage-sensitive dye stained hearts or animal hearts with genetically encoded voltage-reporters [49, 110]. Motion of the hearts is usually fully suppressed with excitation-contraction (EC) uncouplers. OM acquires signals from the entire field of view simultaneously with high resolution without contacting the tissue. With acquired action potential traces, parameters such as activation time, action potential duration and conduction velocity can be calculated. With these advantages, OM has made

great contributions in the understanding of embryonic and adult electrophysiology [49, 220].

The ideal OM imaging should be able to achieve 3D, complete and orientation-independent mapping of conduction. Yet conventional OM is limited due to the fact that it collects signals from one side of the sample, with signals integrated from different depths and focusing planes, and projects to a 2D plane. Under this situation, information acquired from the sample is largely orientation dependent and incomplete, usually less than 50%. Several attempts have been made to solve or partially solve this problem in different animal models [35, 109, 110, 239]. In adult hearts or late-stage embryonic hearts, panoramic OM uses several cameras or splits the field of view of the camera to acquire several images around the heart was developed [35, 109]. However, it is very difficult to apply these methods to small and more complicated looped embryonic hearts. In looping stage quail embryonic hearts, our group has developed integrated OM and optical coherence tomography to correct conduction velocity calculation based on 3D heart geometry [239]. Yet this only improved the accuracy of conduction velocity calculations and did not provide any further electrophysiology information of the heart. In zebrafish heart with genetically encoded voltage reporter, 4D OM was acquired with a commercial spinning disk confocal microscope [110]. Complete 4D electrophysiology information was acquired in this study. However, avian or murine models, in which heart are four-chambered and the cardiac development is more similar to human, have much bigger hearts and genetic voltage reporters or not yet been used in these species. Voltage-sensitive dyes and motion suppression drugs are usually toxic and/or phototoxic [240, 241]. Phototoxicity and photobleaching of the dye potentially prevent long imaging sessions in 4D OM with

voltage-sensitive dyes and EC-uncouplers using confocal imaging, as reviewed in section 1.2.1.

Light-sheet microscopy is a 3D imaging modality that uses a cylindrical lens or a scanning beam to create a sheet of light to illuminate an entire plane at once and collect images at an orthogonal plane [242, 243]. Light-sheet microscopy features deeper penetration, high speed, low photobleaching, low phototoxicity and flexibility in determining resolution and field of view compare to other 3D fluorescence imaging modalities (*e.g.* confocal microscopy, two-photon microscopy). Therefore, it has been widely used in imaging a variety of samples [183, 190, 243, 244]. Due to its advantages of low phototoxicity, high-speed and large field of view, light-sheet microscopy is a suitable candidate for imaging 4D membrane potentials of embryonic hearts.

In this chapter we demonstrate a 4D OM technique achieved through light-sheet microscopy. 4D, complete, orientation dependent imaging of membrane potential and conduction of embryonic hearts was achieved. The custom light-sheet system optimized for 4D OM application will be depicted in detail. Experiment protocols of quail embryonic heart OM, data acquisition and post processing steps will also be described.

## **3.2 Materials and Methods**

### *3.2.1 Optical system*

The imaging system is a custom light-sheet microscope, in which the illumination path and the detection path are separated and orthogonal to each other. This section will step through each part of the optical system and the necessary alignment and optimization procedures. Fig. 3.1 presents a schematic diagram of the entire system.

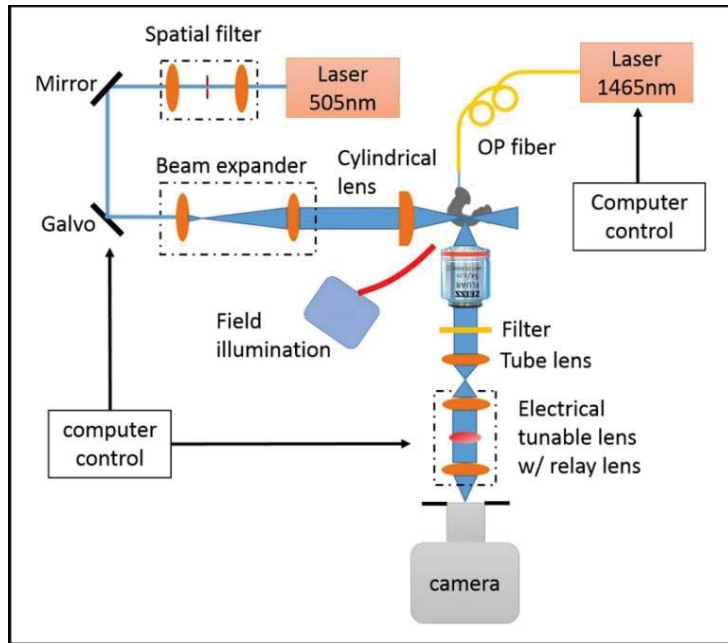


**Fig. 3.1** System setup diagram. Galvo: galvanometer mirror. OP: optical pacing

### 3.2.1.1 Illumination path

In the illumination path, a diode laser with 505 nm wavelength and 70 mW max power was used (Vortran Laser Technology Inc, Sacramento, CA). As shown in Fig. 3.1, the illumination path of our light-sheet imaging system is composed of a cleanup filter (Chroma Technology, Bellows Falls, VT), a set of relay lenses (LA1255-A, Thorlabs, Inc, Newton, NJ) with a 50  $\mu\text{m}$  pinhole (P50S, Thorlabs, Inc, Newton, NJ) in between as a spatial beam filter, reaches a galvanometer mirror (6210H, Cambridge technology, Bedford, MA) serve as the light sheet scanner along the detection axis, a beam expander (LA1951-A and LA1708-A, Thorlabs, Inc, Newton, NJ) and a cylindrical lens (LJ1695RM-A, Thorlabs, Inc, Newton, NJ) to form the light sheet.

The galvanometer mirror (galvo) is placed at a conjugate plane to the back aperture of the cylindrical lens. Accurate locating the galvo ensures light sheets at different scanning

angles are parallel to each other and the detection plane. The scanning voltage has a linear relationship with the location of the light sheet at the sample. This linearly relationship was validated through the illuminated locations on a sample as setting the galvo voltage to a series of values using a function generator (results shown in Fig. 3.2).

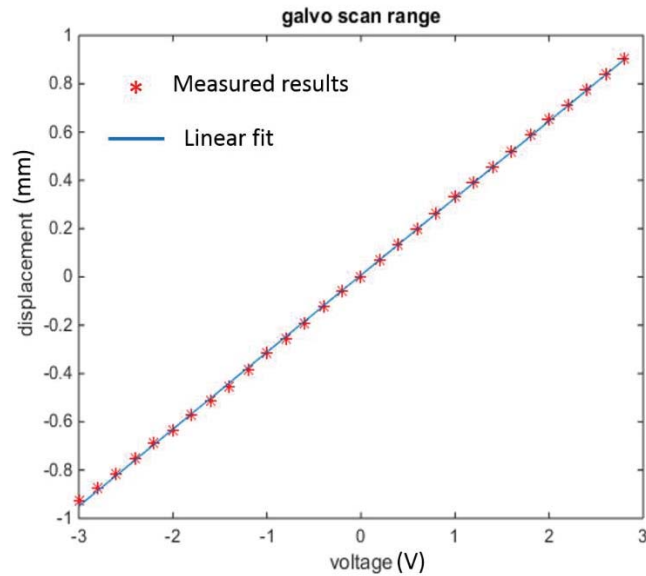


**Fig. 3.2** Displacement of the light-sheet location after the cylindrical lens is proportional to the voltage applied on the galvo.

The thickness of the light sheet is the axial resolution of the system. The light sheet created by this illumination setup has a Gaussian profile. The thickness at the focus has a theoretical value of  $\sim 2 \mu\text{m}$ . Experimental characterization of the light sheet thickness was carried out by acquiring sequential images while moving a phantom across the light sheet, as illustrated in Fig. 3.3. The phantom was made of clear polymer embedded with sparsely arranged fluorescence particles ( $0.5 \mu\text{m}$  diameter). The thickness of the light sheet was measured to be  $3 \mu\text{m}$  at around the focus.

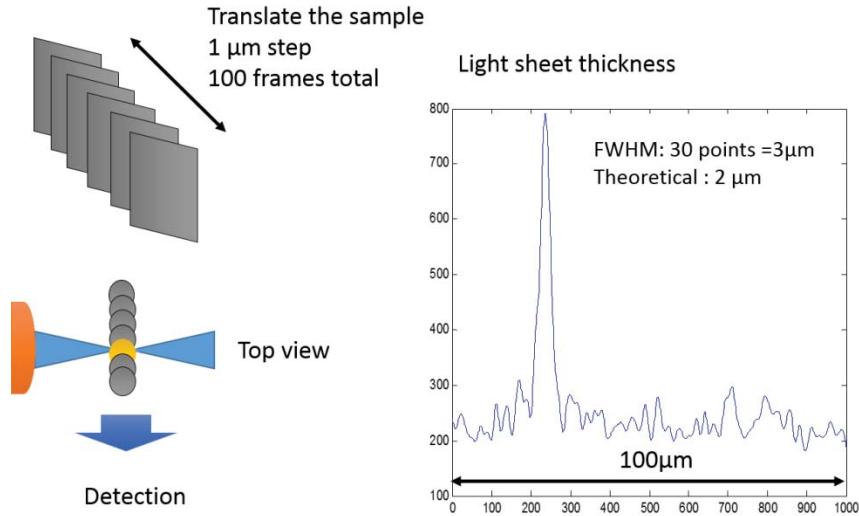


**Fig. 3.3** The left panel presents the method for calibrating the axial resolution of the light-sheet system. The phantom was moved across the light sheet with 1  $\mu\text{m}$  steps. A particle can only be light up when it is in the light-sheet illumination profile. The right panel shows the result of a calibration measurement. The total travel range of 100  $\mu\text{m}$  was interpolated from 100 to 1000 points.

### 3.2.1.2 Detection path – Objective, tube lens and camera

The detection path of the light-sheet imaging system consists of an objective (Fluar 5x/0.25 or C-Apochromat 10X 0.45NA, ZEISS, Oberkochen, Germany), an emission filter (535 nm  $\pm$  20 nm, Chroma Technology, Bellows Falls, VT), a tube lens, a set of relay lenses (LA1509-A, Thorlabs, Inc, Newton, NJ) with an electrically tunable lens (ETL, EL-10-30-C-VIS-LD, Optotune Switzerland AG, Dietikon, Switzerland) in between and an EMCCD camera (iXon Ultra 897, Andor Technology, Belfast, UK). EMCCD camera acquires images in  $xy$ -plane.

Without the ETL, the detection path is a regular microscope, consists of an objective, a tube lens and a camera. The focal length of the objective and that of the tube lens determines the actual magnification of the microscope. The focal length of the tube lens is usually a set value. Several companies such as Nikon and Leica uses 200 mm standard tube

lenses while Zeiss uses 165 mm tube lenses. The magnification number labelled on the objectives themselves is accurate only when using the corresponding tube lenses. If a different magnification is desired in a specific system, it can be achieved by changing the tube lens. The resolution of the system is determined by the NA of the objective and the matched pixel size of the camera. The objective NA limits the resolution to  $R = 0.61\lambda/NA$ , which represents the smallest distance between two scatters that the system can resolve. To achieve this resolution, the magnification of the whole system and parameters of the camera need to match this resolution. This means that each resolvable unit need to occupy at least two pixels on the camera. For example, for an objective with the specification of 10X, 0.45NA, with 550 nm emission light, the theoretically achievable resolution is 746 nm. Magnifying this by 10 times it projects to 7.46  $\mu\text{m}$ . Therefore the camera needs to have the pixel size smaller than 3.73  $\mu\text{m}$  in order to match this resolution. Alternatively further magnification needs to be implemented in the path. In our application, the field of view, performance at low light situation and speed are higher priorities than reaching the optimal resolution. Therefore we selected an EMCCD camera based on these properties, not on the purpose of trying to match the resolution. We chose two tube lenses to extend FOV options. The actual magnification, effective pixel size and FOV are summarized in Table 3.1. Day 2 and day 3 yellow fluorescence protein (YFP) quail embryonic hearts were imaged with the 5X 0.25 NA objective lens and 200 mm tube lens for the observation of endothelial-to-mesenchymal transition (EMT, results shown in Fig. 3.4).

For OM experiments, we adopted the setting of 5X 0.25 NA objective with 75 mm tube lens. In order to run at the speed of hundreds of frames per second, the camera needs to be operated at a crop mode, in which some pixels are completely, physically blocked by a mask (Optomask, Andor, Technology, Belfast, UK). To achieve satisfactory speed and FOV,  $128 \times 128$  pixels remain unblocked for imaging.

**Table 3.1** Resolution and FOV with different optical settings

objective\ f (tube lens)	theoretical resolution	200 mm ( $512 \times 512$ )			75 mm ( $128 \times 128$ , crop mode)		
		Actual M	pixel size	FOV	Actual M	pixel size	FOV
Zeiss water 10X 0.45 NA	685 $\mu\text{m}$	12.12X	1.33 $\mu\text{m}$	681 $\mu\text{m}$	4.55X	3.52 $\mu\text{m}$	451 $\mu\text{m}$
Zeiss air 5X 0.25 NA	1232 $\mu\text{m}$	6.06X	2.64 $\mu\text{m}$	1352 $\mu\text{m}$	2.27X	7.04 $\mu\text{m}$	901 $\mu\text{m}$

### 3.2.1.3 Detection path – ETL

Unlike most of traditional light-sheet systems, the sample and the objective do not need to move in order to acquire multiple  $z$ -planes, instead, the ETL's focal power is continuously altered to scan the focusing plane in correspondence with the position of the illuminated light sheet. The optical implementation is similar to a previous design [200]. The ETL is a liquid lens. It is basically a container filled with optical fluid and sealed with an elastic polymer membrane. An electromagnetic actuator is used to exert pressure, which determines the deflection of the lens thus the focal power. The focal power of the ETL is proportional to the current applied on the electromagnetic actuator. Because of its liquid property, the ETL needs to be mounted horizontally. The optical path layout is shown in Fig. 3.5. The ETL set was pre-mounted with an offset lens that has focal length of -150 mm. The focal length of the pair is referred as  $f_{ETL}$ . As the focal power ( $1/f_{ETL}$ ) changes,

the focus displacement at the objective is given by  $\delta_z = -\frac{1}{M^2} \frac{f_r^2}{f_{ETL}}$ , where  $f_r$  is the focal length of the relay lens [200]. Theoretical and experimental measurements are shown in Fig. 3.6.

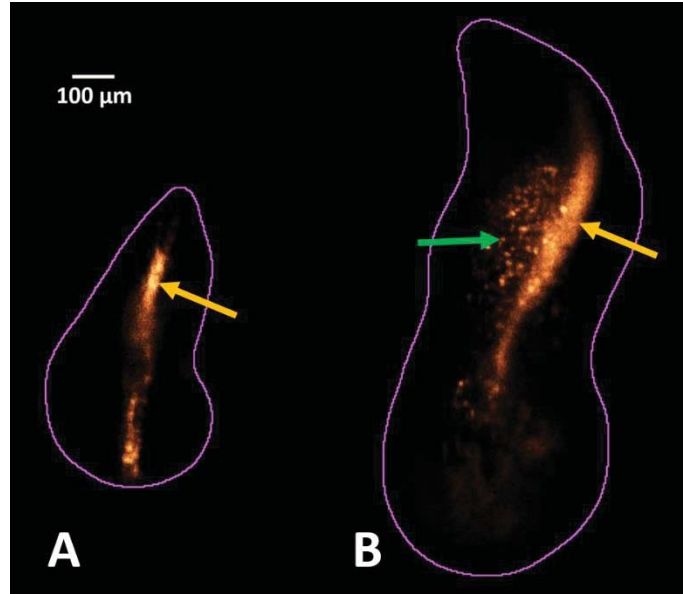


**Fig. 3.4** Fluorescent images of HH stage 14 (A) and 19 (B) YFP quail embryonic hearts acquired using a light-sheet microscope (5X 0.25 NA, 200 mm tube lens). Magenta borders: segmented heart tube. Yellow arrows: endocardium; green arrow: EMT cells.

It is critical to precisely align the ETL in the detection path. If not, two problems occur. As  $1/f_{ETL}$  changes, the magnification of the system is not consistent, or the images shift laterally. The first issue is caused by misalignment of distances between lenses while the second problem is due to ETL not being centered. The correct distances and alignment steps are labelled on Fig. 3.5. To ensure the center location of ETL, it should be mounted on a  $xy$ -translational mounting piece. Both the magnification and the lateral shift corrections require iterative procedures. The metric for determining similarities between images acquired at different locations was parameters returned from a rigid image registration algorithm (here rigid parameters are magnification and translation). As can be

seen in Fig. 3.7, the registration results were reliable. Examples of magnification and shift corrections are shown in Fig. 3.8.

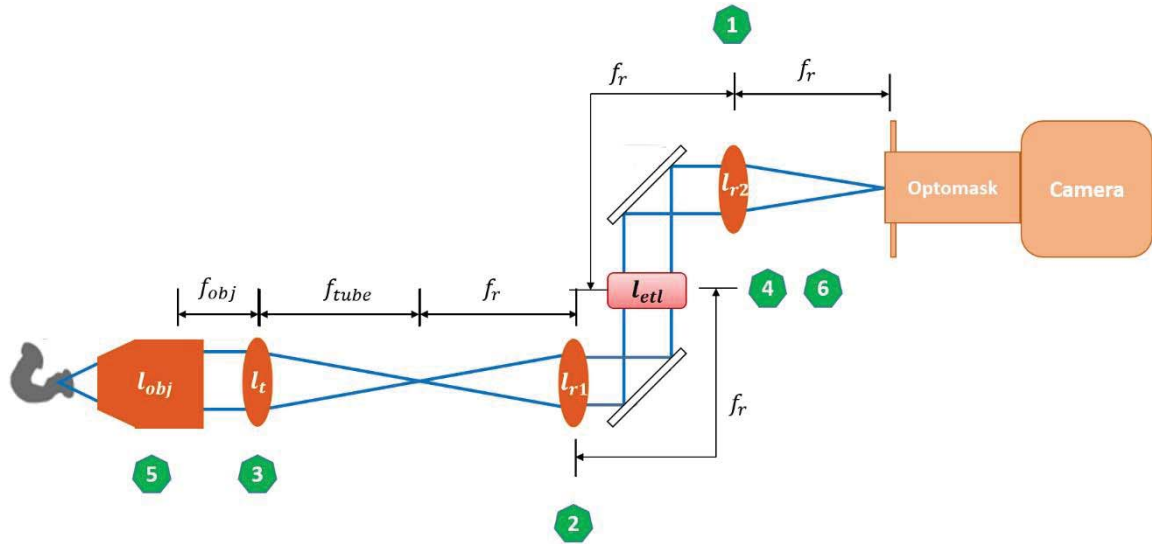


**Fig. 3.5** The exact layout of the detection path of the light-sheet system. Because the ETL needs to be mounted horizontally, two mirrors cubes were used to reflect the optical path. Distances labelled between optical components indicate the length of light path at the optical axis. The numbers in green heptagons represent the order of alignment steps. The ETL should be adjusted multiple times to ensure it is centered between  $l_{r1}$  and  $l_{r2}$  and it is laterally centered with respect to the optical axis. The lateral adjustments corrects for the lateral shifts in images as  $1/f_{ETL}$  changes. The alignment step 5 ensures uniform magnification as  $1/f_{ETL}$  changes.

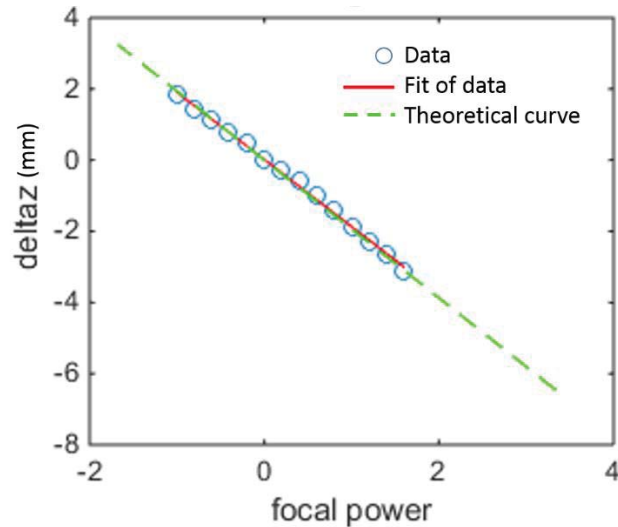


**Fig. 3.6** The linear relationship between the focal power of the ETL and the displacement of image plane.

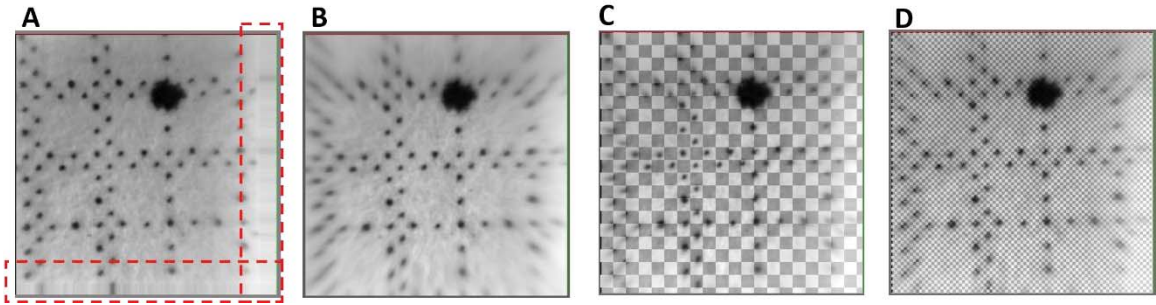


**Fig. 3.7** Rigid image registration as a metric for optimizing ETL locations. A and B are images acquired under different settings of ETL focal power. A was registered to B. The lateral shifts in both directions can be observed in the dashed-line red boxes. C and D are merging results of A and B displayed using checkerboards. There is no obvious misalignment in the merging results.

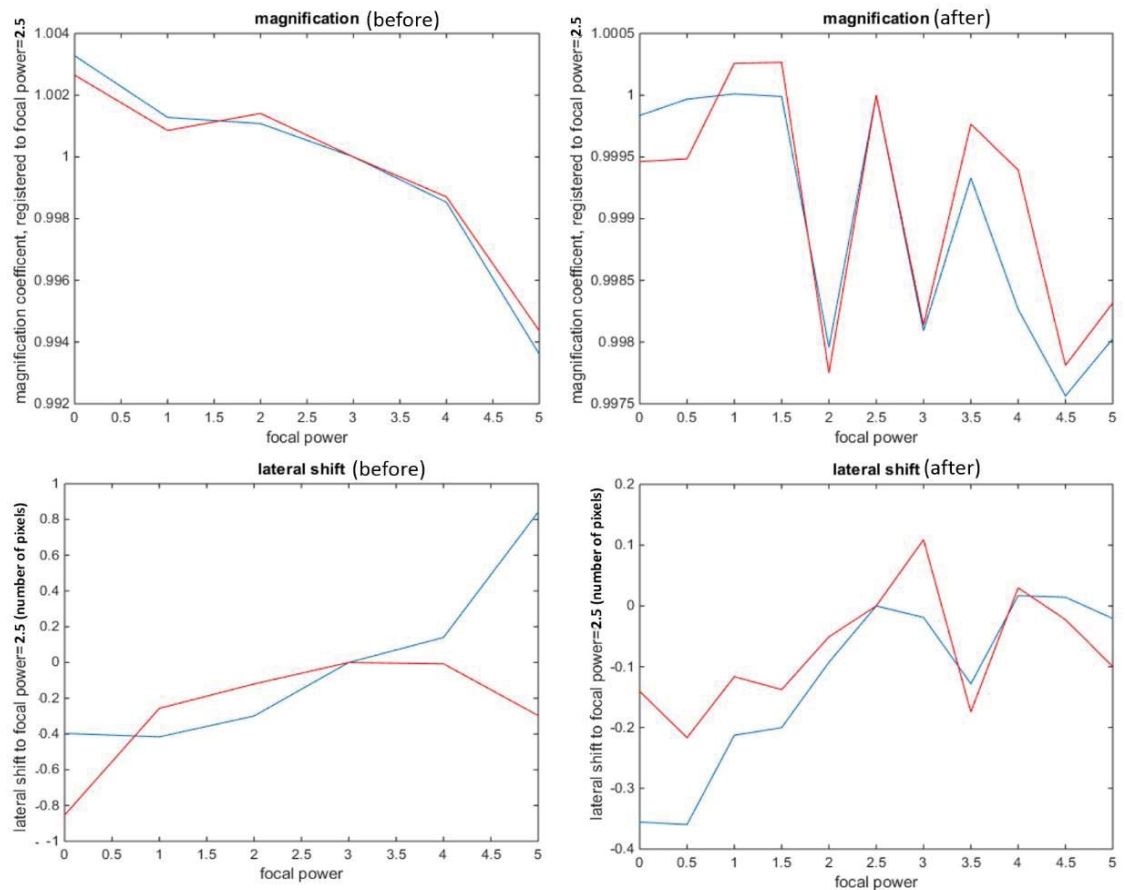


**Fig. 3.8** ETL optimization examples. Top panels are before and after an adjustment for correcting magnification. Bottom panels are before and after corrections of lateral shifts of the ETL. Images acquired at different focal power settings were registered to the image at focal power=2.5. Both parameters were reduced after adjustments.

### 3.2.1.4 Optical pacing implementation

Cardiac electrophysiology parameters are heart rate dependent [111, 112]. OM in adult hearts uses electrodes as a point stimulation source [113]. In embryonic hearts it is not feasible to stimulate using electrodes. Optically pacing the hearts was developed as a reliable stimulation method and it was demonstrated with OM [118, 119].

The optical pacing setup includes a single-mode fiber-coupled 1465 nm diode laser (QPhotonics, Ann Arbor, MI) and a laser diode controller (Newport Corporation, Irvine, CA) [119]. 1Hz, 20 ms pulse width, 2.2 V square-wave pulse trains were used to pace both examples in this paper. The resulted radiant exposure on the sample was 58 J/mm<sup>2</sup>. Optical pacing signals were controlled through a Labview program. Fig. 3.9 shows the pacing fiber placement and an OM recording of a paced embryonic heart.

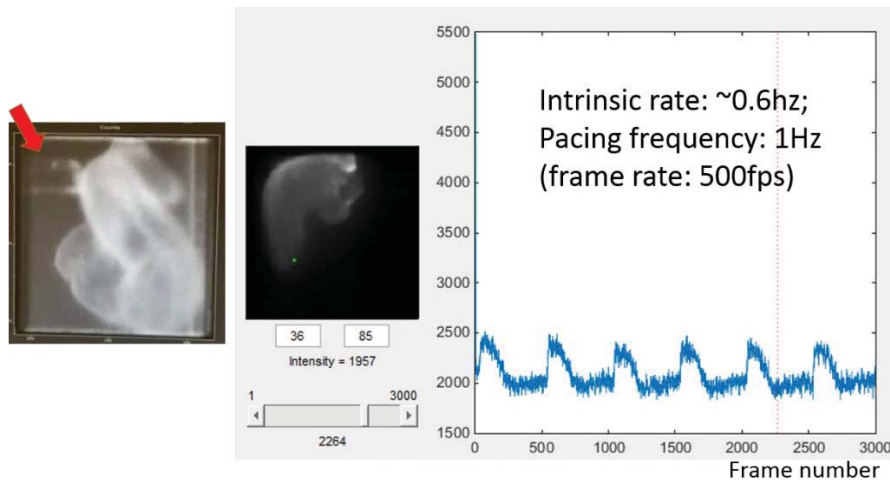


**Fig. 3.9** OM recordings with optically paced heart. The left panel shows a brightfield image of the pacing fiber (pointed by the red arrow) placed on an embryonic heart. The middle panel shows the fluorescence image of another heart. The right panel shows the traces from the selected pixel in the middle panel, labelled with a green dot on the left panel. The intrinsic rate of the heart was approximately 36 beats per minute, and it was paced at 1 Hz. The recording shows a 6 s time period (3000 frames) and the action potentials shows exact 1 Hz.

### *3.2.2 Sample preparation for OM experiments*

Fertilized quail eggs (*Coturnix coturnix*, Boyd's Bird Company, Inc., Pullman, WA) were incubated in a humidified, forced draft incubator (G.Q.F. Manufacturing Co., Savannah, GA) at 38°C for 50 hours. Quail embryos were dissected from the yolk. The stage of each embryo was determined by the number of somites under a stereomicroscope and the heart was then excised [47].

FluoVolt was the voltage-sensitive dye used in this experiment. The mechanism of this dye is different than di-4-ANEPPS. It is similar to the photo-induced electron transfer mechanism described in Chapter 1 (personal communications with the company). Voltage-sensitive dye solution was prepared before each experiment by mixing FluoVolt (Life Technologies, Carlsbad, CA) and PowerLoad concentrate (Life Technologies, Carlsbad, CA) into Tyrode's (Sigma-Aldrich, St. Louis, MO) solution in manufacture suggested concentrations. The excised embryonic heart was stained in 300  $\mu$ l dye solution for 20 minutes at room temperature. The embryonic heart was then moved to a 1 ml cuvette filled with 1 ml of Tyrode's solution containing 10  $\mu$ M of excitation-contraction (EC)-uncoupler, cytochalasin D (Sigma-Aldrich, St. Louis, MO) to eliminate myocardial contraction. The cuvette was mounted onto the sample stage of the imaging system. Two Hamburger–Hamilton (HH) stage 14 quail embryonic hearts were selected for study.

### *3.2.3 4D data acquisition and image processing*

During the imaging session, an embryonic heart was placed at the imaging field of view. With field illumination and under guidance of the camera, the end of the optical pacing fiber was directed into the cuvette and gently placed in contact with the surface of the heart.

Emission filter was then placed in the detection path. While optically pacing the heart, the camera continues to acquire images at 500 frames per second and the  $z$ -plane was moved every two seconds by simultaneously scanning the light sheet through the galvanometer mirror and adjusting ETL focal power. For each embryonic heart, 15 – 20  $z$ -planes were imaged.

2D time-sequence images were rearranged to construct a 4D dataset based on known time differences between adjacent  $z$ -planes. The 4D dataset was trimmed to keep one full action potential across the whole heart. Our previously developed two accumulative fitting software package (Matlab, Mathworks, Natick, MA) and image filters (Matlab, Mathworks, Natick, MA) were applied to the 4D data set. 4D transmembrane potential movies were created with the fitted results using Amira (FEI Company, Hillsboro, OR). Transmembrane potentials on  $xz$ -plane and  $yz$ -plane were also sampled and displayed in Amira. Activation time of each action potential was determined through the fitting software package and the results were mapped onto a segmented 3D surface mesh of the heart structure.

For validation purposes, 3D activation time values for each heart were projected to 2D using weighted averaging based on an exponential profile from the surface of an arbitrarily chosen side. The projected results were shown as conventional isochrones maps.

### **3.3 Results of 4D OM**

A fluorescence image of a single  $z$ -plane and three fluorescence traces from selected pixels in this  $z$ -plane are shown in Fig. 3.10. The myocardium of the heart mostly showed strong staining, with the bottom part generally stronger than the top part due to the light sheet direction. In this particular example, the bottom side is near the inflow region of the heart and the top side is close to the outflow tract. A delay of activation can be clearly observed

in Fig. 3.10B and Fig. 3.10C. The endocardium of the heart also showed some staining, yet there was no voltage signal, as expected.

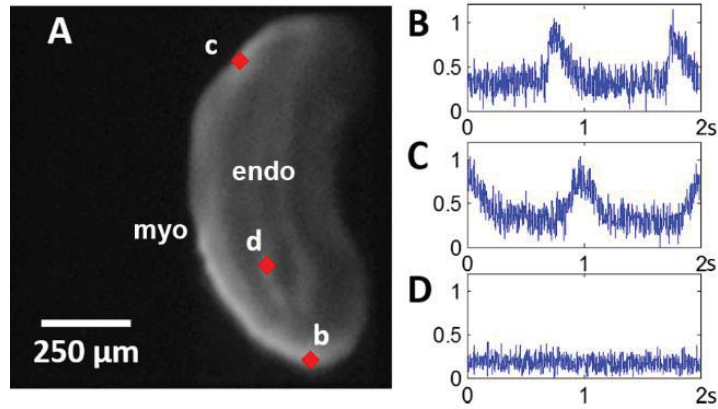


**Fig. 3.10** Panel A is a fluorescence image of an embryonic heart with voltage-sensitive dye staining. b, c and d are pixels which traces are plotted in B, C and D respectively. Intensity values were normalized. myo: myocardium; endo: endocardium.

With 4D datasets, the view of slices is not limited to the imaging plane. Transmembrane potentials of three orthogonal planes from a 4D dataset are shown in Fig. 3.11 and movie 2.1. The imaging plane ( $xy$ -plane), showed activation from the bottom of the image to the top, with two sides activated at similar times (Fig. 3 B, F, J, N). The  $xz$ -plane is orthogonal to the conduction direction therefore the activation around the heart tube was almost simultaneous. The  $yz$ -plane provides a view for the inner and outer curvature of ventricular region of the heart tube. As observed in Fig. 3.11 D, H, L, and P, conduction at the outer curvature is much faster than the inner curvature to ensure the tube has coordinated conduction at the outflow tract. 4D transmembrane potentials of another sample are also shown in movie 2.2.

Two examples of 3D activation map are shown in Fig. 3.12 and movie 2.3. In heart 1, the end of the inflow and outflow regions were not captured. In heart 2, the region affected

by pacing artifact was removed to avoid confusion. As expected the region immediately adjacent to and downstream of the pacing region was activated first and the end of outflow tract was activated last. The whole process in both embryos took approximately 300 ms. 2D projected activation maps are shown in Fig. 3.13.

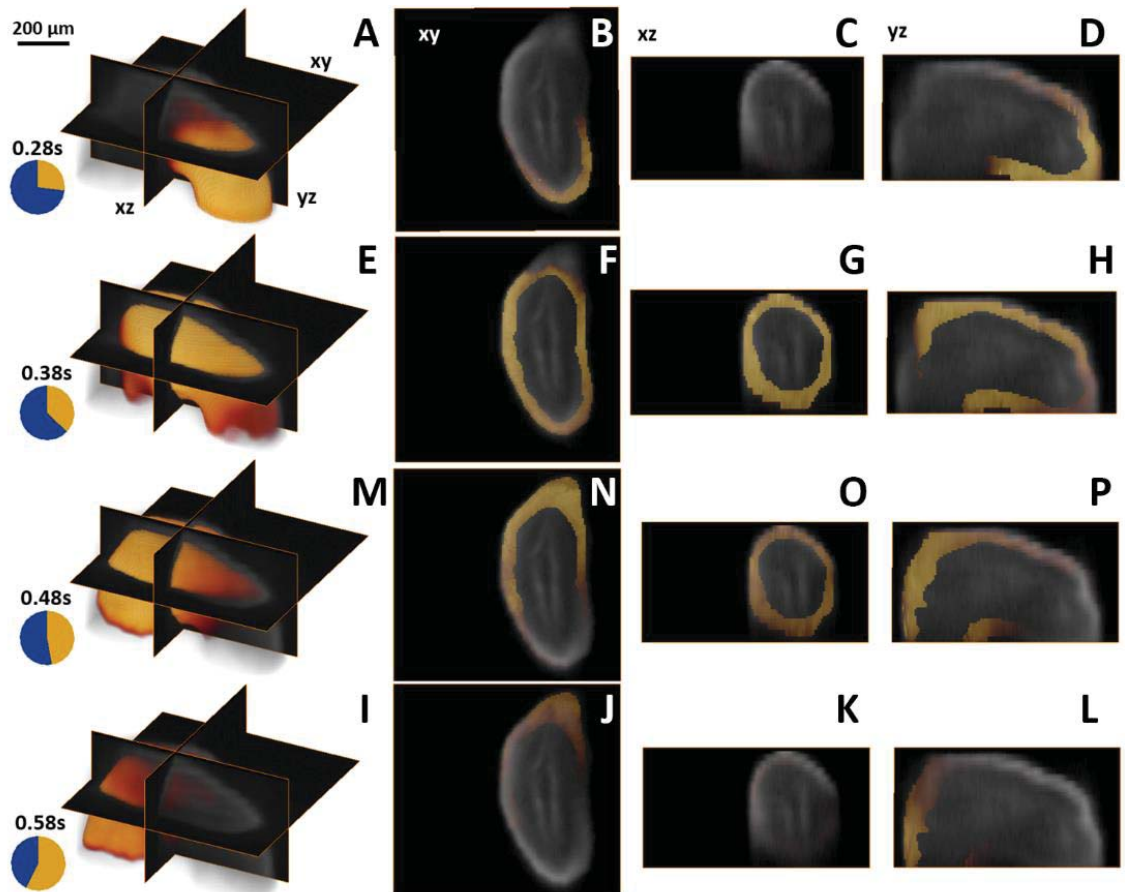


**Fig. 3. 11** 4D transmembrane potentials shown in 3D and three orthogonal planes. Colored activation wave is overlaid on grayscale heart tube volume reconstruction or cross sectional images. A, E, I, M are 3D transmembrane potential volumes at 0.28s, 0.38s, 0.48s and 0.58s respectively and the locations of the three orthogonal planes are indicated these panels. B, F, J and N are  $xy$ -planes at corresponding time points. C, G, K and O are  $xz$ -plane at corresponding time points. D, H, L and P are  $yz$ -planes at corresponding time points.

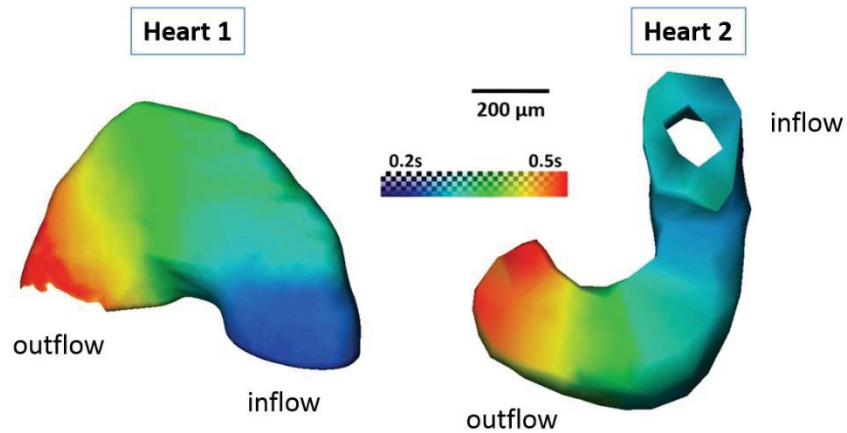


**Fig. 3.12** 3D activation map of two HH stage 14 embryonic hearts.

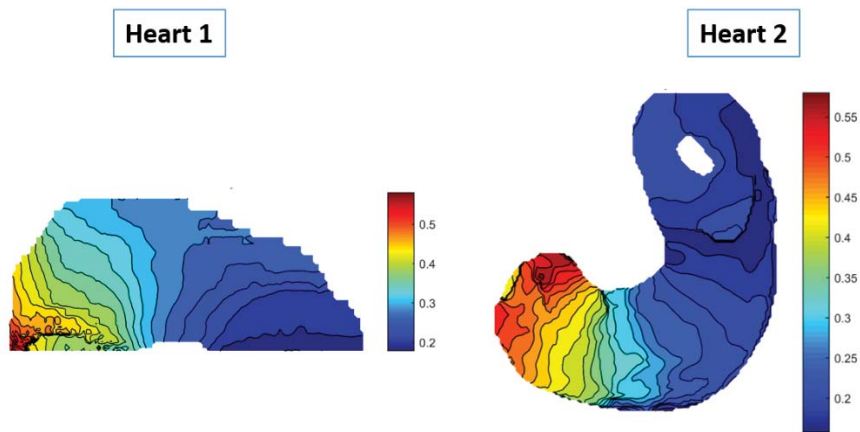


**Fig. 3.13** Projected 2D activation maps from two HH stage 14 embryonic hearts

### 3.4 Discussion

We have demonstrated the first 4D voltage-sensitive dye imaging in avian embryonic hearts with light-sheet microscopy and optical pacing. This provides complete, orientation independent electrophysiology information around the entire heart tube with a controlled heart rate. Unidirectional conduction with a slow-fast-slow feature was demonstrated in complete looping heart tubes. By providing complete information from one sample, it

greatly reduces the number of samples needed to be imaged in order to acquire certain regions of interest. The orientation independent feature enables more direct and accurate comparisons among individual animals. 4D transmembrane potential movies, transmembrane potentials in resampled orthogonal planes, the 3D activation maps, and the 2D projected activation isochrone maps showed that the electrophysiological signals we acquired here not only showed consistent conduction patterns with previously reported results in avian hearts at similar stages [81-83], In addition, we further provided complete conduction information of the 3D looping heart tubes.

In building the 4D imaging system, two factors are especially critical. They are achieving acceptable SNR and speed. Voltage-sensitive dye imaging in embryonic hearts usually suffers from low SNR due to the small signal change with conventional dyes such as di-4-ANEPPS [90]. The use of 3D sectioning method further eliminated the integration of signals from different depth and different focusing planes. While this spatially resolves the source of signals and improves the accuracy of transmembrane potential recordings, the SNR would be largely reduced. The newly available voltage-sensitive dye, FluoVolt, provides more than 5 times better SNR than di-4-ANEPPS under conventional OM setup, as shown in Fig. 3.14. Here under the light-sheet imaging conditions, it offered acceptable SNR (as shown in Fig. 3.10), which was in the analyzable range of our previously developed fitting software package [90]. Why do we care about speed? Voltage-sensitive dyes and EC-uncouplers are toxic or phototoxic [64, 241]. 4D OM imaging not only requires a high-speed camera for providing enough temporal resolution for the fast transmembrane potentials, time of each imaging session should also be minimized while optimally maintaining the heart's health. Therefore we selected light-sheet microscopy as

our 3D sectioning method because it can achieve high frame rates by acquiring signals from an entire plane simultaneously and its low phototoxicity by illuminating only the imaging plane. We adopted the electrical tunable lens (ETL) design in the detection path so that no translation was induced on the sample and the transition time between  $z$ -planes is negligible. Optical pacing not only serves as a means for heart rate control, but also provides very accurate heart cycles to greatly reduce the amount of heartbeats needed at each  $z$ -plane.

Embryonic hearts were kept under room temperature in this demonstration. Further development of a temperature-controlled imaging chamber would maintain the viability of the hearts and extend the imaging session.

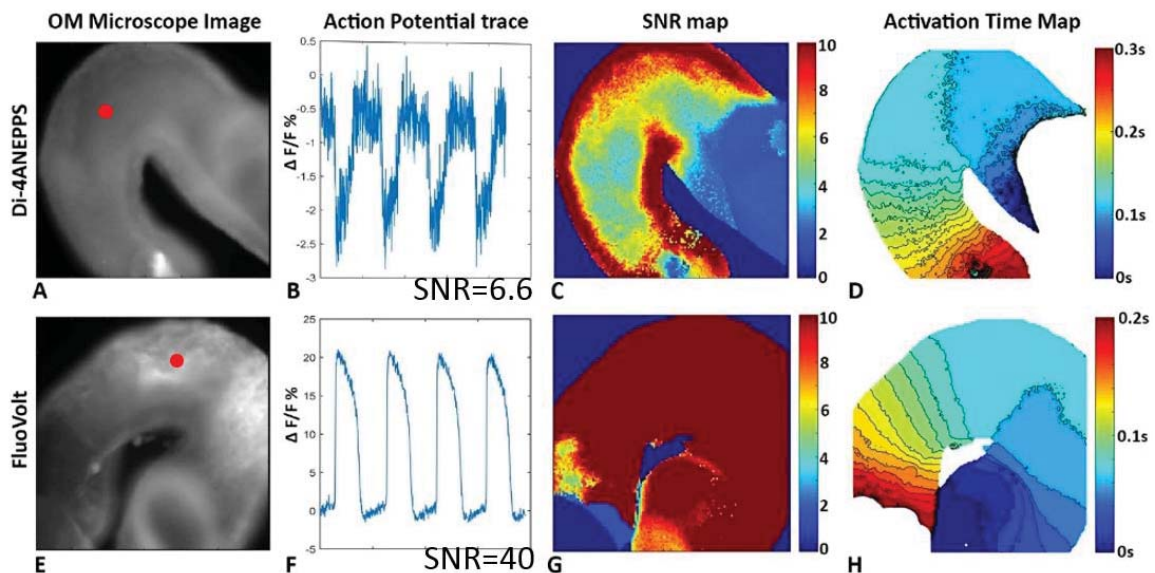


**Fig. 3.14** Comparison of SNR between di-4-ANEPPS and FluoVolt. A and E are fluorescence images from two embryos that were stained with each dye. B and F are two representative action potential traces from each example. C and G are SNR maps of the entire hearts. D and H are isochrone maps calculated from each example without any filtering. Reproduced from the same original data as Figure 4 in Watanabe *et al.*, 2016 [48].

4D OM with light-sheet microscopy developed in this study moved a significant step further from conventional OM. . It is able to provide full characterization and phenotyping of early embryonic cardiac electrophysiology. It will also be a reliable tool for comparing normal and abnormal cardiac conduction in developmental models because it is orientation independent. In addition, this method can be easily adapted to other animal models and has the potential to achieve *in vivo* conduction mapping for animal models in which genetically encoded voltage indicators are available. Early cardiac electrophysiology was shown to have interplays with critical early cardiac structures [85]. 4D transmembrane potentials could potentially be more accurately related to 3D cardiac structures and answer key questions on the interplay among cardiac structure, gene expression and electrophysiological functions.

## **Chapter 4. Heart motion correction in OM using image registration**

### **4.1 Heart motion in OM**

Cardiac electrical activity and conduction sequence can be recorded optically with OM [49, 220]. The contracting motion of the heart changes the location of signal sources during imaging, making action potential traces ambiguous, therefore motion suppression or correction is necessary. A widely-accepted method for eliminating motion artifacts in OM is to use an excitation-contraction (EC) uncoupler to fully stop heart motion without affecting electrical activity of the heart. Several popular EC-uncouplers are Cytochalasin D (cytoD), blebbistatin and BDM [93, 94]. Other methods such as mechanical suppression, ratiometric imaging and image registration have been used to reduce or correction heart motion in OM recordings, yet they have not reached a satisfactory level [99-101].

Although EC-uncouplers perform perfectly as a mechanism for abolishing heart motion completely, they may induce pharmacological effects that influence calcium handling, ion channel kinetics and affect action potential characteristics [96, 97]. Baker et al. found that diacetyl monoxime (DAM) and cytoD altered intracellular calcium concentration handling and the vulnerability to arrhythmias of perfused mouse hearts. Action potential duration (APD) was increased by approximately 100% and conduction velocity was reduced by 10~20% [245]. A different group demonstrated similar but not as pronounced effects of cytoD and BDM in rabbit hearts [96]. Blebbistatin was also shown to prolong APD by 25%, increase the maximal slope of restitution by 100% and ventricular fibrillation threshold significantly in rabbit hearts [97]. Furthermore, in embryonic hearts, EC-uncouplers can severely affect the health of the heart and significantly shorten tissue viability. This not only affects the amount of data that can be acquired with one sample,

but is also incompatible with longitudinal imaging over several stages, which is especially important for investigation of the developing conduction system. Other methods of suppressing or correcting heart contraction are still being pursued.

This chapter will describe the approach of using nonrigid image registration as a motion correction mechanism to recover signals acquired from the freely beating intact quail embryonic heart.

## **4.2 Image registration**

Image registration is aligning one set of images to another set of images that share the same object or content. The entire calculation is based on the information in the images. These images may be acquired through 2D or 3D imaging methods, including common medical imaging modalities such as fluorescence microscopy, computed tomography and magnetic resonance imaging. In medical imaging, multimodal datasets are often acquired for accessing different types of information. Image registration is necessary in order to associate these different pieces of information. This section will provide a brief review on image registration.

There are many ways to categorize the numerous registration methods [246]. This section will be classifying registration methods based on geometrical transformation, rigid, affine and deformable transformation. Affine and deformable transformation together can be called nonrigid registration. Usually, one 2D or 3D image is defined as the reference image and the other one is defined as the moving image. The registration from the moving image to the reference image is an iterative optimization process based on some form of similarity metric. The stopping criterion is reaching the minimum of a cost function.

Rigid image registration is the simplest type of registration and requires the least number of parameters. A 2D case only involves three parameters: two translational parameters and a rotational parameter. This transformation preserves all distances within the object, the straightness of lines, and relative angles between lines. Affine registration moves one step further with the addition of scaling and shear parameters. Therefore it does not preserve distances or angles between lines, but it still preserves the straightness of lines. Both rigid and affine transformation have limited number of parameters, therefore they can be performed using matrix-based registration methods [246].

Deformable transformation is also called free form transformation. In a lot of situations, especially in biomedical imaging with live samples, local deformation due to the displacement or the morphological change of the sample can be quite common. Here the object in one image needs to be deformed in order to match the other image. Therefore even the straightness of lines cannot be preserved in free form transformation. An example from this category B-spline based nonrigid registration method [227]. In this method, control points with equal spacing are assigned to the entire image/volume. The spacing can be user-defined. Transformation of each pixel is determined by the transformation of its surrounding control points using B-spline interpolation. The number of control points associated with the pixel can also be adjusted. Therefore these parameters can be tuned to suit for different situations base on properties of the images or the degree of local transformation needed. The judging criterion is similarity between the two images/volumes. Two often used similarity equations are cross correlation and mutual information. To achieve the optimal transformation, a cost function associated with the transformation

parameters is iteratively minimized [227]. Because biological tissues should have smooth borders, a smooth penalty term is also introduced to the cost function.

## **4.3 Methods**

### *4.3.1 Sample preparation*

Fertilized quail eggs (*Coturnix coturnix*, Boyd's Bird Company, Inc., Pullman, WA) were incubated in a humidified, forced draft incubator (G.Q.F. Manufacturing Co., Savannah, GA) at 38°C for approximately 50 hours. An HH stage 15 quail embryo was removed from its egg and the heart was excised. The embryonic heart was stained with 10 $\mu$ M of di-4-ANEPPS (Life Technologies, Carlsbad, CA) in 300  $\mu$ L Tyrode's solution (Sigma-Aldrich, St. Louis, MO) for 12 minutes at room temperature. The embryonic heart was then placed in the imaging chamber filled with 1 mL of Tyrode's solution.

### *4.3.2 Image acquisition*

The OM imaging system was described in chapter 1. This experiment was conducted at room temperature. While the embryonic heart was beating, an OM image series was acquired. 10  $\mu$ M cytochalasin D (Sigma-Aldrich) was then applied to the surrounding solution to suppress contraction of the heart. After the heart motion was completely stopped, another OM image set was collected.

### *4.3.3 Registration methods of time-series images*

An open source registration software package based on the described B-spline registration method was used in this study [227]. Parameters that can be user-optimized includes transformation level (rigid, affine or nonrigid), similarity metric, spacing of control points (intersecting points of a mesh grid), and smooth penalty level. Between each image pair,

the registration return a matrix contains  $x$  and  $y$  transformation matrices, with which the exact transformation can be replicated.

Each OM dataset contains 600 time-series images. It was necessary to determine how to register all 600 images to a single reference image and ideally “freeze” the heart motion. Four methods were tested in this study, as shown in Fig. 4.1. During each heartbeat, the heart starts at a resting phase, contracts until reaches a most contracted phase, and then return to the relaxing phase. The first method was call serial neighbor, in which each frame was registered to its neighboring frame and the transformation matrix was recorded. Then the  $n^{\text{th}}$  frame was transformed  $(n-1)$  times to the first frame. The idea behind this method was that a larger transformation was more challenging therefore transforming in small steps may be more reliable. However, it was discovered later that because each transformation is not ideal, many times of transformation cause too much accumulated error and cannot effectively correct the motion. The second and the third methods were simply registering every frame to a single reference frame, which was a frame at the resting phase or a frame at a middle contracting phase. A concern with this method was that frames that were further away from the reference may not have as good registration results as the frames closer to the reference. The last method is the key-frame method, which combines the advantages the first three methods and avoids the disadvantages. It separates the entire dataset to smaller groups. Frames in each group (*e.g.* in this study 20 frames per groups) were registered to the first frame as a mid-step reference (so-called key-frames). These key-frames from the smaller groups were registered to a single reference and the transformation matrices were recorded. All frames that were already registered to their key-frames were

then transformed again using the corresponding key-frame transformation matrices. In this method, each frame was at most transformed twice.

After each registration process, results were fed into the processing software package. Activation maps were  $2 \times 2$  binned to reduce noises. Conduction velocities were calculated for the ventricle and the outflow tract regions by selecting paths along the heart tube and use the activation difference divided by the distance of each path. Each measurement was repeated 10 time.

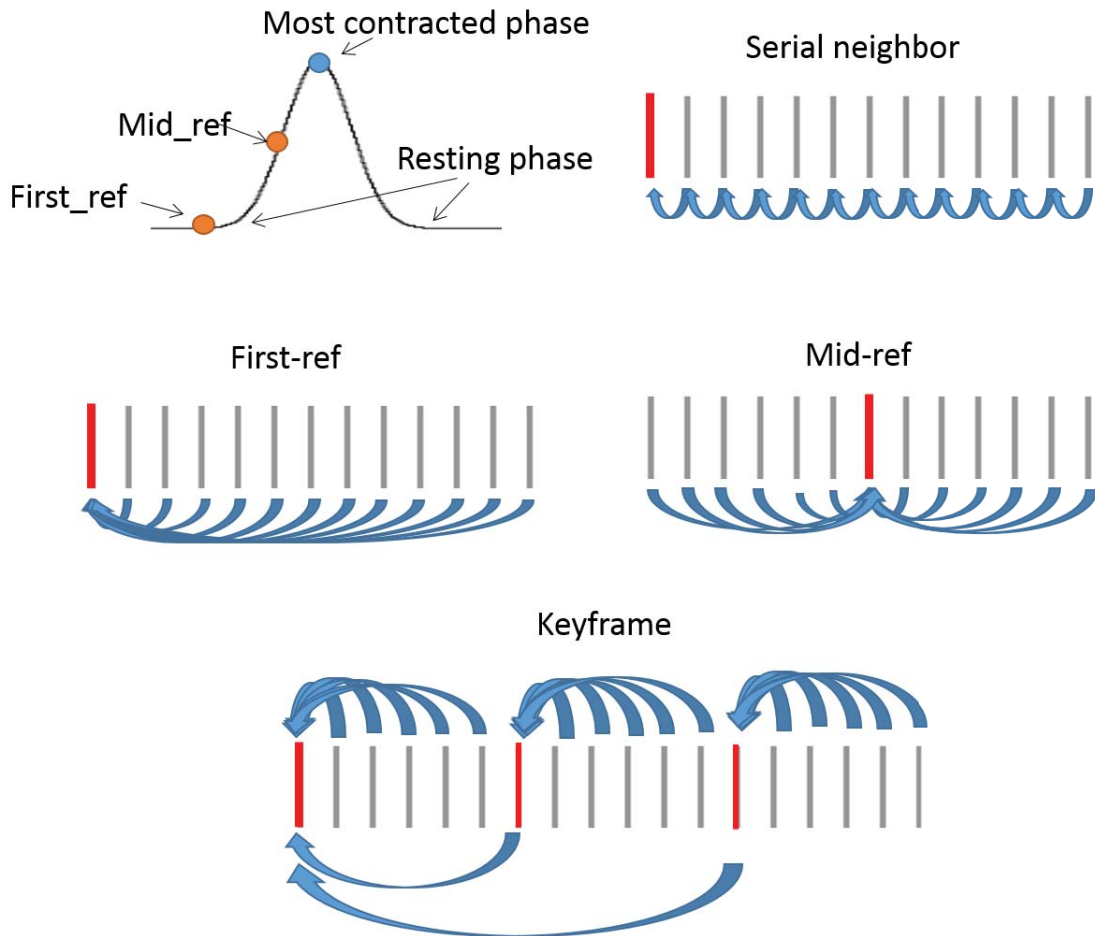


**Fig. 4.1** Schematic diagram of multiple-image registration methods.

#### 4.4 Results and discussion

Image registration methods can effectively correct motion in OM recordings, as shown in Movie 4.1. An example of registered frame and the deformed grid is shown in Fig. 4.2.

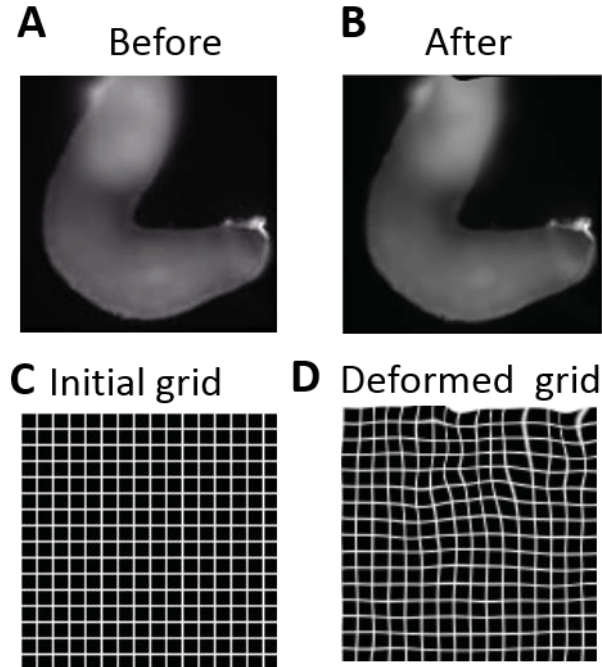


**Fig. 4.2** An image before and after registration. A and B: the same image before and after registering to a reference frame. C and D: the initial grid and the deformed grid after registration.

Three representative action potential pairs are shown in Fig. 4.3. Motion corrected action potential traces are selected from the key-frame corrected dataset. In Fig. 4.3A, the upstroke of the action potential is completely indistinguishable due to motion. After correction, the shape of action potential is recognizable, although the upstroke is not as sharp. In Fig. 4.3B, the upstroke of the action potential is clear in the trace before motion correction, yet the repolarization is obscure due to motion. The upstroke of the action potential trace was maintained after the correction and the repolarization phase was recovered. Fig. 4.3C shows an example action potential trace from a pixel at the edge of the heart. Pixels at the edge usually encounter significant signal change because the heart

is moving in and out of them. It can be seen that the major motion artifact no longer exist in the motion corrected trace and the upstroke of this action potential trace can be easily detected.

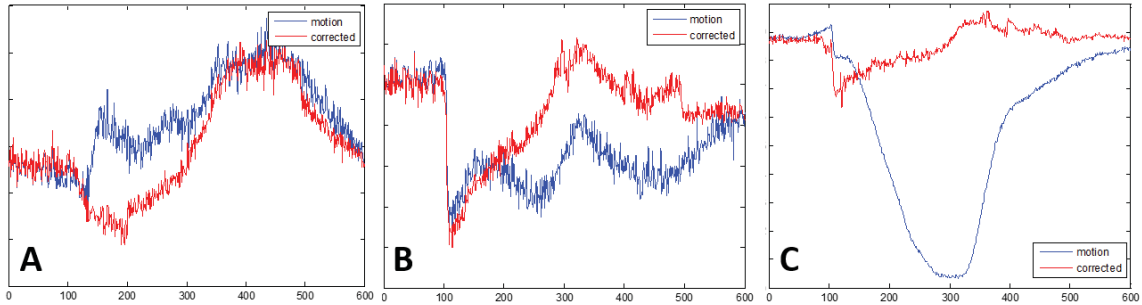


**Fig. 4.3** Representative action potential traces before and after motion correction. Blue action potential traces are from OM recordings with motion. Red action potential traces are from key-frame corrected dataset.

Activation sequence is an important parameter in embryonic cardiac electrophysiology research and is often presented as activation maps. Each pixel is encoded with colors that represent its activation time. At the looping stage of avian hearts, the activation sequence is unidirectional, with faster conduction at the primitive ventricular region and slower conduction at the inflow and the outflow tract.

OM recordings with motion did not produce a well-ordered activation map, as presented in Fig. 4.4A. Activation map of OM recordings after heart motion was suppressed is the gold standard, although the recording itself may have alterations due to the effect of the EC-uncoupler. Activation maps of corrected OM signals using the three registration methods are shown in C, D and E. Part of the inflow region at the top were blurred and does not have any structural feature, as shown in Fig. 4.2A. This is because the heart was looped and that specific region was out of focus when being imaged. Therefore the registration cannot recover this part of the image. The rest of the heart all showed

organized activation patterns. In the first-ref map, conduction pattern at the ventricle region matches the standard the best and the later part of the heart tube does not match the standard. In the mid-ref map, conduction pattern of the middle part of the outflow tract matches the standard pattern and the end of the outflow tract still shows errors. In the key-frame map, activation patterns matched the standard well throughout the heart tube. Therefore, it can be concluded that the key-frame method shows the best registration results.

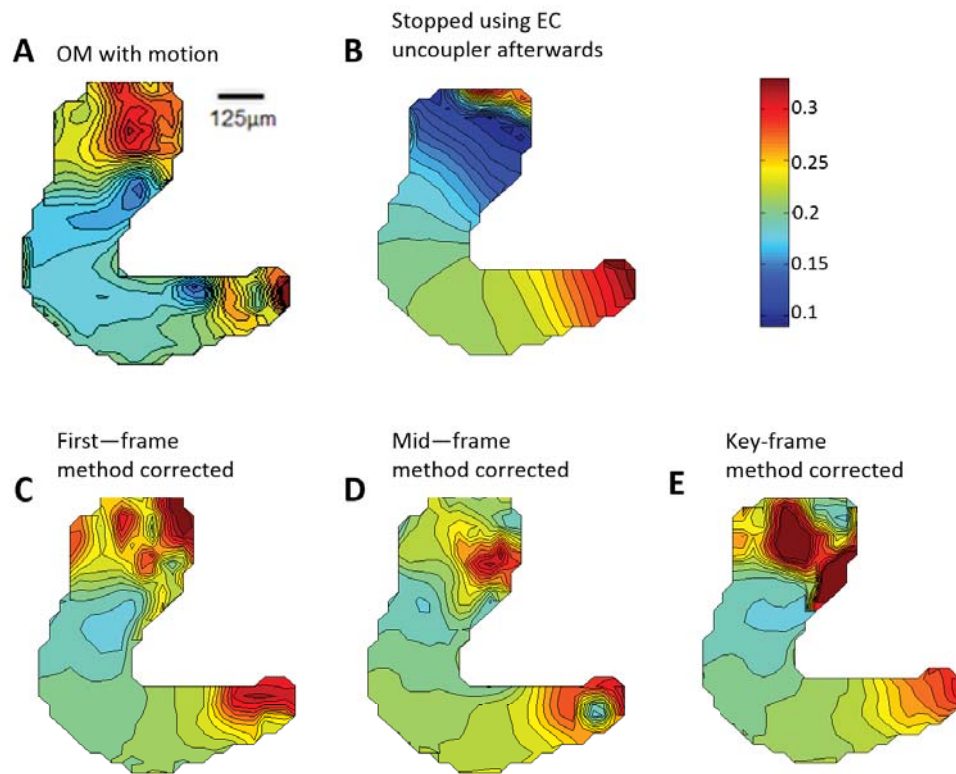


**Fig. 4.4** Activation maps of OM recordings with and without motion correction. A: no motion suppression or correction was applied. B: motion eliminated with cytoD. C: motion corrected with first-ref method. D: motion corrected with mid-frame method. E: motion corrected with key-frame method.

While the activation pattern is mostly qualitative, conduction velocity at the ventricle region and the outflow tract region was also measured to be similar between the key-frame method corrected and the stopped recordings, although the corrected data has higher noise (Table 4.1).

Conduction velocity (mm/sec)	Ventricle	Outflow tract
Stopped	15.4 ± 0.2	2.7 ± 0.2
Corrected (Key-frame)	13.8 ± 0.8	2.9 ± 0.7

**Table 4.1** Conduction velocity measurements with and without motion correction

## **Chapter 5. Cardiac neural crest ablation model**

### **5.1 Introduction**

Congenital heart defects (CHDs) are a major public health concern worldwide [1, 2, 247]. The cause of CHDs is known to be multifactorial, but the steps leading to CHDs are not well understood. Many craniofacial syndromes include CHDs, and are caused by genetic and/or environmental factors. Two such syndromes are DiGeorge syndrome, which is connected to a microdeletion in the 22q11 region of the chromosome, and fetal alcohol syndrome (FAS), which results from prenatal ethanol exposure. Both syndromes are recognized to be associated with the disorder of the neural crest, a tissue composed of a transient, multipotent, migratory cell population involved in the development of many organs and systems [19, 20].

The role of neural crest cells (NCCs) in heart development has been illuminated through NCC ablation experiments in avian embryos [5, 248-251]. The resultant CHDs and craniofacial defects were found to be strikingly similar to those in DiGeorge and 22q11 deletion and other related syndromes in humans. In avian embryos, NCCs located between the mid-otic placode and somite 3 were found to be especially important to heart development, and are therefore defined as the cardiac neural crest cells (CNCCs) [26]. The ablation of CNCCs leads to conotruncal defects as severe as persistent truncus arteriosus (PTA) and double outlet right ventricle (DORV) [26] among other less severe conotruncal defects. Among these defects, PTA is the most representative of the CNCC-ablation model because it consistently exists in all CNCC-ablation animal models while is extremely rare in other CHD models [5, 46, 252].

Through research on CNCC-ablated embryos spanning more than three decades, it is widely accepted that CNCCs are necessary for outflow tract septation and repatterning of the great vessels [26]. Embryos that were CNCC-ablated developed outflow septation defects (*e.g.* PTA), outflow alignment defects (*e.g.* DORV) and many types of great vessel defects including absence, interruption, and incorrect branching [5]. These mature structural phenotypes have been reported many times [46, 250, 251]. However, the quantitative phenotyping of the great vessels, which could identify subtler defects, was not performed in these earlier studies.

Furthermore, cardiac valves were not examined in previous studies as extensively as the patterning of the conotruncal structures. Cardiac valves are small but important structures in the mature four-chambered heart. Atrioventricular (AV) valves ensure blood flow from atria to ventricles and minimize regurgitant flow. Abnormal valve structure and function can lead to reduced cardiac output due to increased regurgitation [253] and result in severe heart dysfunction that can become life-threatening unless the valves are repaired or replaced [254, 255]. Neural crest-derived cells are found in valves [34, 256] and valvular defects of various kinds have been occasionally reported in CNCC-ablation models [257, 258]. However, detailed valve morphology and quantitative measurements have not been reported in previous studies, likely due to the lack of technology to image these small, deep structures in 3D.

It is unclear when and how CNCC ablation affects cardiac valve development. Previous evidence supports the hypothesis that CNCC-related CHDs may involve significant contribution of abnormal early cardiac function. Cardiac cushions, which are valve progenitors, were reported to be abnormal at cardiac looping stages in chicken and mouse

embryos after CNCC deletion [28, 259]. At these stages, CNCCs have accumulated at the pharyngeal arches and have not reached the outflow tract of the heart [26, 260], yet cardiac function was reported to be abnormal [27-29, 261]. Furthermore, early flow and cardiac cushion abnormalities were reported to coexist in multiple diseases models [8, 259]. It has also been shown that changes in retrograde flow during early cardiogenesis can affect *klf2a* expression and valve development [262]. Therefore, investigation of early flow and cardiac cushion morphology in CNCC-ablated embryos would give insights on the timing and form of abnormalities of cardiac structure and function in the CNCC-ablation model.

Previous findings of abnormal cardiac function in CNCC-ablated embryos were increased blood flow velocity, decreased systolic and diastolic blood pressure, depressed contractility (shortening fractions and ejection fractions) and heart dilation as presumed a compensation mechanism at Hamburger and Hamilton (HH) stage 19 in avian embryos [27-29, 261]. Similar findings were reported for other animal models [259, 263]. These measurements were made using tools such as pressure sensors, which were invasive, and microcinematography, which may have decreased accuracy due to limited contrast and 2D imaging of differently oriented hearts. Early cardiac function, especially hemodynamics, has not been reported after these initial experiments. Nor were they linked to any specific cardiac structural defects, such as abnormal cardiac cushions. One reason may be that the available imaging technology restricted the measurements that could be made accurately. Another potential reason is that until recently, cardiac function was often overlooked as a contributing factor in the etiology of CHDs in favor of gene regulation.

Optical coherence tomography (OCT), which provides high resolution (2-30  $\mu\text{m}$ ) 3D imaging at high speed, a field of view (1-3 mm), is well suited to embryonic imaging and

Doppler flow imaging capability [145, 148, 161, 171, 174, 178, 239, 264]. OCT is noninvasive and can image embryos cultured under physiological conditions. By treating tissues with optical clearing methods, the field of view of OCT imaging can be significantly extended [265]. Due to these features, OCT has been extremely useful in studies of avian heart development and CHD phenotyping [174, 180, 264, 266]. Compared to previously available imaging technology used in CNCC-ablation studies (*e.g.*, histology and micro CT) OCT provides rapid, 3D, noninvasive imaging. For functional flow imaging, OCT provides higher temporal and spatial resolution than ultrasound, and does not require contact. Therefore, OCT imaging was used for assaying both early and late developmental stages in this study.

In this study, we aim to qualitatively and quantitatively phenotype CNCC-ablation-related CHDs and investigate early cardiac dysfunction that could potentially serve as a mechanism for late-stage CHDs. We adopted CNCC laser ablation in a quail model that reproduces the CHDs (PTA and DORV) found in 22q11 deletion/DiGeorge syndrome [267, 268]. At cardiac looping stages embryos were imaged with structural and Doppler OCT for body flexure, flow and cardiac cushion analysis. At the four-chambered heart stage, hearts were dissected, cleared and the structure was imaged.

## **5.2 Materials and Methods**

### *5.2.1 Embryo preparation and CNCC ablation*

Avian species have been extremely useful animal models in the study of CNCC functions [5]. Unlike the murine model, the avian model offers access to the neural crest for easy and spatiotemporally specific experimental manipulations. Most importantly, avian embryos can be cultured *in ovo* or in shell-less culture under physiological conditions,

allowing imaging at specific developing stages without the need to sacrifice them. Fertilized quail eggs (*Coturnix coturnix*, Boyd's Bird Company, Inc., Pullman, WA) were incubated in a humidified, forced draft incubator (G.Q.F. Manufacturing Co., Savannah, GA) at 38°C until Hamburger and Hamilton (HH) stage 8-9 (about 30 hours incubation) [47, 250]. The eggs were opened, placed in a shell-less culture in a sterilized 35-mm Petri dish and embryos were stained with neutral red [155, 269]. Similar to previous established methods, the bilateral neural folds from mid-otic placode to somite 3 were laser ablated under the guidance of a microscope [250]. Continuous-wave, 35 mW infrared light at 1465nm (QPhotonics, Ann Arbor, MI) and visible pilot light were focused onto the embryo through a ready-to-use compact scan head [239]. The laser spot size was estimated to be 200  $\mu\text{m}$  on the surface of the embryo, resulting in the irradiance of  $1.1 \times 10^6 \text{ W/cm}^2$ . The laser spot was scanned at 1 Hz for 20-25 seconds on each side of the neural crest. Fig. 5.1 shows a schematic diagram of the ablation system. The embryos were returned to the incubator after ablation until desired stages. To confirm the extent of the ablation area, a cohort of embryos was examined using propidium iodide staining to assess cell viability. Propidium iodide enters and remains in damaged cells with disrupted membranes. In this experiment, 20 $\mu\text{L}$  of propidium iodide at a concentration of 10  $\mu\text{g/mL}$  was applied to the embryo immediately after CNCC ablation. After 5 minutes, fluorescence signals were imaged. Bright field and fluorescence images were collected sequentially and the regions that exhibited strong fluorescence were confirmed to be the regions of CNCCs. Result of PI staining is shown in Fig. 5.2. A group of sham control embryos were exposed to all other treatments except the scanning infrared laser exposure. A second control group of embryos that were not stained with neutral red was also included in the experiment to determine if

the neutral red treatment itself conferred any effects on the parameters that we assayed. There was no difference in any part of the results between the two control groups so we will only present the results from the sham control group. Operations, assays and post processing procedures are described in the following sections and summarized in Table 5.1.

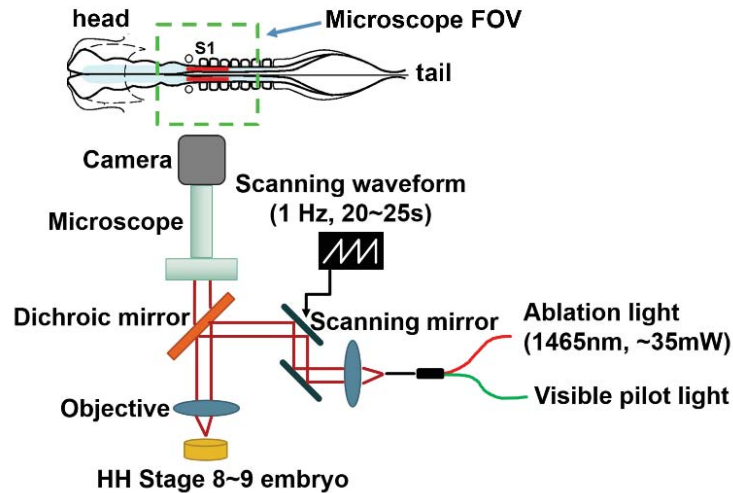


**Fig 5.1** CNCC ablation setup diagram. Two thick red lines on the embryo indicate the ablation region, which is from the mid-otic placode to somite 3. FOV: field of view. Microscope FOV is 1.5 mm × 1.5 mm. S1: somite 1.

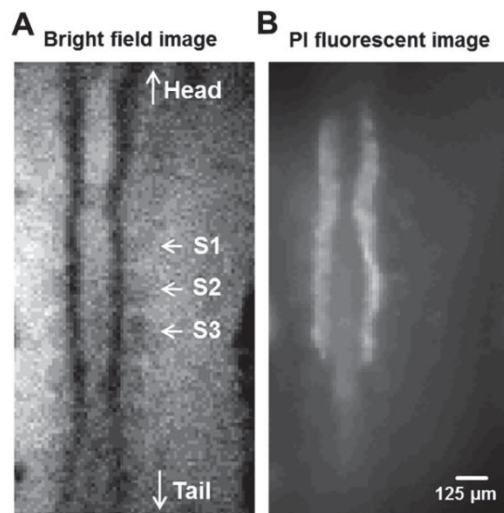


**Fig. 5.2** A: a bright field image of a HH stage 9 embryo immediately after its CNCCs were ablated. The embryo was stained with neutral red before ablation. S1, 2, 3: somite 1, 2, 3. B: a fluorescent image of the same area as panel A with propidium iodide staining to assess cell viability after CNCC ablation of both sides of the neural folds.

### *5.2.2 Imaging and analysis of late-stage septated hearts*

Cohorts of control and CNCC-ablated embryos were incubated in shell-less culture until HH stage 34-35, when the embryonic heart would normally have completed septation to become four chambered. At these stages, the great vessels should have completed the major steps in morphogenesis and achieved their mature asymmetric branching pattern. The left AV valve leaflets should also be distinct although not completely thinned. Hearts from both control and experimental groups were excised, fixed in formalin and optically cleared based on a ClearT protocol [180, 265]. Optically cleared hearts were imaged with a linear-in-wavenumber spectral domain optical coherence tomography (OCT) system [128, 178, 180]. The light source of the OCT system has a center wavelength at 1310 nm and a full-width at half-maximum bandwidth of 75 nm. The axial and lateral resolutions of the system are both  $\sim 10 \mu\text{m}$  in air. The line rate of the OCT system is 47 kHz. 3D datasets acquired from OCT imaging were read into Amira software (Visualization Sciences Group, FEI, Burlington, MA) for 3D reconstruction, visualization and segmentation. Great vessel outer diameters were manually measured on 2D cross sections that were orthogonal to the vessels, as shown in Fig. 5.3. To measure each vessel, at least two measurements (normally two or three) were made in different directions. Then the measurements for each vessel were averaged. Measurements were made at the location when a great vessel just branches off from its main trunk (aortic trunk or pulmonary trunk). Vessel inner diameters were not measured because they often appeared to have irregular shapes that were difficult to quantify. Left AV valve leaflets were manually segmented and the volume was computed.

	Day 1 (HH stage 8-9)	Day 8 (HH stage 34-35)			post processing
Cohort 1	operation	assay	purpose	sample size (sham, experimental)	
	sham / ablation	OCT volume imaging <i>ex vivo</i>	great vessels	n = 8, 18	morphology analysis, diameter quantification
			valves	n = 9, 24	segmentation, morphology analysis, quantification of leaflets
	Day 1 (HH stage 8-9)	Day 3 (HH stage 19-20)			Post processing
Cohort 2	operation	assay	purpose	sample size (sham, experimental)	
	sham / ablation	pulsed Doppler OCT <i>in vivo</i>	flow	n = 8, 26	waveform analysis and retrograde flow quantification
		OCT volume imaging <i>in vivo</i>	body flexure	n = 8, 26	combining images
		OCT volume imaging <i>ex vivo</i>	cardiac cushions	n = 5, 10	morphology analysis and quantification

**Table 5.1** A summary of operation, assay and post processing performed on a cohort of embryos for day 8 analysis and a cohort of embryos for day 3 analysis.

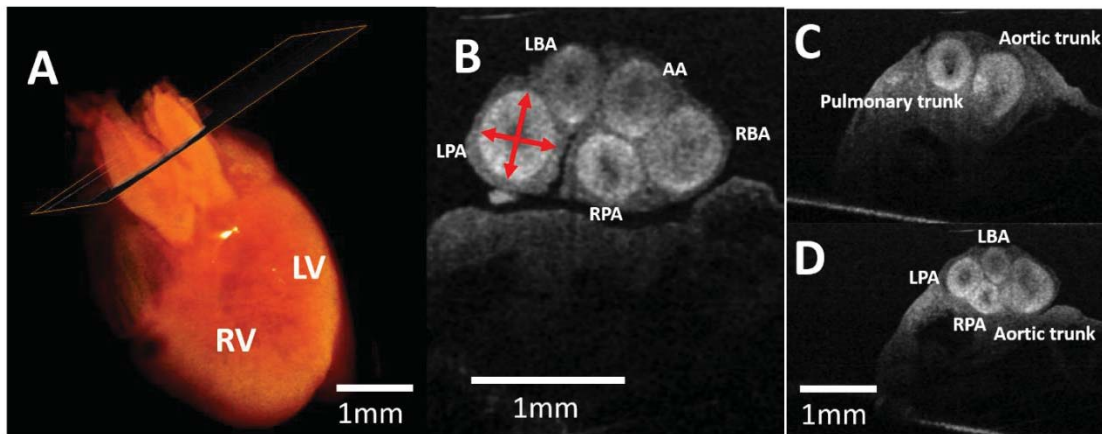


**Fig 5.3** Example of great vessel measurement on a control embryo. A: 3D volume reconstruction image of a sham control embryo. An orthogonal slice cut through the great vessels in this panel indicates a cross-sectional image that was used to measure the great vessel diameters. B: the orthogonal slice in A. The outer diameters of the great vessels are very close to a circular shape. Red double head arrow: great vessel measurements. C and D are images showing the great vessels at different locations in the heart. C shows the proximal end of the great vessels. The aortic and pulmonary trunk are present. D shows a location that the LBA just branched off the aortic trunk. RBA: right brachiocephalic artery, LBA: left brachiocephalic artery, AA: aortic arch, RPA: right pulmonary artery, LPA: left pulmonary artery. LV: left ventricle, RV: right ventricle.

### *5.2.3 Structural and functional imaging of embryos at the cardiac looping stage*

Control and CNCC-ablated embryos in shell-less culture were moved from the incubator into a customized environmentally controlled OCT imaging chamber [178] at HH stage 19-20 (late cardiac looping stage) to maintain physiological conditions. First, whole embryos were imaged with OCT to visualize body flexure and accurately stage the embryos. Three 4 mm by 4 mm regions were imaged for each embryo to cover the entire body area. In post processing, projection images were generated from the OCT volumes by volume rendering in Amira software. These projection images were stitched together to generate a single image of the entire embryo. Staging of the embryos was primarily based on the limb development [270]. Other features such as body/ head curvatures can be significantly altered in the CNCC-ablated embryos and are not reliable features for staging. After whole-body imaging, pulsed Doppler traces were acquired from the right vitelline artery of each embryo by OCT M-mode Doppler imaging. The flow patterns of the vitelline arteries have been previously reported to reflect cardiac function [8, 175]. The percentage of retrograde flow was calculated as the ratio of the negative flow area and the positive flow area [8, 175]. Morphology phenotypes were determined from the flow traces by three blinded experts. Finally, after OCT M-mode Doppler imaging, the whole embryo was dissected from the yolk and fixed in formalin and the hearts were imaged with OCT. The hearts remain attached to the body to preserve their shape and orientation during imaging. Segmentation and analysis of the cardiac cushions were performed using Amira software.

### *5.2.4 Statistical analysis*

For the data acquired from the day 8, four-chambered hearts, Student's t-test was used for both great vessel measurements and valve volume measurements (\*  $p < 0.05$ ). Day 3

survival rate calculation combined the number of survivors from the day 3 cohorts and the number of survivors on day 3 from the day 8 cohorts. For data from the day 3, cardiac looping-stage embryos, comparison of percentage of retrograde flow, and cushion volumes was made using Student's t-test (\*  $p < 0.05$ ). Correlation coefficients were calculated using Matlab (MathWorks, Natick, MA). Cushion morphology comparisons and correlation of cushion and flow phenotypes were made using Fisher's exact test.

### **5.3. Results**

#### *5.3.1 Great vessel defects*

Cohorts of experimental and control embryos were allowed to develop until HH stages 34-35 (day 8) when normal embryos would have completed cardiac septation, great vessel branching and valve leaflet differentiation. The survival rates of the sham control group and the experimental group were 55% (11/20) and 41% (24/58), respectively. Gross body defects were identified during dissection. Heart defects were diagnosed using 2D sections and 3D volume reconstructions acquired from OCT imaging. Embryo phenotypes are summarized in Table 5.2. When the hearts were excised, the great vessels were cut at a position roughly 2 mm away from the heart. Therefore defects in the distal portion of the great vessels were not identified here. Control embryos at this stage have five great vessels in cross section at that level: right brachiocephalic artery (RBA), left brachiocephalic artery (LBA), aortic arch (AA), right pulmonary artery (RPA), and left pulmonary artery (LPA). They are separated into the aortic trunk and the pulmonary trunk and both trunks are connected in the middle of the base of the heart. In persistent truncus arteriosus (PTA), the pulmonary and aortic vessels branch from a single trunk and a ventricular septal defect is present (Fig. 5.4). In “absent great vessel defects, at least one vessel is missing at the level

assayed. Other defects observed were great vessel stenosis and incorrect branching. These defects sometimes coexisted in the same heart. Examples of 3D volume reconstruction of great vessel defects are shown in Fig. 5.5 (A-D).

Parameter	Sham	CNCC-ablated
Number of survivors	11	24
Survival rate	55%	41%
Normal body	10 (91%)	18 (75%)
Unfused chest wall	1 (9%)	5 (21%)
Twisted body	0 (0%)	1 (4%)
Heart with obvious defects	0 (0%)	11 (46%)
PTA	0 (0%)	6 (25%)
DORV	0 (0%)	2 (8%)
Absent great vessel	0 (0%)	4 (17%)
Great vessel stenosis	0 (0%)	3 (13%)
Incorrect great vessel branching <sup>a</sup>	0 (0%)	1 (4%)

**Table 5.2** Day 8 (HH stage 34) Embryo Phenotypes

a: incorrect great vessel branching other than the types listed above

PTA: persistent truncus arteriosus

DORV: double outlet right ventricle

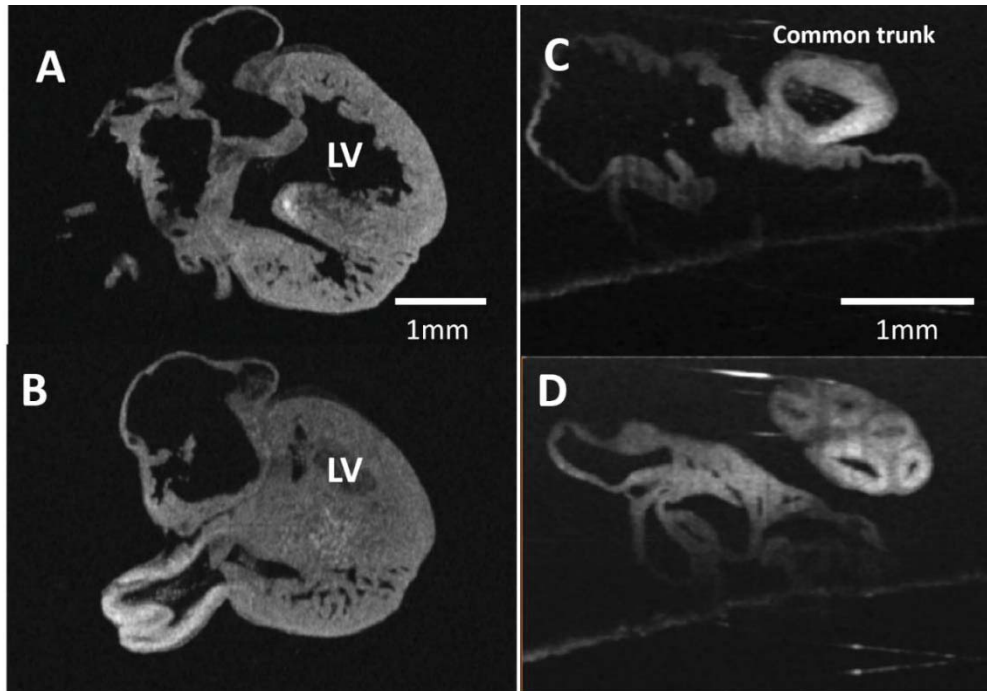


**Fig. 5.4** An example of a heart with PTA. A and B: heart cross sectional images of the chamber. A ventricular septal defect is present and can be observed in A. A large, single trunk is connected to the right ventricle. C and D: orthogonal views for observing the great vessels. C: the proximal end of the great vessels. A common trunk is present. D: five great vessels branched from the common trunk.

Here we also made quantitative measurements of hearts with all five great vessels present at the level assayed, in addition to qualitative assessment of the great vessel defects. The measurement of the great vessels were made on the OCT cross sectional images orthogonal to the vessels, as shown in Fig. 5.5. The outer diameters of the AA and the RBA are significantly smaller in the CNCC-ablated embryos compared to the controls (by 11% and 16% respectively). The diameter of the LBA has a decreasing trend without reaching statistical significance, possibly due to large biological variances.

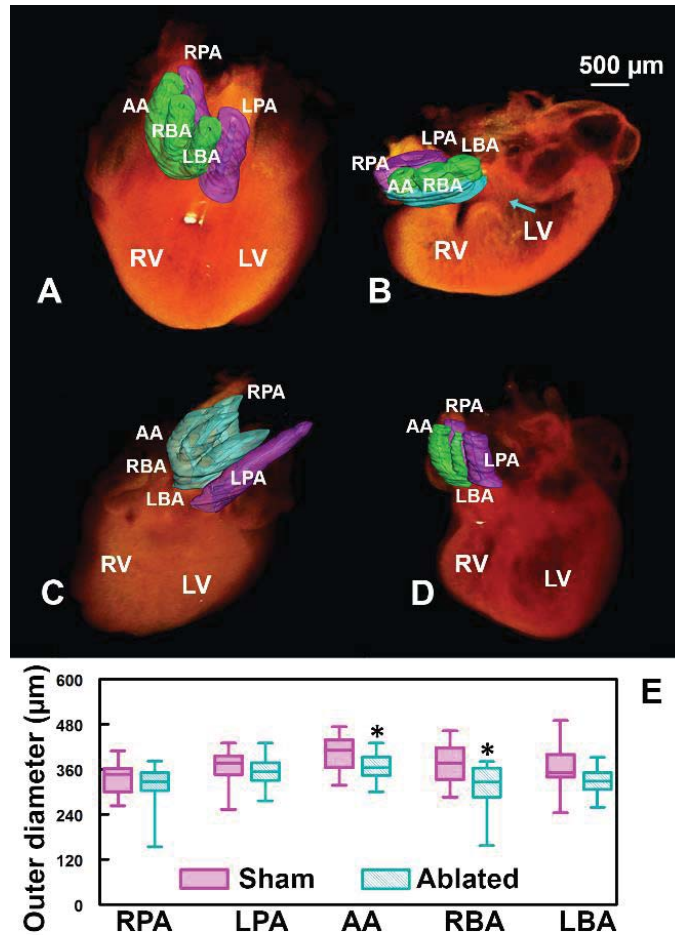


**Fig. 5.5** CNCC-related great vessel defects. A-D: 3D OCT volume reconstructions and great vessel segmentation. Green: the aortic trunk vessels, purple: the pulmonary trunk vessels, cyan: branching errors. A: control embryonic heart. B: an example of PTA. The region with cyan color at the great vessels represents the common trunk. Arrow in B: ventricular septal defect. C: an example of incorrect branching. The aortic trunk branches into four vessels instead of three and the pulmonary trunk branches into one instead of two. D: absent great vessel. E: box plot of great vessel outer diameter measurements. The box represents 25% - 75% and the whiskers represent the range. AA and RBA in the CNCC-ablated group are significantly smaller than the control group. \*  $p < 0.05$  Green: the aortic trunk vessels, purple: the pulmonary trunk vessels, blue: branching errors; RBA: right brachiocephalic artery, LBA: left brachiocephalic artery, AA: aortic arch, RPA: right pulmonary artery, LPA: left pulmonary artery. LV: left ventricle, RV: right ventricle.

### 5.3.2 Left atrioventricular (AV) valvular defects

Left AV valvular defects were consistently observed in CNCC-ablated embryos. At HH stages 34-35, after optical clearing, the internal structures of the heart including the septum,

trabeculae and the valves can be clearly identified in OCT cross sections. Normally developed left AV valve leaflets at this stage are relatively thick and consist of a longer septal leaflet and a short and thick mural leaflet. These two leaflets together form a V-shaped structure which results in a relatively large contact region for the surfaces of the valve leaflets (Fig. 5.6A). This orientation of the two leaflets ensures unobstructed blood flow from the atrium to the dilating ventricle and impedes regurgitant flow when the ventricle contracts. Blood flow through the heart can be aberrant if the leaflets are malformed or the positions of the two leaflets are abnormal. One obvious potential consequence is regurgitation, which in the long term may lead to more severe defects. Almost all embryos from the CNCC-ablated group presented some degree of left AV valvular abnormalities (Fig. 5.6). One heart (Fig. 5.6B) had very thin septal and mural leaflets. Another heart had PTA with the two valve leaflets forming a bowl shape rather than the normal V-shape (Fig. 5.6C). This resulted in very little contact of the two valve leaflets along their sides. A small gap between the two valve leaflets was detected from a rotated view of valve leaflet segmentation. This specific phenotype was detected in five out of six PTA hearts, with gaps of various sizes between the valve leaflets. In another example the relative position of the valve leaflets results in a reversed V-shape orientation (Fig. 5.6D). Volumes were determined for each leaflet. Overall leaflet volumes (septal, mural and total leaflet volumes) of the CNCC ablation group were significantly smaller than controls. Interestingly, it was noticed that the leaflet volumes of PTA hearts (6 hearts) were quite similar to the controls so they were then separated out. PTA and non-PTA experimental groups were each tested against the sham control group and the results are shown in Fig. 5.6E. The non-PTA hearts from the ablation group showed significantly

decreased septal leaflet volume (43% decrease,  $p < 0.05$ ), mural leaflet volume (38% decrease,  $p < 0.05$ ) and total volume (40% decrease,  $p < 0.05$ ) compared to the sham controls. The PTA group did not show significant differences in valve leaflet volumes from the controls.

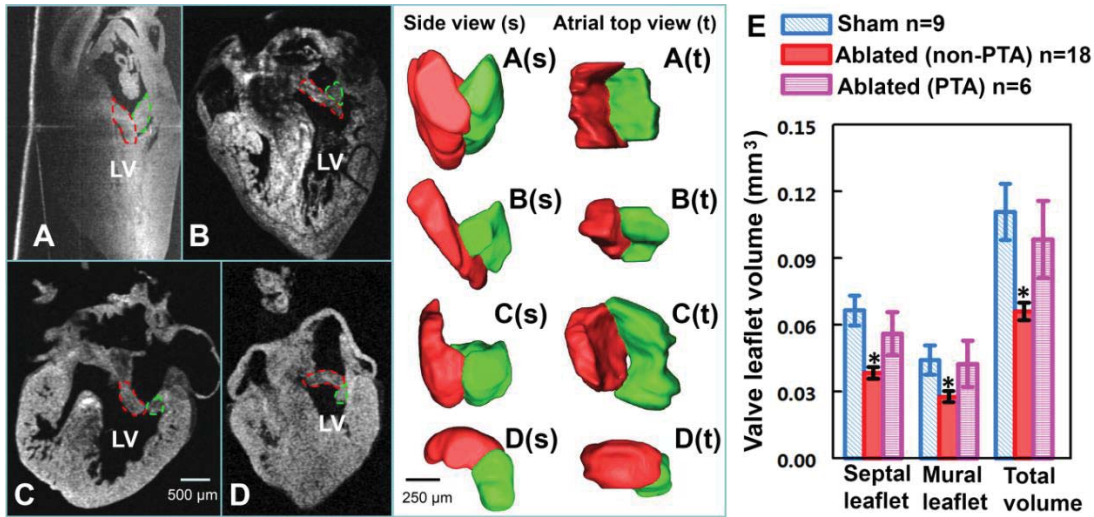


**Fig 5.6** CNCC-ablated embryos exhibited left AV valve defects. Panels A-D are 2D OCT cross sections of four-chambered hearts from a sham control embryo (A) and three CNCC-ablated embryos (B-D). Their left AV valve leaflets are outlined by red (septal valve leaflets) and green (mural valve leaflets) dashed lines. A(s)-D(s) are side views of 3D reconstructions of the left AV valve leaflets that correspond to A-D and A(t)-D(t) are views of the atrial side. E shows results of volume measurements of left AV valve leaflets for 9 sham control embryos, 18 CNCC-ablated embryos that do not have PTA and 6 PTA hearts from the CNCC-ablated embryos. Error bar: standard error. \*  $p < 0.05$  LV: left ventricle.

### 5.3.3 Body flexure abnormalities at early stages

The survival rates at HH stage 18-30 were 83% and 68% for sham and CNCC-ablated embryo groups respectively.

Body flexure abnormalities at late looping stages (HH stage 18-20) were mentioned in previous CNCC-ablation studies yet were not presented or described in detail [251, 271]. However, these structural features of the body may be associated with other serious defects and syndromes. For example, scoliosis has been correlated with the development of heart defects [272, 273]. At this stage, control embryos on the yolk (Fig. 5.7A and Fig. 5.8A)

usually have a relatively straight trunk with the right side of its head exposed and the head curving smoothly with the looped heart easily observable on the right side of the body tucked under the head (labeled with blue dashed-line circles in Fig. 5.8). The right wing and leg buds are located at the middle and the end of the trunk, both pointing forward (blue arrows in Fig. 5.8A). CNCC-ablated embryos, in contrast, often have a different degree of body twisting and rotation (Fig. 5.7B-E). Sometimes, the head and/or the heart of the embryo can be buried under the body (Fig. 5.7D,E). The proportions are summarized in Table 5.3. The anatomy of a pale white embryo on the pale yellow yolk is difficult to visualize using a stereomicroscope. Standard stereomicroscope images only provided good contrast for red blood on a yellow yolk background while the OCT image provided clear delineation of the embryo body and other structures such as the aortic arch, the somites and the limb buds. This comparison can be clearly observed in Fig. 5.7 and Fig. 5.8. Because head and curvature features can be hidden due to abnormalities in development after experimental treatment, the limb buds in the OCT projection images were used to stage the embryos. They appeared to be less affected in their morphology compared to other features.

	sham (n=8)	CNCC-ablated (n=26)
Heart rate, bmp	216 ± 27	223 ± 14
Normal body	100%	31%
Moderately-twisted	0%	38%
Severely-twisted	0%	31%

**Table 5.3** Heart rate of the control and CNCC-ablated embryos were not significantly different. A significant portion of CNCC-ablated embryos present moderately-twisted body flexures or severely-twisted body flexures.

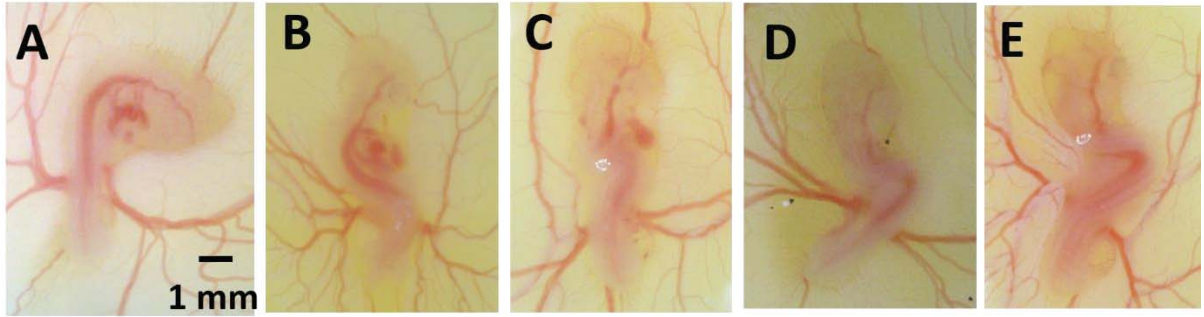


**Fig 5.7** Microscopy images of embryo body flexures. A: control embryo. B and C: CNCC-ablated embryos with moderately twisted bodies. Their heart can be seen, although appears to be different than the controls possibly due to abnormally developed heart or a rotated angle. D and E: severely twisted CNCC-ablated embryos. Their hearts are not visible from the surface.

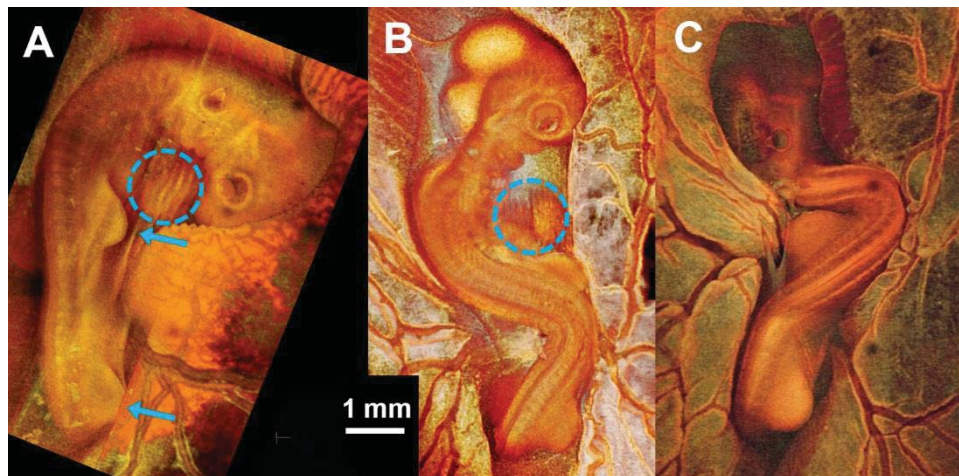


**Fig 5.8** Whole embryo images demonstrating body flexure (HH stage 19-20). A (a sham control embryo), B and C (two CNCC-ablated embryos) are projection images from 3D OCT volume rendering. A, B and C are the same embryos in Fig. 5.7 A, B and E respectively. Blue arrows point at the limb buds that were used for staging the embryos. Blue dashed-line circles: embryonic hearts (with artifacts due to the beating motion). Heart in C is not visible. The limb morphology indicates that all three embryos are between HH stages 19-20, closer to HH stage 20.

#### 5.3.4 Abnormal flow at cardiac looping stages

At HH stage 19-20, M-mode Doppler OCT images were obtained from the right vitelline artery of each embryo. These particular stages were chosen for live imaging assays because embryos at these stages are undergoing important cardiogenesis events such as endothelial-

to-mesenchymal transition (EMT) in the endocardial cushions and conduction repatterning [36, 274]. As shown in the control embryos and previously reported healthy embryos, a pulsed Doppler trace recorded from a normally developing embryo consists of a positive peak, which is forward flow and a small but clearly detectable negative peak, which is retrograde flow [8, 175].

Quantitative measurements showed that the retrograde flow percentage (ratio of the area of the negative peak to the area of the positive peak) in normal embryos is consistently low (~ 3%). The CNCC-ablated embryos, in contrast, were found to have significantly increased percentage of retrograde flow and large variability (Fig. 5.9B, C and E).

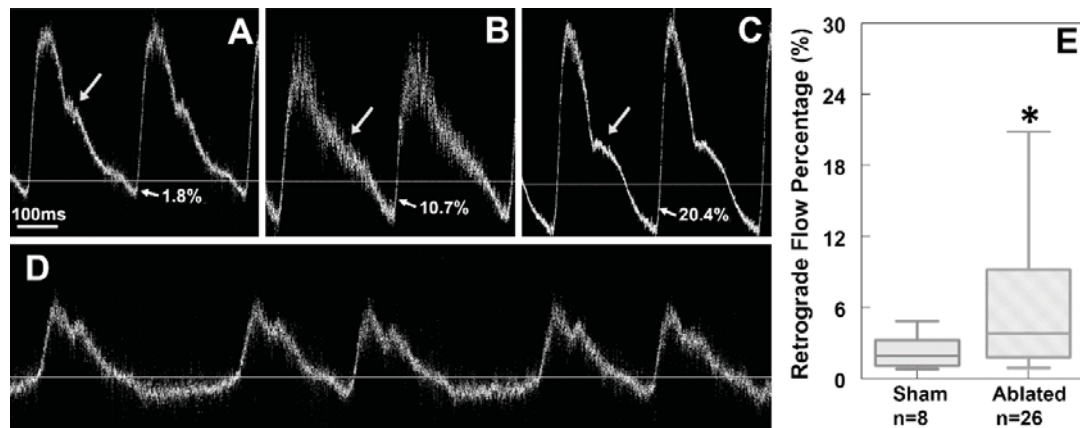


**Fig 5.9** CNCC-ablated embryos have abnormal flow profiles at HH stage 19-20. A-D are pulsed Doppler traces from a sham control embryo (A) and three CNCC-ablated embryos. The prominent shoulder phenotype is point out by arrows in A, B and C. The retrograde flow percentage (indicated in yellow arrows and number in A-C) is calculated as the ratio of negative peak area and the positive peak area. The retrograde flow percentages of the two examples are 10.7% and 20.4% for B and C respectively. D: A pulse Doppler trace from another experimental embryo that exhibited an arrhythmia. E: box plot of retrograde flow percentage for the control group and the experimental group. The box represents 25% - 75% and the whiskers represent the range. \*  $p < 0.05$ .

It was also noticed that control embryos usually have a shoulder at around the middle of the falling slope of forward flow. In contrast, this shoulder was sometimes absent, reduced or at a different position in the CNCC-ablated group (Fig. 5.9B). We also observed

one CNCC-ablated embryo with arrhythmia (Fig. 5.9D). There was no difference between the control and ablated groups in heart rate ( $p = 0.37$ ). No correlation was found between body flexure abnormalities and retrograde flow measurements.

#### *5.3.5 Abnormal cardiac cushions at cardiac looping stages*

Abnormal flow waveforms and increased levels of percent retrograde flow in CNCC-ablated embryos suggest the presence of anomalies in cardiac cushion function and morphology. After the functional pulsed Doppler assay, each embryo was dissected, fixed and prepared for OCT structural imaging (Fig. 5.10). Cardiac cushions from volumetric images of 5 control embryos and 10 CNCC-ablated embryos were manually segmented in Amira software. Cardiac cushions at the atrioventricular junction (AVJ) were segmented into two regions, the inferior AV cushion, which is a clearly delineated region, and the superior AV cushion, which is connected to the cushions in the outflow tract. The inferior and superior AV cushions in control embryos are thick and usually contact each other, resulting in a largely occluded lumen area (Fig. 5.11A). The outflow tract cushions of control embryos are usually thick and cover the whole length of the outflow tract. In the experimental group, 6/10 embryos clearly showed significant gaps between the inferior and superior AV cushions and much reduced lumen coverage, as shown in 2D and 3D images in Fig. 5.10 (two middle columns) and cross sectional images in Fig. 5.11. AV gap measurements are shown in Fig. 5.11D. Furthermore, 6/10 experimental embryos showed reduced luminal coverage of the outflow tract cushions. Fisher's exact test suggested that the gap phenotype and the reduced outflow tract cushion coverage phenotype of the experimental group are features that are significantly different from the controls (Table 5.4). These two types of defects did not correlate with each other (correlation coefficient =

0.58,  $p = 0.10$ ). Although cushions appear to be quite different, cushion volumes calculated were not significantly different between the two groups ( $p = 0.13$ ). It is potentially because CNCC-ablated group developed dilated hearts (Fig. 5.10B and Fig. 5.10C compared to Fig. 5.10A) and much larger lumen areas (Fig. 5.11B and 5.11C compared to 5.11A). Therefore a similar amount of cardiac cushions were spread over a much larger region.

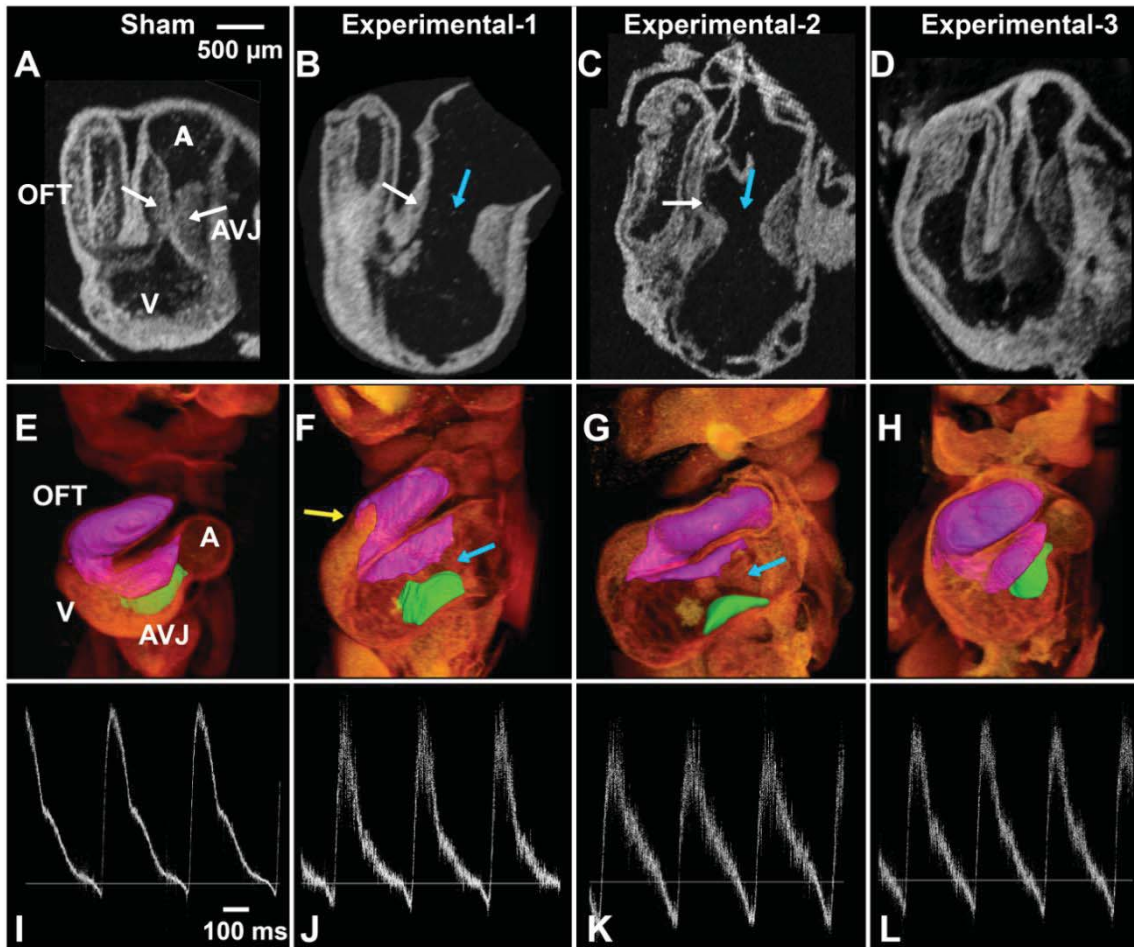


**Fig. 5.10** CNCC-ablated embryos have abnormal endocardial cushions at HH stage 19-20. Row 1 (A-D) are 2D OCT sections of HH stage 19-20 embryonic hearts. Row 2 (E-H) are 3D OCT volume rendering and cushion segmentations (green: inferior AV cushion, purple: fusion of superior AV cushion and outflow tract cushions). Row 3 (I-L) are the flow traces recorded *in vivo*. Panels in each column shows data from the same control or experimental embryo *in vivo* (pulse Doppler trace) and *ex vivo* (3D heart structural imaging). White arrows: the superior and inferior cushions. Blue arrows: large gaps between the superior and inferior AV cushions in the ablated embryos (B,C,F and G). yellow arrow: reduced cushion coverage in an ablated embryo. D: a CNCC ablated embryo that appeared to have relatively normal cushions. A: atrium, AVJ: atrioventricular junction, V: ventricle, OFT: outflow tract.

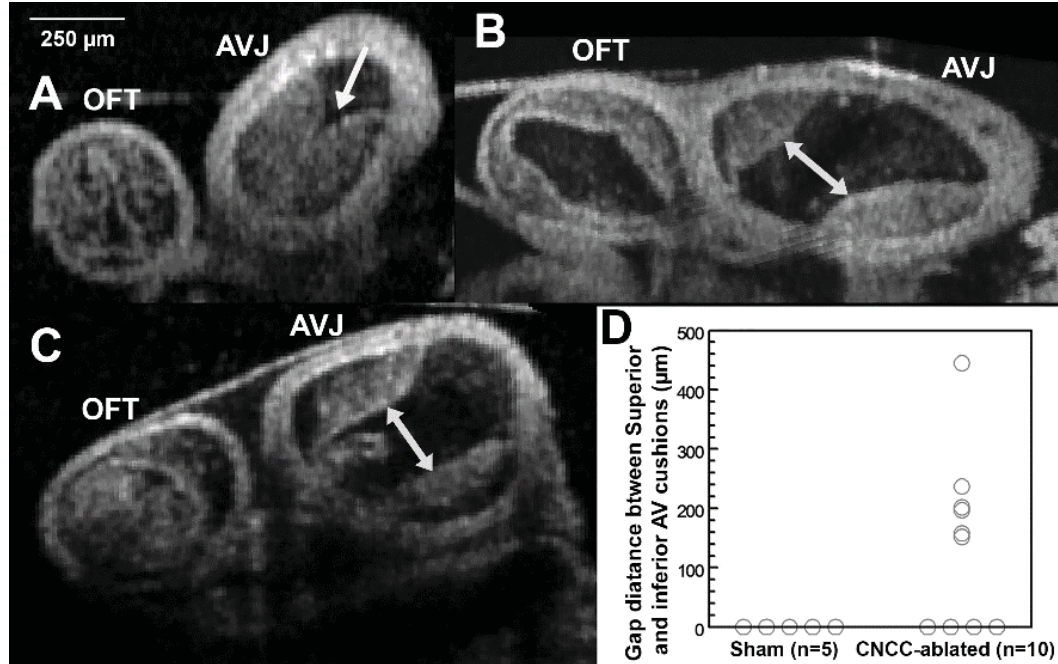


**Fig. 5.11** OCT cross-sectional images of the AV cushions. A: a control embryonic heart. B and C: CNCC-ablated embryonic hearts. Arrow in A: the inferior and superior AV cushions contact each other and fill most of the lumen. Double head arrows: gaps between the inferior and superior AV cushions in ablated hearts. D: gap distance measurements. OFT: outflow tract. AVJ: atrioventricular junction. All three images share the same scale bar on the top left corner.

Inferior and superior AV cushion	no gap	gap	two-tail <i>p</i> value
sham	5	0	0.044
ablation	4	6	

Outflow tract cushion	full coverage	reduced coverage	two-tail <i>p</i> value
sham	5	0	0.044
ablation	4	6	

**Table 5.4** Analysis of cardiac cushion phenotypes including the gap phenotype between cushions at the AVJ and reduced outflow tract cushion coverage phenotype of the luminal surface.

### *5.3.6 Potential links between two early-stage defects*

Because the same embryos have provided both pulsed Doppler flow measurements and cushion measurements, these two datasets can be compared and correlated. Phenotypes and measurements considered here are: shoulder phenotypes (normal or abnormal) and retrograde flow percentage from the flow trace, correlated with AV cushion phenotypes (gap or no gap in the AV cushions and full or reduced coverage in the outflow tract cushions) and cushion volumes from the cardiac cushion analysis. Among 15 embryos, including both sham and CNCC-ablated embryos, for which cushion volumes were measured, 2 had flow traces that were too noisy to confidently distinguish the presence of the shoulder feature, and were therefore excluded from this analysis. All control embryos had a low percent retrograde flow, no or negligible gap between inferior and superior AV cushions and complete outflow tract cushion coverage. Among the embryos that had significant gaps between inferior and superior AV cushions, 4/5 had an absent shoulder in pulsed Doppler flow traces. All 8 embryos that had no gaps between AV cushions had normal shoulders in their pulse Doppler traces. Fisher's exact test suggested that there was a strong correlation between the cushion gap phenotype and the shoulder feature in pulsed Doppler trace (examples are shown in Fig. 5.10, and correlation is summarized in Table 5.5). This indicates that the normal AV cushion morphology during heart beating might be responsible for the shoulder feature in the flow pattern. No correlation was found between the AV cushion gap and increased levels of percent retrograde flow. No correlation was observed between outflow tract cushion coverage ( $p = 0.27$ ) and percent retrograde flow. Retrograde flow percentage was not significantly correlated with total cushion volume

either ( $p= 0.14$ ). The cause of increased retrograde flow percentage might be more complicated than being determined by a single parameter that was assayed.

AV cushion\ flow	normal shoulder	abnormal shoulder	correlation coefficient	<i>p</i> - value
gap	1	4	0.843	0.007
no gap	8	0		

**Table 5.5** Correlation between AV cushion gap and flow shoulder phenotype.

#### 5.4. Discussion

Late-stage heart defects observed in our CNCC-ablation quail model were consistent with documented CHDs in NCC-related clinical syndromes as well as previous CNCC-ablation models in other species such as chicken or mouse [5, 275]. These defects involve a spectrum of great vessel abnormalities [5]. Previous studies have mostly focused on patterning defects of the great vessels and the associated molecular expression changes [46, 252, 276, 277]. More detailed structural alterations were largely ignored. Changes in great vessel dimensions may be important indicators or predictors of more severe diseases such as compromised cardiac function. In our study, we have quantitatively measured great vessel diameters and detected significantly decreased great vessel sizes in the CNCC-ablation model. CNCCs play an important role in repatterning the aortic arch arteries into the mature great arteries as well as providing smooth muscle cells for the great arteries themselves [6, 26]. This decrease in vessel diameter may be due to fewer CNCCs reaching and populating the aortic arch mesenchyme. The decreases of great vessel diameters also support the notion that quantifying the diameters of great vessel may reveal that CNCC-related defects are more prevalent than reported in the literature. These “minor” alterations

may change the relative flows through each branch and this may lead to more severe consequences in the future, although further research is needed to test this hypothesis.

We have also qualitatively and quantitatively phenotyped valvular defects. Changes in valve morphology and/or the relative position of leaflets are important indicators for impaired cardiac function [278]. Any failure in valve closure can cause leakage and increase retrograde flow, reducing cardiac output, potentially causing heart failure [279]. Abnormal morphology as well as decreased volume of the left AV valves observed in the CNCC-ablated embryos can be an indication of disrupted cardiac function. Such abnormalities at this stage may result in more severe problems in further development of the valves, the heart and even the rest of the body and the placenta.

CHDs can be initiated by genetic or functional abnormalities at very early stages [8, 280]. In this study we investigated early onset of cardiac abnormalities with regard to early cardiac hemodynamic function. At early developmental stages, hemodynamics and cardiac cushions at early stages were previously examined because they are critical factors for outflow tract and cardiac valve development [262, 281]. During cardiac development, immature valves and valve progenitors perform functions similar to mature valves in the adult heart [259, 282]. They allow forward flow and minimize reverse flow. The resultant flow patterns and biomechanical forces can in turn affect molecular signaling or gene expression and cardiogenesis [262, 283-286]. Any alterations in this feedback loop can affect normal heart development. It has been shown previously by multiple groups that chamber morphology, flow and other functions are all critical factors in cardiogenesis and valve development [262, 283, 287, 288].

With Doppler OCT, we were able to detect blood flow profiles, calculate percent of retrograde flow and correlate flow profiles to cardiac cushion structure and other features at cardiac looping stages. We consistently observed the prominent shoulder feature in pulse Doppler flow traces from normally-developing looping-stage embryos [8, 175] and absent shoulder phenotype in CNCC-ablation embryos. The absence of prominent shoulders was correlated with gaps between the AV cushions. This suggested that in CNCC-ablated embryos, the AV cushions could fail to appose and close the lumen properly during the cardiac cycle, therefore leading to abnormal flow through the AVJ and resulting in a pattern change in the overall flow profile [282]. However, we did not detect a significant decrease in cardiac cushion volume. The gaps are more likely caused by abnormal cushion distribution or changes of the overall shape and size of the AV canal, rather than simply the volume of the cushions. Heart dilation was reported to be a compensatory mechanism for decreased heart function [29]. In our experiment, CNCC-ablated embryos also suffered from dilated heart tubes where the normal volume of cardiac cushion may be inadequate to close the lumen properly (Fig. 5.11). Our results were consistent with the observation in a NCC deficient mouse model using ultrasound and microCT to measure flow and cushion thickness at E11.5 (a later developmental stage than HH stage 19 in avian species). They found that NCC deficient mice exhibited retrograde flow at the dorsal aorta and thinner cardiac cushions than the wild types [259].

Cardiac function and morphology are known to influence each other [283, 287]. For example, alterations of retrograde flow in the zebrafish led to arrested valve growth and affected the normal expression of *klf2a*, a transcription factor that is crucial for normal valve development [262]. On the other hand, it has been shown that cardiac cushion

size/thickness by itself can impact signaling, gene expression and electrical events in the early embryonic heart [85]. It is unclear whether cardiac function or morphology initiated the abnormalities that we observed at HH stage 19-20 in the CNCC ablation model. In the avian embryo, CNCCs start to populate the pharyngeal arches at HH stage 13 and do not migrate to the heart until HH stage 25 [260]. One possibility is that the absence of CNCCs around pharyngeal arches contributes to abnormal flow by altering resistance or compliance, followed by cardiac cushion malformation due to abnormal flow. Another possibility is that cushion morphology is altered before hemodynamics. It was suggested that FGF8 might be responsible for the early myocardium dysfunction [5]. These dysfunctions include abnormal cardiac jelly formation at HH stage 14 [32], which could cause abnormal flow. In the future, assaying cardiac function and imaging cardiac jelly formation at even earlier stages may potentially resolve these two different possible causes.

In this study, we also presented that CNCC-ablated embryos exhibit body flexure abnormalities at cardiac looping stages, which were previously mentioned but not focused on [251, 271]. In most studies, the embryos with these deformities were not analyzed because their hearts were usually underneath the body and difficult to visualize using conventional stereomicroscopes. However, the body twist can be a very important feature, as Manner et al. reported that these embryos had a significantly lower survival rate when compared to CNCC-ablated embryos that did not have a body flexure defect [271]. Similar abnormal embryo body flexure was observed in other heart disease models including zebrafish [289] and quail [8]. In the fetal alcohol syndrome (FAS) quail model that we have established, ethanol-exposed embryos exhibited very similar body twisting as seen in this study as well as similar abnormalities in hemodynamics. [8]. Ford et al. has shown that

optically pacing the looping-stage embryonic heart at a higher than intrinsic rate for five minutes to exhaust the heart at HH stage 14 led to body flexure abnormalities at HH stage 19 and CHDs at late stages [290]. This suggested that twisting of the body axis may be a secondary effect resulting from earlier abnormal cardiac function or abnormal cardiac looping. This evidence of early body phenotypes in heart disease models is consistent with the clinical finding of the correlation of spinal abnormalities to cardiac defects [272, 273].

Besides the body twisting, many early and late-stage phenotypes of the CNCC ablation model have strikingly resembled our previously published FAS quail model [8, 291]. At HH stage 34-35, defects such as absent great vessels and incorrect great vessel alignment were observed in both models. Measurements of the outer diameters showed 6%-10% and 11%-16% decreases in the FAS and CNCC-ablation models respectively for the aortic branches, where the smooth muscle cells are mainly derived from CNCCs. Another late-stage phenotype identified in both models was abnormal left AV valve. Besides morphological similarities, the total volume of the valve leaflets of the FAS and CNCC ablation models were decreased by 45% and 40%, respectively, as measured by 3D OCT imaging. This may be a direct effect of CNCC disorder or an indirect influence through abnormal early cardiac morphology and function. These early cardiac abnormalities include the lack of a prominent shoulder in the flow waveform, increased percent retrograde blood flow and defective cardiac cushion formation. It was noticed many years ago that DiGeorge syndrome and FAS share common characteristics including abnormalities of the face, cardiovascular system, central nervous system, and immune system [17, 18]. Numerous studies have demonstrated the influence of alcohol exposure on the neural crest cells (NCCs), which results in increased NCC apoptosis or impeded

NCC migration signaling [20-25]. The similarities described here between the quail FAS and CNCC-ablation models further support the theory that the reduction of NCCs may at least be partially involved in ethanol-induced birth defects, including CHDs [20].

Based on experimental results from this study as well as previous studies, the following mechanism involving cardiac functions is proposed in Fig. 5.12. Genetic or environmental factors such as alcohol exposure may cause CNCC dysfunction. In this study CNCC dysfunction was mimicked by CNCC ablation. Sufficient evidence has shown that CNCCs themselves play a critical role in great vessel remodeling and some evidence suggested that CNCCs may contribute to valve development [5, 34, 258]. As suggested by the results of this study together with some previous findings, CNCC ablation leads to abnormal cardiac cushion development and abnormal hemodynamics at a time point before CNCCs physically reach the heart. Cardiac cushions, as valve progenitors, are directly associated with normal/abnormal valve development while abnormal hemodynamics at the outflow tract possibly contribute to conotruncal defects [43, 281, 292, 293]. Abnormal cardiac cushion development and abnormal hemodynamics potentially influence each other and form a feedback loop. This abnormal feedback between cardiac function and cardiac cushions may impact the overall development of the heart and lead to a spectrum of defects. Although not shown in the chart for simplicity, any steps in this chart likely involve gene expression alterations.

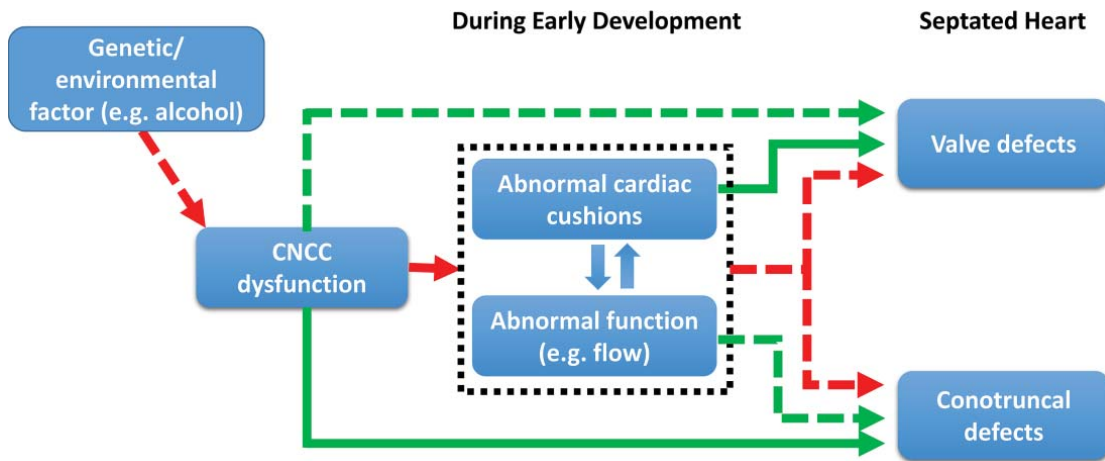


**Fig. 5.12** Proposed role of cardiac functions for CNCC-related CHDs. CNCC dysfunction causes abnormal early cardiac structures and functions, which compose a feedback loop (black dashed-line box) that may contribute significantly to late stage CHDs. Green solid arrows: previously established links with solid experimental supports. Green dashed arrow: previously suggested links with limited experimental supports. Red solid arrow: links established in this study. Red dashed arrows: suggested links in this study.

In conclusion, we have quantitatively phenotyped the great vessels and left AV valvular defects in a CNCC-ablation model, which have not been reported previously. Abnormal early cardiac function and structure, including abnormal flow patterns and cardiac cushion formation were investigated as a potential mechanism for valve defects. Similar defective phenotypes are observed in avian models of both alcohol exposure and CNCC-ablation, measured at both looping and four-chambered stages. This supports the hypothesis that CNCCs play a role in alcohol-induced CHDs. In the future, to further investigate the association between early abnormalities and late stage defects, we will make use of non-invasive OCT imaging to longitudinally follow the cardiac function and structure of CNCC-ablated embryos. Better optical clearing techniques will facilitate the imaging of even older hearts and allow us to make measurements on more mature valves and great vessels. It may become possible to image the heart intact for diagnosing distal great vessel defects such as coarctation of the aorta and measuring the length of great vessels. We will

also investigate even earlier, more detailed aspects of cardiac function such as absolute blood flow and shear stress at the pharyngeal arches, which are specific CNCC migration sites [161, 173, 294]. These early functions may serve as reliable predictors of later developmental defects, potentially enabling rapid screening methods for studies of rescue/prevention interventions.

## **Chapter 6. Summary and future work**

### **6.1 Summary**

There are numerous unanswered questions regarding the pathological process of congenital heart defects (CHD). Linking the developmental cardiac structure, function, biomechanical forces, conduction and gene expression is especially important in answering those questions. Optical mapping (OM), the current imaging method for embryonic cardiac conduction, has drawbacks that limits its use in the investigation of the developmental cardiac conduction system. This dissertation focuses on improving OM technology by taking advantages of other emerging modalities, including optical coherence tomography (OCT) and light-sheet fluorescence microscopy. The improvements accomplished in this dissertation will greatly benefit the investigation of the embryonic conduction system and the etiology of CHDs.

In chapter 1, CHD, CHD models, cardiac conduction system were reviewed and the gaps in our understanding were discussed. Improved imaging technology can be the key in answering some of the remaining questions. As a standard modality for measuring electrophysiology, OM was reviewed and its limitations were put forward. OCT and light-sheet fluorescence microscopy were introduced as promising technologies that may facilitate OM in providing better electrophysiological measurements. The major limitations of current OM technology are its 2D imaging property, incomplete information from a conventional imaging session and the requirement for drugs to uncouple heart motion. These issues were addressed in the following chapters.

The first step was to correct biased conduction velocity measurements. Chapter 2 described an integrated OM and OCT system and an algorithm for the correction of

conduction velocity. The system setup was described and experiments of three hearts were demonstrated. OCT images provided 3D structural imaging of the hearts and the datasets were segmented to generate height maps, which were used in correcting velocity from 2D to 3D. The correction amount is determined by the 3D slope of the local region along the conduction direction. Conduction velocity and the resulted correction amount were mapped to high resolution images. In two of the three hearts, about 40% of the pixels needed a significant correction. This 3D correction eliminated underestimation bias in 2D conduction velocity measurements therefore enabling more accurate measurements with less experimental variability.

After mapping 2D OM images to 3D surface of the heart, it became more obvious that traditional OM can only efficiently image a small portion of the heart ( $\sim 1/3$ ). Therefore a further step was taken to acquire complete, orientation-independent, full 3D electrophysiology information. The approach of achieving this goal was combining light-sheet fluorescence microscopy with OM. In chapter 3, the design and alignment of a custom built light-sheet microscopy system were described in detail. The light-sheet system used a cylindrical lens to generate a light sheet for illumination and adopted an ETL in the detection path in order to achieve fast scanning and eliminate the need of moving the sample. We have successfully demonstrated the feasibility of acquiring 4D OM images with this light-sheet system. 4D membrane potentials were presented in figures and movies. With 4D dataset, activation sequence of any 2D plane can be resampled and analyzed. This can be extremely useful when a specific cross section of the sample is interested in a study. Abnormal samples often have altered morphology. The complete, orientation-independent datasets will be ideal for comparisons between normal and abnormal samples.

The use of EC-uncouplers significantly influences the health of embryonic hearts and makes OM imaging a terminal process. Chapter 4 introduced an attempt to overcome this limitation through correcting heart motion in post processing instead of applying EC-uncouplers to the heart during imaging. The motion correction approach was based on a B-spline nonrigid image registration algorithm. To register hundreds of frames to a single steady state, several approaches were tested. It was demonstrated that a two-step key-frame registration method provided the best results. This correction recovered the upstroke of the action potential to some extent. The activation maps calculated from recordings after motion correction with key-frame method and the recordings from heart motion suppressed with CytoD were similar. Conduction velocities in the ventricle and outflow tract region were also comparable. This method based on 2D OM image showed promises in correcting the majority of in plane motion, yet the contraction of the heart is 3D and the out of plane motion made it impossible to fully recover the recording to a motion-free situation.

The ultimate goal of developmental cardiovascular research is to understand and even prevent CHDs. Models that consistently result in defects that resemble CHDs in human are critical in achieving the goal. A cardiac neural crest cell (CNCC) ablation model was developed and described in chapter 5. CNCC-ablation mimics features of DiGeorge syndrome and causes a series of outflow tract defects in the heart. It is likely involved in the mechanism of alcohol-induced heart defects. A laser ablation method was described, and detailed quantitative phenotyping of CNCC ablation-related CHDs and abnormal early cardiac structures and functions were reported. OCT was used to assay both early and late-stage embryos and hearts. Quantitative analysis revealed that at later septated-heart stages, CNCC-ablated embryos have reduced great vessel diameter and reduced left

atrioventricular valve leaflet volumes compared to the control embryos. At earlier cardiac looping stages, CNCC-ablated embryos exhibited abnormally twisted bodies, abnormal blood flow waveforms, increased retrograde blood flow percentage, and abnormal cardiac cushion formation. These early stage abnormalities can be contributing factors for the late-stage CHDs. We have also observed striking similarities between the range of phenotypes found in the CNCC-ablation model and those found in an established avian fetal alcohol syndrome model. The CNCC-ablation model was previously reported to have conduction system defects. The technology improvement made in the earlier chapters will facilitate the investigation of abnormal conduction in the CNCC and the fetal alcohol syndrome CHD models, as well as validating rescue models in the future.

## **6.2 Future work**

The work in this dissertation builds the foundation for a large body of further development and experiments. Future work with the highest priority will be discussed in this section.

### *6.2.1 4D OM in beating embryonic heart and in vivo OM*

Using image registration method for the correction of cardiac motion is limited to 2D and the results were not entirely satisfactory. This is because heartbeat motion is in 3D and the out of plane motion causes the object to be in and out of focus therefore changes the point spread function at each depth layer, and is then reflected as intensity changes in the image. Correcting motion in 3D, although may require more complicated algorithms, can be advantageous over that in 2D because the out of plane motion can be captured in 3D and may be more accurately corrected. Here I propose several approaches, which should be tested out one by one, from the simplest to the most complicated.

The first approach uses the light-sheet OM system itself. Embryonic hearts will be prepared using the normal OM procedure except for the EC-uncoupler. Without using the EC-uncoupler, the heart can be paced for a much longer period of time and therefore it can be more densely sampled at  $z$  direction during data acquisition (i.e. more slices). This ensures signals from all pixels to be captured in adjacent slices while the heart is beating. 2D-over-time light-sheet OM data of beating hearts will be collected and rearranged to 4D datasets based on the accurate gating timing achieved with optical pacing. Electrical activity causes signal intensity to change, which can potentially confound with signal changes due to motion. However, because membrane potentials are from the myocardium, theoretically tracking surface motion of the heart should be adequate for correcting fluorescence traces. A general threshold will be applied to the images for identifying the myocardium. 3D image registration will be used to track pixel displacement through a complete heart cycle. The registration of the 3D time series volumes may adopt either a single-reference or key-frame methods, as described in Chapter 4 for 2D images. This will result in 4D membrane potentials on a “static” heart, with which measurements such as activation time and conduction velocity can be made. Alternatively, algorithms may be developed to directly identify and track the conduction wave using the 4D data of beating hearts without achieving the “static” mode. For example, velocity vectors calculated from the 4D datasets with motion are the combination of the conduction velocity vector and motion velocity vector. Motion velocity should be a smaller contribution compared to conduction velocity. By tracking motion and extract a motion velocity vector at each pixel, the conduction velocity vector can be calculated by subtracting the motion velocity vector from the total velocity vector. Note that pixel tracking through imaging registration or other

image similarity-based methods gives an estimation and may not be the ground truth of the physical displacement of cells in contraction. If this estimation of displacement is not satisfactory, fiducial markers on the heart may be necessary to characterize the true motion of the contracting heart.

It is possible that motion tracking and correction on threshold images may not be satisfactory. Therefore I proposed a second approach, which uses another set of images that do not have voltage signal responses to facilitate motion tracking. This idea is similar to the 2D ratiometric imaging [99, 101]. Candidates include another fluorescence imaging using another dye and OCT. Using fluorescence imaging requires modification of the detection path. The additional setup includes a dichroic mirror, appropriate optics and a second fast camera. The FOV of the two cameras should be calibrated and well-aligned. The second dye should not have effect on the conduction system, interfere with the voltage-sensitive dye or affect the health of the heart significantly. Two cameras will be synchronized and collect data simultaneously. Once both datasets are acquired, 4D data from the second camera will be used to track motion (similarly to the first approach described in the last paragraph) and corresponding pixels in 4D data from the voltage sensing camera will be traced back using the trajectory found by the second camera. The advantage of using a second fluorescence channel is the ease of matching pixels from two cameras while the disadvantage is the need for a second stain on the hearts. An alternative imaging modality is high-speed OCT. With gating technologies or the recently available ultra-high-speed swept light source, 4D myocardium contraction pattern of the embryonic heart can be acquired by OCT with sufficient spatial and temporal resolution. The OCT sample arm can be compact and portable. Therefore it is effortless to be integrated to the

existing light-sheet system. Sample preparation follows the normal light-sheet OM procedure. The acquisition of 4D OCT datasets will be simultaneous with 4D OM. The contraction pattern will be used to track both in plane motion and out of plane motion for each corresponding slice in the 4D OM dataset. The tracking results will then be used to correct motion in 4D OM. This approach does not require a second staining on the heart, yet it adds a step of registering 3D volumetric images from two different imaging modalities, which is computationally expensive and can potentially cause errors.

The ultimate goal is *in vivo* and longitudinal OM, although it requires overcoming several challenges. The first issue lies in the dye. Voltage-sensitive dyes are phototoxic to some degree depends on the type of the dye. Compared to 5 to 10-minute survival for a quail embryonic heart sample with both dye staining and the EC-uncouplers, a heart may survive for half an hour with exposure restricted to the dye staining. Yet it is still a short time compare to the days of developmental process that we are interested in. Even if a dye with minimum phototoxicity is developed, it faces another problem that it may not be efficiently delivered to the heart tissues due to the two layers of membranes wrapping the embryo and the heart. The ideal solution to both issues with the dye is to make genetically encoded voltage indicators (GEVI) available in avian species. Several generations of GEVIs have been developed and used in neurological studies [52, 61, 70, 295]. In 2014, *in vivo* OM of embryonic zebrafish heart was demonstrated with one of the GEVIs, Arch(D95N) [110]. This generation of Arch has a response time in 1-40 millisecond range. A newer Arch-based GEVI QuasArs has improved speed and sensitivity, however, it has not been available in the heart of any species [61].

*In vivo* OM will also require system redesign. The current light-sheet microscopy system illuminates the sample from the side and detect signals from another side. An embryo in culture is kept horizontally and the heart is only accessible from above. Therefore, either a setup in which both illumination and detection optics access the sample from the top or an oblique, single objective lens light-sheet system needs to be implemented. Both forms of light-sheet system have been demonstrated previously [196, 197, 201, 202]. Either solution is approachable, but involves significant modifications to the current system.

#### *6.2.2 Software toolbox for 4D membrane potentials*

Visualization of membrane potentials in 4D is exciting and important. However, phenotyping, characterization and comparison often are not satisfactory without quantification. Our group has established a software toolbox for conventional 2D OM images. As the development of 4D OM with the light-sheet system, the current software became inadequate. Therefore, software optimized for 4D OM will be implemented. Algorithms for computing important electrophysiological parameters will be developed. These parameters include activation time, action potential duration, upstroke velocity and conduction velocity. The first three parameters are related to single action potential traces and the algorithms for calculating them can be mostly inherited from previous software toolbox. The conduction velocity calculation has a drastic change from 2D to 3D. Conduction of electrical activity follows the heart surface in a 3D space, but because the heart only has two cell layers at early stages, conduction is therefore still confined within a thin layer. A fitting algorithm that takes this conduction property into consideration will be developed. The fitting will be within a kernel that can adaptively change its size based on the conduction velocity. Conduction direction will be within the surface of the kernel,

*i.e.* perpendicular to the normal of the kernel. Moreover, the software should require minimum input from users so that high throughput data can be analyzed automatically. Because 4D datasets are often large in size and requires substantial computational power, we will consider implementing graphics processing unit (GPU) for the processing.

### *6.2.3 Link 4D conduction maps with cardiac structures and gene expression*

The feedback loop of structure, hemodynamics, biomechanical forces, conduction and gene expression continuously takes place during cardiogenesis. None of these factors should be investigated in isolation. Fortunately our group has access to several different imaging systems, with which we can map most of these parameters in the developing hearts. For example, OCT is capable of characterizing structure, hemodynamics and biomechanical forces. Light-sheet fluorescence microscope is well-suited for a variety of staining experiments, besides offering 4D conduction maps.

The initial experiments will be quantitatively phenotyping normal embryos and establishing protocols for high-throughput screening. Then CHD models, specifically the fetal alcohol syndrome model and the CNCC-ablation model, will be investigated. Because the looping stages of heart development is an important time period and is the range of stages we are familiar with, the looping stages will be the first target. Topics that will be first explored are excitation-contraction coupling, full conduction velocity-cardiac cushion thickness correlation maps, distribution of the three connexins (Cx40, Cx43, Cx45), etc. Here I propose a series of experiments enabled by the tools developed in this dissertation:

- 1) Quantitatively phenotype 4D cardiac membrane potentials in a series of stages of normal quail embryos (start from HH stage 10). Identify important transitions in conduction system development.

- 2) Quantitatively phenotype 4D cardiac membrane potentials in FAS and CNCC-ablated quail embryos.
- 3) Characterize conduction patterns in a series of stages of mouse embryos. Collect OM data from mouse embryonic hearts (E10.5) with and without motion. Explain the contradictory conduction results for looping stage mouse embryos.
- 4) Integrated 3D conduction velocity and cardiac cushion thickness mapping in normal embryos, FAS embryos and CNCC-ablated embryos.
- 5) Integrated 3D conduction velocity and connexins mapping.
- 6) Integrated conduction and contractile wave mapping. Measurement of EC delay.
- 7) Integrated *in vivo* OM and shear stress mapping.

## **Appendix A Movie Description**

**Movie 2.1** 4D transmembrane potentials of looping stage embryonic heart and 2D transmembrane potentials in three orthogonal planes. Colored activation wave is overlaid on grayscale heart tube volume reconstruction or cross sectional images. A: 4D transmembrane potentials and the locations of the three orthogonal planes. B: transmembrane potentials at an xy-plane. C: transmembrane potentials an xz-plane at corresponding time points. D: transmembrane potentials at a yz-plane.

**Movie 2.2** 4D transmembrane potentials of a looping stage embryonic heart.

**Movie 2.3** 3D activation map of a looping stage embryonic heart.

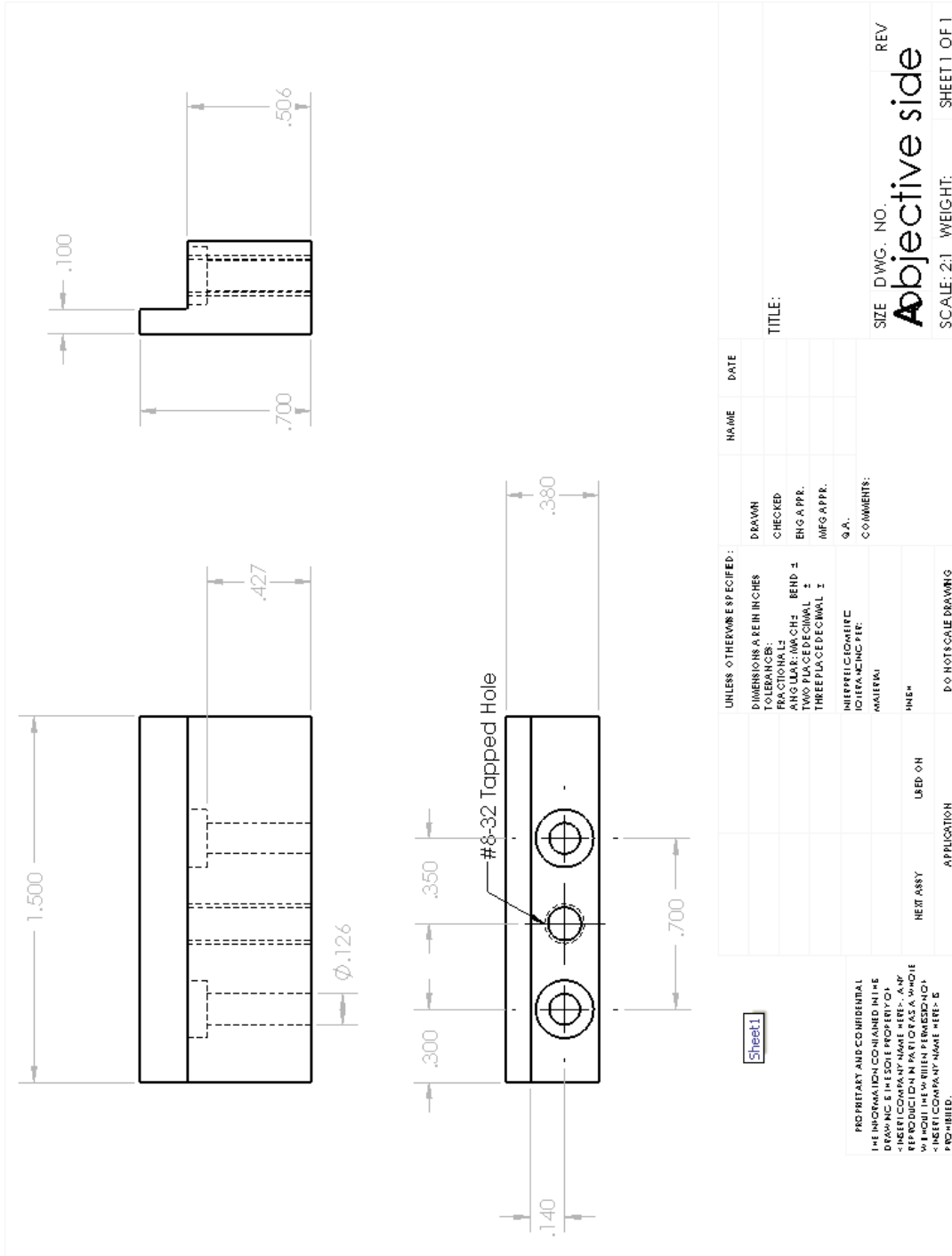
**Movie 4.1** OM fluorescence images before and after motion correction.

## Appendix B Compact OCT scanner Part List

<b>Part No.</b>	<b>Vendor</b>	<b>Quantity</b>	<b>notation</b>
A397TM-C	Thorlabs	2	collimating lens
SM1Z	Thorlabs	1	
KB1F	Thorlabs	3	removable mounts (magnetic)
KB1P	Thorlabs	1	removable mounts (magnetic)
S1TM09	Thorlabs	1	
SM1L10	Thorlabs	1	cut at the machine shop to fit for set 1
KC1-T	Thorlabs	3	
CP06	Thorlabs	1	
LA1608C	Thorlabs	1	objective set 1
AC254035C	Thorlabs	1	objective set 1
AC254030C	Thorlabs	2	objective set 2
AC254045C	Thorlabs	1	objective set 3
AC254060C	Thorlabs	1	objective set 4
PT1	Thorlabs		stage for reference arm
PF10-03-M01	Thorlabs	1	mirror for reference arm
stage1	custom	1	drawing attached
stage2	custom	1	drawing attached
stage3	custom	1	drawing attached



Part drawing for stage 2 (objective stage)



Sheet 1

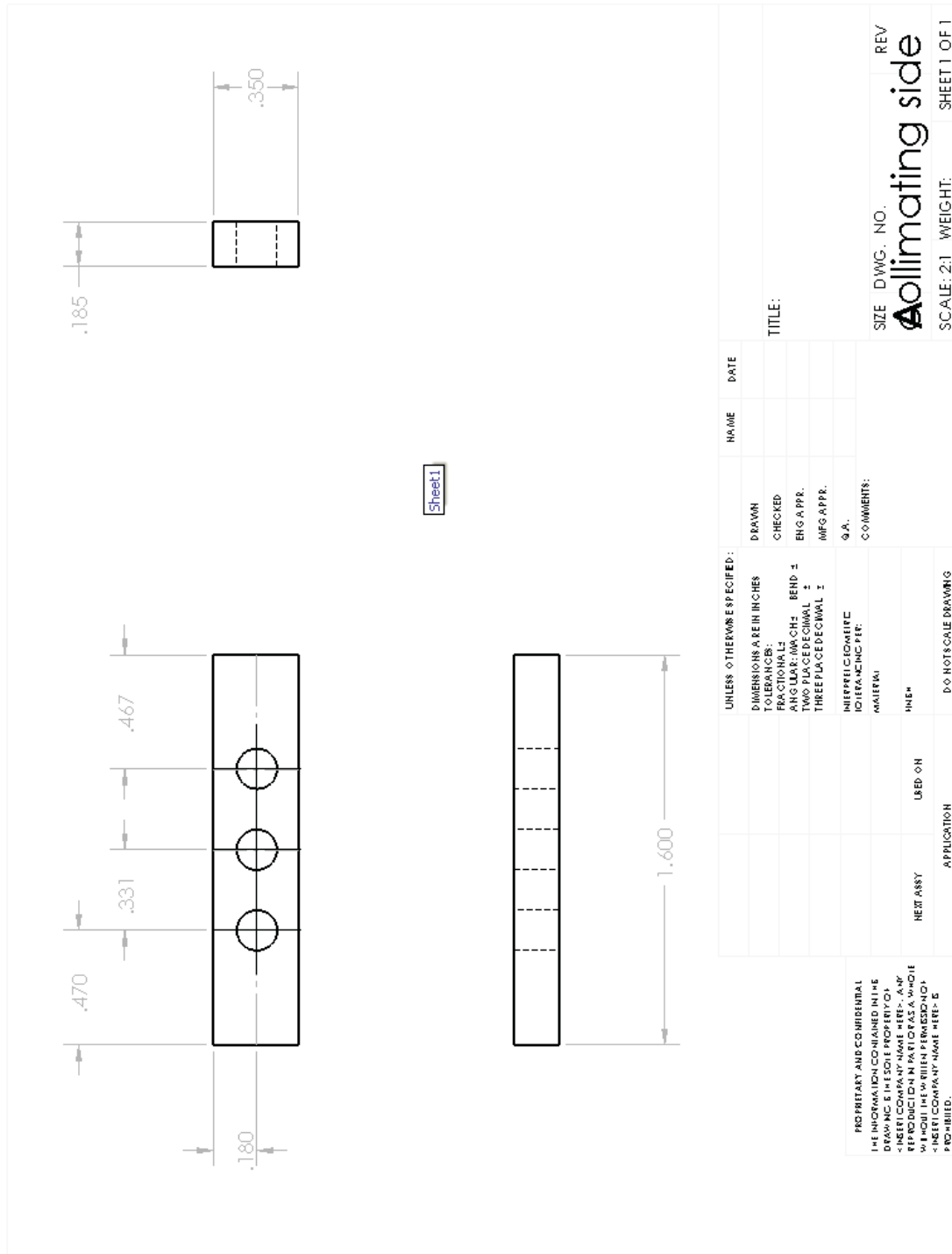
PROPRIETARY AND CONFIDENTIAL  
 THE INFORMATION CONTAINED IN THIS  
 DRAWING IS THE SOLE PROPERTY OF  
 INERT COMPANY NAME HERE. A RE-  
 PRODUCTION IN ANY FORM OR BY  
 ANY MEANS WITHOUT THE WRITTEN  
 PERMISSION OF INERT COMPANY  
 NAME HERE IS  
 PROHIBITED.

UNLESS OTHERWISE SPECIFIED:	NAME	DATE
DIMENSIONS ARE IN INCHES		
FRACTIONS	DRAWN	
ANGULAR DIMENSIONS	CHECKED	
TWO PLACE DECIMAL	ENG APPR.	
THREE PLACE DECIMAL	MFG APPR.	
Q.A.		
INTERPREL DIMENSIONS	COMMENTS:	
ISO/FIN/UNC PTF		
MM/ITERM		
INCH		
NEXT ASSY	USED ON	
APPLICATION		
DO NOT SCALE DRAWING		

SIZE DWG. NO. REV  
**Objective side**  
 SCALE: 2:1 WEIGHT: SHEET 1 OF 1

5 4 3 2 1

Part drawing for stage 3 (collimation stage)



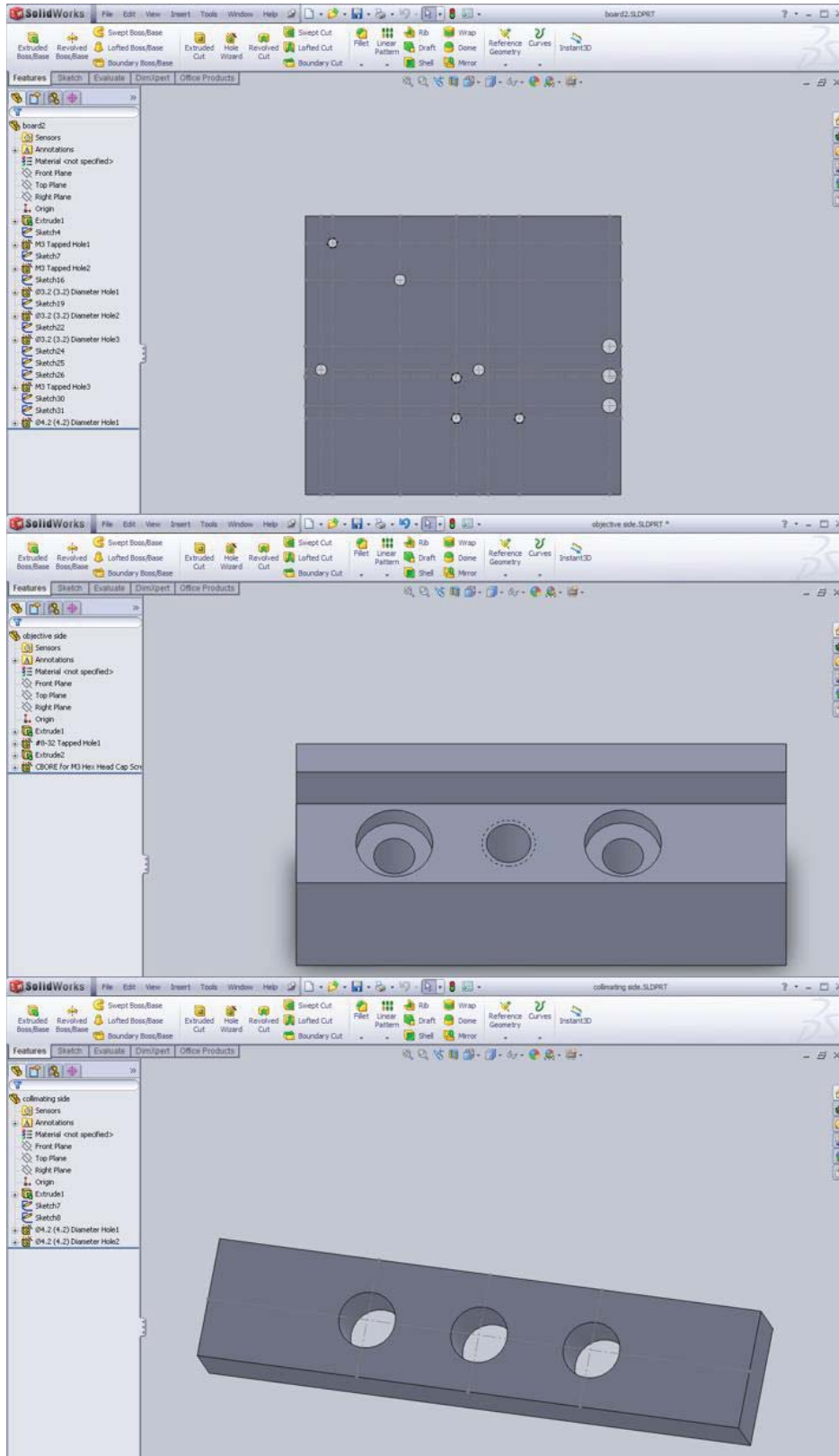
Sheet 1

UNLESS OTHERWISE SPECIFIED:		NAME	DATE
DIMENSIONS & REIN INCHES	DRAWN		
TOLERANCES:	CHECKED		
FRACTIONAL:	ENG APPR.		
ANGULAR: MACH: BEND: ±	MFG APPR.		
TWO PLACE DECIMAL: ±	Q.A.		
THREE PLACE DECIMAL: ±	COMMENTS:		
INTERFEROMETRIC			
IDENTIFYING REF:			
MATERIAL:			
FINISH:			
USED ON:			
APPLICATION:			
DO NOT SCALE DRAWING			

PROPRIETARY AND CONFIDENTIAL	SIZE	DWG. NO.	REV
THE INFORMATION CONTAINED IN THIS	<b>Collimating side</b>		
DRAWING IS THE SOLE PROPERTY OF	SCALE: 2:1	WEIGHT:	SHEET 1 OF 1
<INSERT COMPANY NAME HERE>. ALL			
RIGHTS RESERVED. NO REPRODUCTION			
OR TRANSMISSION IN ANY FORM OR BY			
ANY MEANS, ELECTRONIC OR MECHANICAL,			
INCLUDING PHOTOCOPYING, RECORDING,			
OR BY ANY INFORMATION STORAGE AND			
RETRIEVAL SYSTEM, WITHOUT PERMISSION			
IN WRITING FROM THE COMPANY IS			
PROHIBITED.			

### 3D SolidWorks model of stages 1, 2, and 3



## Appendix C Integrated OCT and OM Image Processing using MATLAB

System setup information is in Chapter 2. Experimental procedure should follow the OM protocol. An OCT volume of the heart should be collected simultaneously or immediately after OM data acquisition.

All code files are located under codes/Pei/OCT\_OM\_static, unless otherwise notified.

Main function: OCTOMstatic

- 1) Loading OCT (volume) and OM (2D-over-time image series) datasets respectively
- 2) Cut OCT data to limit the size of the volume for fast processing
- 3) Correct aspect ratio for OCT volume images. Call function “*correct\_interpolation*”
- 4) Correct imaging angle for OCT volume images based on the image of glass chamber, which is a straight line in image. Call function “*correct\_orientation*”
- 5) Create *en face* projection image from the OCT volume. Call function “*OCTvolume\_projection*”
- 6) Image registration between OCT projection image and an OM image. Call function “*image\_registration*” (this function is in the image registration folder)
- 7) Transform the OCT volume according to the registration transformation matrix to match the OM data. Call function “*affine\_transform*” (this function is in the image registration folder)
- 8) Segmentation of the heart from the OCT volume. This step is performed using Amira. In the segmentation panel, use threshold to roughly segment the heart and then manually modify to perfect the segmentation.
- 9) Create OCT surface mask using the segmentation result acquired from the last step. Generate an OCT height map.

- 10) Generate 2D activation map and 3D corrected conduction velocity map. Call function “*yOMcurvefit*” (this function is under the MATLAB code folder). Feed in OCT height map as a parameter to this program.
- 11) Project 2D activation time map and conduction velocity map onto the 3D surface mask created in step 9). Call function “*iso\_onthreed*”

## Appendix D Light-sheet Microscopy System Part List

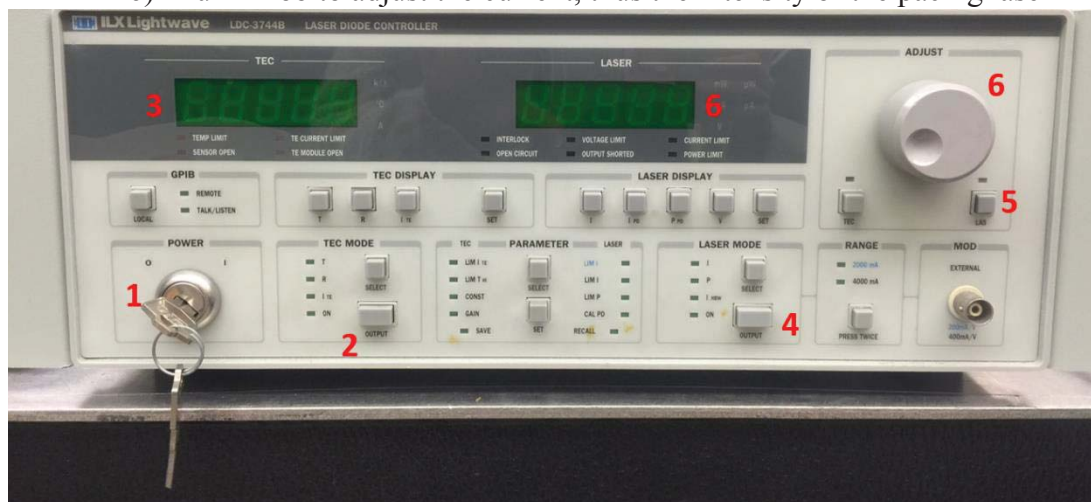
component of system	Part No.	Vendor	Quantity	notation
Illumination	Stradus® 505 - 70	Vortran	1	505 nm light source
	ET500/20x	Chroma	1	light source clean up filter
	LA1255-A	Thorlabs	2	spatial beam filter
	P50S	Thorlabs	1	
	CXY1	Thorlabs	1	
	CP02	Thorlabs	2	
	6210H set, 3mm	Cambridge Technologies	1	Galvo
	LA1951-A	Thorlabs	1	beam expander
	LA1708-A	Thorlabs	1	
	LJ1695RM-A	Thorlabs	1	cylindrical lens
Detection	Objective Fluor 5x/0.25	Zeiss	1	objective
	C-Apochromat 10x/0.45 W M27	Zeiss	1	objective
	SM1A17	Thorlabs	1	objective adaptor
	PT1	Thorlabs	1	objective translating mount
	ET535/30m	Chroma	1	emission filter
	QRC1A	Thorlabs	2	emission filter mount
	LA1608-A	Thorlabs	1	tube lens
	LBF254-200-A	Thorlabs	1	tube lens
	LA1509-A	Thorlabs	2	relay lens
	EL-10-30-C-VIS-LD-MV	pacer	1	ETL
	EL-E-4	pacer	1	ETL driver
	CM1-P01	Thorlabs	2	mirror cube
	CXY1	Thorlabs	1	ETL mount
	SM1A10	Thorlabs	1	ETL adaptor
	iXon Ultra 897	Andor	1	high speed camera
optomask	Andor	1		
	PT3	Thorlabs	1	sample translational stage
Optomechanical mounting parts	XT66-1000	Thorlabs	1	
	XT66P2	Thorlabs	3	
	MB8	Thorlabs	2	

post	Thorlabs	many, various length	
post holder	Thorlabs	many, various length	
rods	Thorlabs	many, various length	
BA1	Thorlabs	many	
KM100T	Thorlabs	2	
CP02	Thorlabs	many	

## Appendix E Light-sheet OM Protocol

### A day before experiment

1. Make sure the light-sheet system is in working condition using a polymer phantom (calibration reports located under /light-sheet OM/system/calibration).
2. Make sure the pacing laser (Qphotonics, QFLD-1465-400S) is in working condition. A simple test: turn the laser diode controller to 140 mA, the output power from the laser should be around 35 mW. If not, use the IR card to check the light spot from the pigtail fiber.
  - a) Diode controller for the pacing laser
    - 1) Turn key
    - 2) Push the TEC output
    - 3) Make sure the TEC display says 25 degrees
    - 4) Turn on laser mode output
    - 5) Push to enable adjustment of laser power
    - 6) Turn knob to adjust the current, thus the intensity of the pacing laser

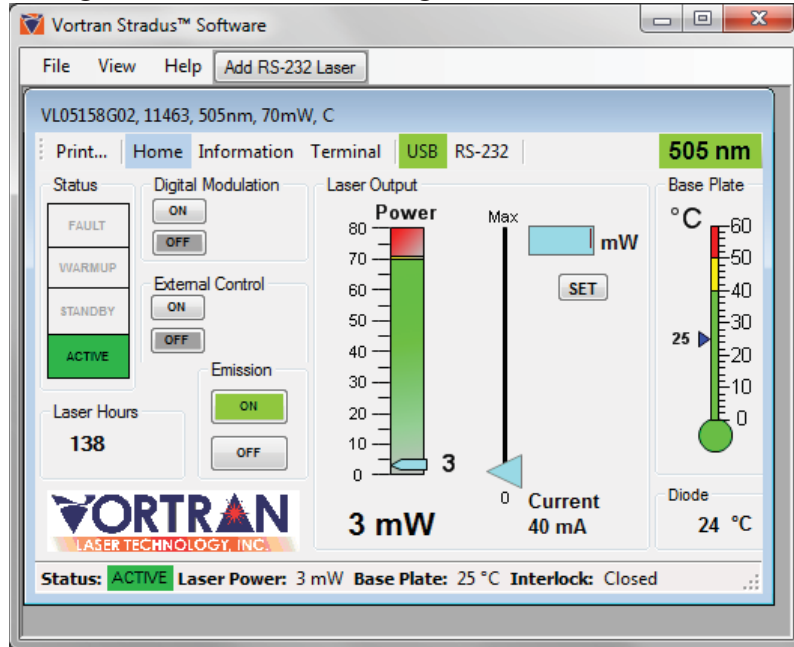


3. Setup pacing components. Use a proper stage to hold the micromanipulator.

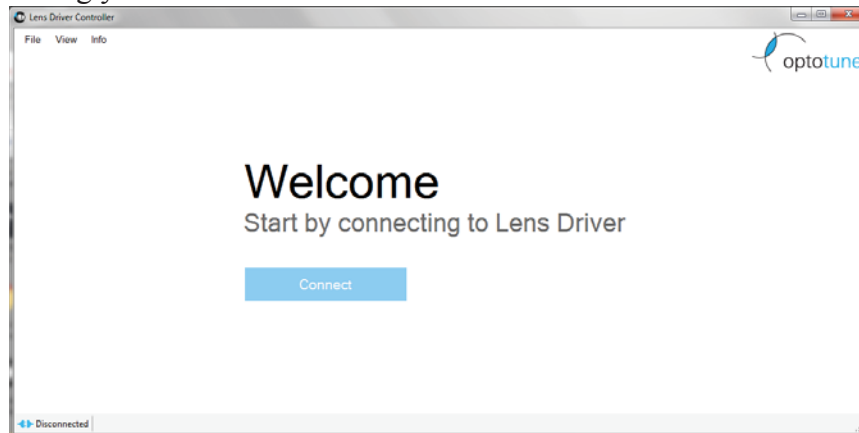
### Before experiment

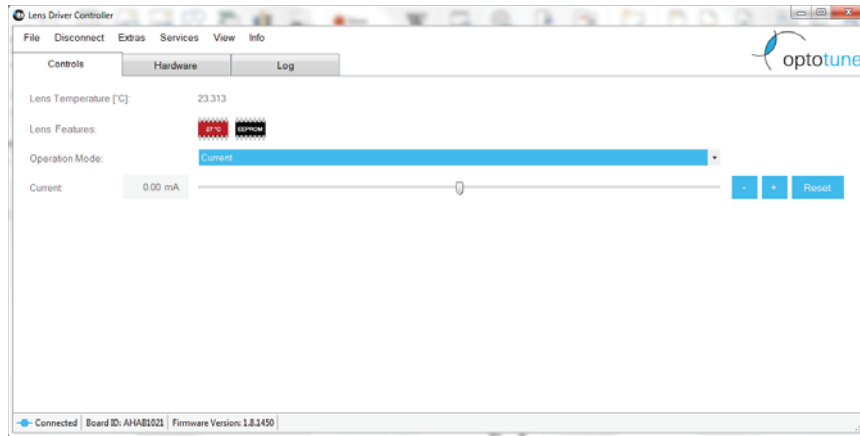
4. Aliquot Tyrode's solution (fridge) into a dish and return the bottle to the fridge
5. Take FluoVolt and PowerLoad (both fridge and should be kept in one bag) and make staining solution. Dilute FluoVolt 1000 times and PowerLoad 100 times (1  $\mu$ l FluoVolt and 10  $\mu$ l PowerLoad per 1 ml Tyrode's solution). Staining solution should be mix in a black tube. Shake to mix well.
6. Float optical table
7. Turn on the power of the Galvo (under the optical table).
8. Take out CytoD from the freezer of motion suppression is desired.
9. Turn on the light-sheet system:

- a) Turn on the 505nm laser (Vortran). Push down the power switch, then turn key.
- b) Connect the ETL driver to the computer through its USB cable.
- c) Turn on the power button of the camera (Andor)
- d) Turn on the 505nm laser controlling software (Vortran Stradus Software). Output power can be adjusted through the input box. During aligning and testing, 1-3 mW should be enough.

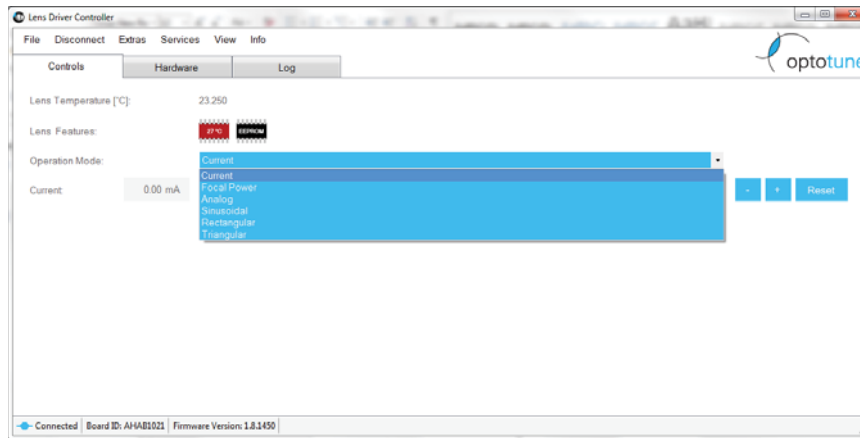


- e) Turn on the ETL controlling software (Lens Driver Controller). Click “connect”. If the software cannot find the ETL, a dialog box will pop up asking you to install the driver.

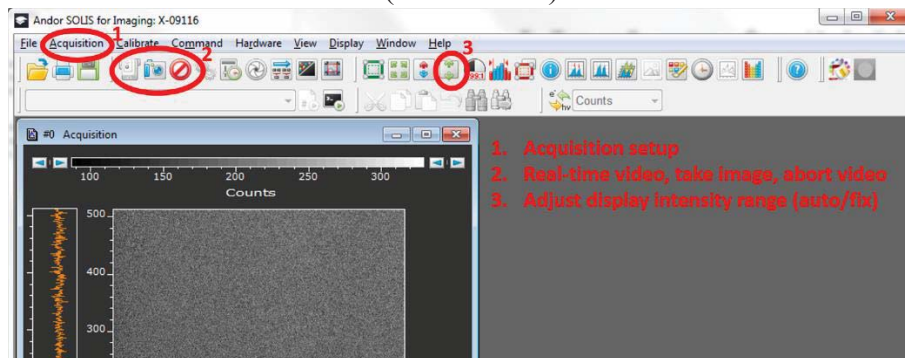




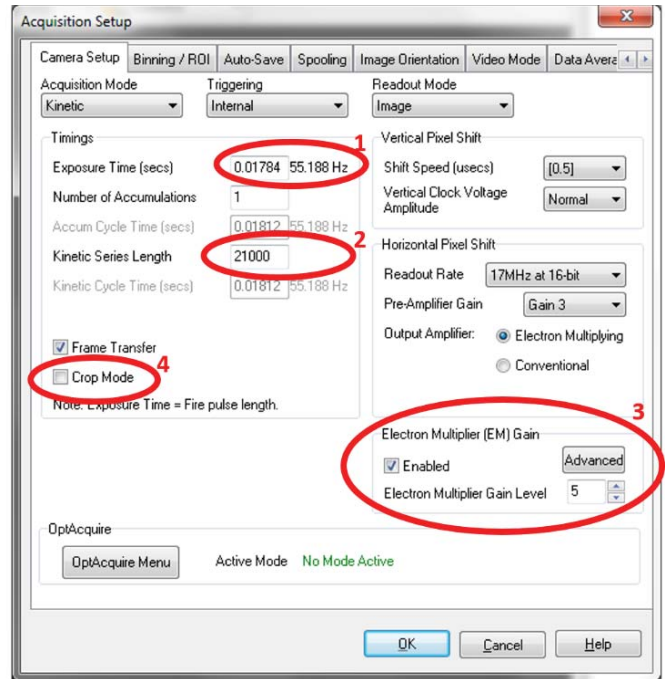
For light-sheet experiment, select “analog” from the dropdown menu.



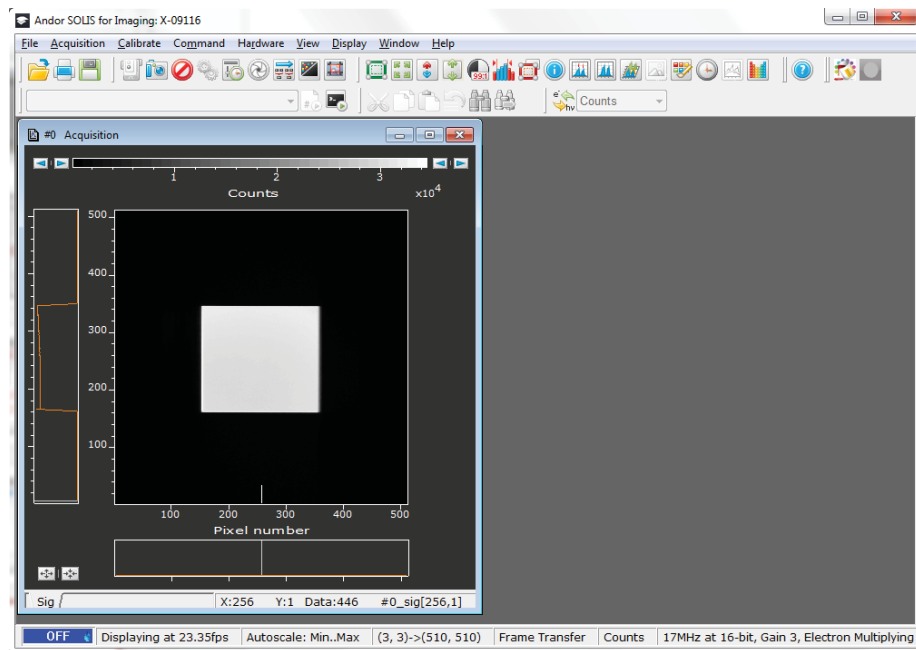
f) Turn on the camera software (Andor Solis).



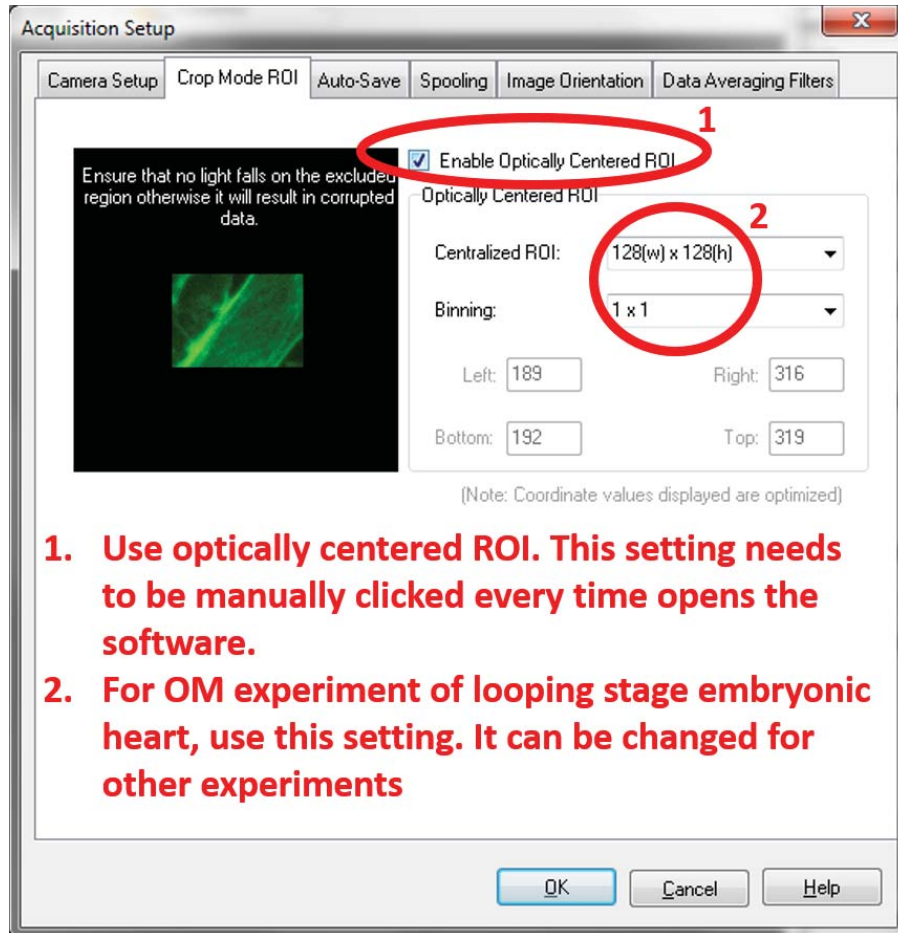
1. Setup frame rate using proper "exposure time"
2. Setup total number of frames using "kinetic series length"
3. Set some EM gain to further reduce read noise. This is useful when you have relatively low light. This will sacrifice some dynamic range
4. The camera works under "crop mode" for voltage imaging.



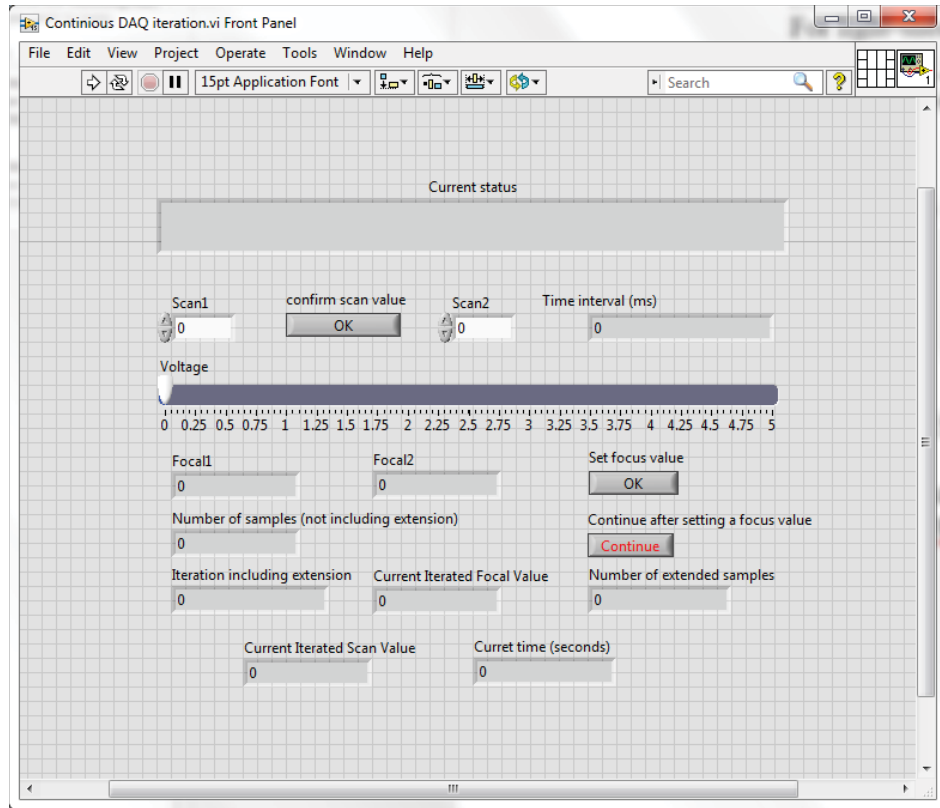
Crop mode is used when imaging fast voltage signals. Use the optomask to mask out pixels to leave desired field of view (usually 128\*128)



In "crop mode ROI", select proper settings

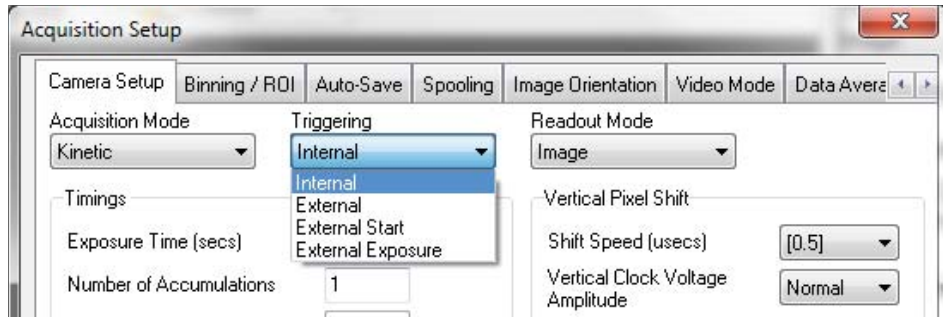


g) Turn on LabView program “Continuous DAQ iteration”

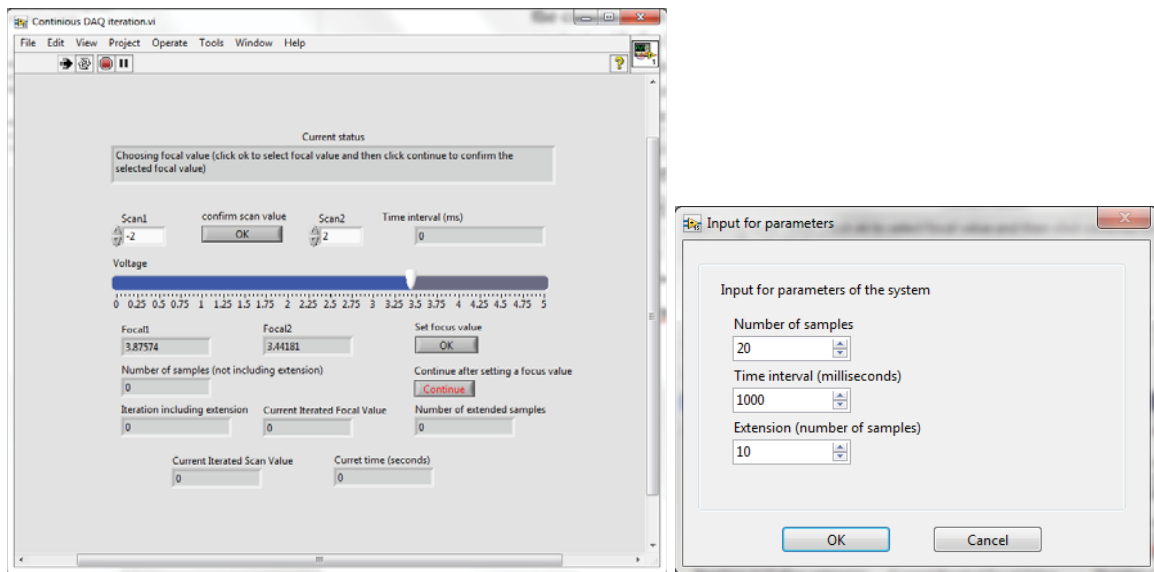


## During experiment

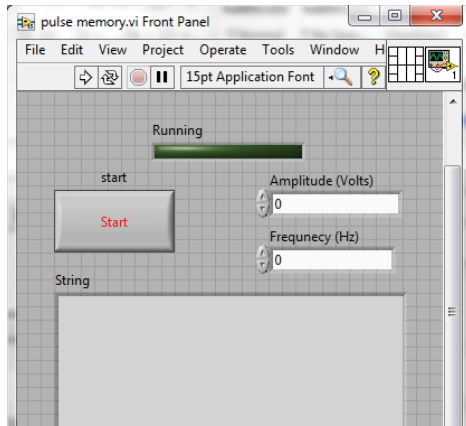
10. Excise a heart
11. In the dark under red light, use a glass transfer pipette to place the heart into 300  $\mu\text{l}$  staining solution. Use a cap to cover the heart. Stain for 20 min. Lights can be turned on during the staining waiting time.
12. Put 1 ml Tyrode's solution into a cuvette. Put 1.2  $\mu\text{l}$  CytoD into the cuvette if motion suppression is desired.
13. After the staining time, turn off lights. In the dark under red light, transfer the heart using the glass pipette from the staining solution to the cuvette. Make sure the heart drops to the middle of the cuvette.
14. Use the LabView program to set the scanning to 0 (Galvo centered)
15. Open the shutter for the 505nm laser. Set laser output power at some value between 5-10 mW. Place the cuvette so that the light sheet goes through the heart.
16. Turn on real-time video. Use the correct fluorescence filter. Find the heart, move it in x and y dimensions to place the heart in proper field of view.
17. Turn off the 505nm laser, turn on the red light. Remove fluorescence filter. With the help of the camera video, introduce the pacing fiber to the cuvette, gently locate the fiber in contact with the heart, at the atria region.
18. In camera acquisition setting, select "external start" as the triggering mode. Back to the main panel of the camera and click the "take image" button. (the camera will then wait for a trigger to start imaging)



- Turn on the 505nm laser and set the output power to 10 mW. Use the LabView program, manually set two focusing planes. Then in the pop up window, set the number of slices wanted between the two preset focusing planes, the imaging time at each plane and the number of extended slices desired. The time interval should be determined by the pacing frequency and the number of heartbeat at each slice. For example if the heart is paced at 1Hz and one heartbeat is wanted at each slice, then the time interval should be 1000 ms. In the camera setting, the number of total frames should be calculated to match your data acquisition settings.



- Before clicking “ok”, turn on the pacing laser by turning on the laser diode controller. Start pacing (either by a function generator or by a LabView program).



21. Turn up the 505nm laser power to be 70 mW.
22. Click “ok” in the popup window in step 10.
23. Save data at a desired location after data acquisition is completed. Make sure the entire series is saved. This may take a while.
24. Turn off the 505nm laser. Turn off the pacing laser.
25. Once all data is acquired, light may be turned back on.
26. Dump the contents of the cuvette into the sink and rinse with dH<sub>2</sub>O. The cuvette may be reused.

**After experiment:**

27. Discard dish or tube used for staining in regular trash.
28. Discard tissue or eggs contents into a red biohazards bag.
29. Clean up egg area and zip the red biohazards bag.
30. Clean all dissection tools. Return pipette and dissection tool to their original location.
31. Dump remaining Tyrode’s solution.
32. Unfloat the table.
33. Turn off the camera.
34. Turn off the ETL.
35. Turn off the 505nm laser power and close the shutter.
36. Turn off the pacing laser and pacing laser diode controller.
37. Turn off the Galvo.

## Bibliography

1. van der Linde, D., et al., *Birth prevalence of congenital heart disease worldwide: a systematic review and meta-analysis*. Journal of the American College of Cardiology, 2011. **58**(21): p. 2241-2247.
2. Marelli, A.J., et al., *Lifetime Prevalence of Congenital Heart Disease in the General Population from 2000 to 2010*. Circulation, 2014.
3. Fengler, B.T., W.J. Brady, and C.U. Plautz, *Atrial fibrillation in the Wolff-Parkinson-White syndrome: ECG recognition and treatment in the ED*. The American Journal of Emergency Medicine, 2007. **25**(5): p. 576-583.
4. Khairy, P. and S. Balaji, *Cardiac Arrhythmias In Congenital Heart Diseases*. Indian Pacing and Electrophysiology Journal, 2009. **9**(6): p. 299-317.
5. Hutson, M.R. and M.L. Kirby, *Neural crest and cardiovascular development: A 20-year perspective*. Birth Defects Research Part C: Embryo Today: Reviews, 2003. **69**(1): p. 2-13.
6. Hutson, M.R. and M.L. Kirby. *Model systems for the study of heart development and disease: cardiac neural crest and conotruncal malformations*. in *Seminars in cell & developmental biology*. 2007. Elsevier.
7. Burd, L., et al., *Congenital Heart Defects and Fetal Alcohol Spectrum Disorders*. Congenital Heart Disease, 2007. **2**(4): p. 250-255.
8. Karunamuni, G., et al., *Ethanol exposure alters early cardiac function in the looping heart: a mechanism for congenital heart defects?* American Journal of Physiology - Heart and Circulatory Physiology, 2013.
9. Serrano, M., et al., *Fetal alcohol syndrome: cardiac birth defects in mice and prevention with folate*. American journal of obstetrics and gynecology, 2010. **203**(1): p. 75. e7-75. e15.
10. Control, C.f.D. and Prevention, *Surveillance for fetal alcohol syndrome using multiple sources--Atlanta, Georgia, 1981-1989*. MMWR. Morbidity and mortality weekly report, 1997. **46**(47): p. 1118.
11. Control, C.f.D. and Prevention, *Update: trends in fetal alcohol syndrome--United States, 1979-1993*. MMWR. Morbidity and mortality weekly report, 1995. **44**(13): p. 249.
12. May, P.A. and J.P. Gossage, *Estimating the prevalence of fetal alcohol syndrome: A summary*. Alcohol Research and Health, 2001. **25**(3): p. 159-167.
13. May, P.A., et al., *Prevalence and epidemiologic characteristics of FASD from various research methods with an emphasis on recent in - school studies*. Developmental disabilities research reviews, 2009. **15**(3): p. 176-192.
14. Fox, D.J., et al., *Fetal alcohol syndrome among children aged 7-9 years-Arizona, colorado, and new york, 2010*. MMWR. Morbidity and mortality weekly report, 2015. **64**(3): p. 54-57.
15. May, P.A., et al., *Prevalence and characteristics of fetal alcohol spectrum disorders*. Pediatrics, 2014. **134**(5): p. 855-866.
16. Abel, E., *Fetal Alcohol Syndrome: Medical Economics*. Oradell, NJ, 1990.

17. Ammann, A.J., et al., *The digeorge syndrome and the fetal alcohol syndrome*. American Journal of Diseases of Children, 1982. **136**(10): p. 906-908.
18. Sulik, K.K., et al., *Fetal alcohol syndrome and DiGeorge anomaly. Critical ethanol exposure periods for craniofacial malformations as illustrated in an animal model*. American Journal of Medical Genetics, 1986. **25**(S2): p. 97-112.
19. Menendez, L., et al., *Directed differentiation of human pluripotent cells to neural crest stem cells*. Nat. Protocols, 2013. **8**(1): p. 203-212.
20. Smith, S.M., et al., *Neural crest development in fetal alcohol syndrome*. Birth Defects Research Part C: Embryo Today: Reviews, 2014. **102**(3): p. 210-220.
21. Czarnobaj, J., et al., *The different effects on cranial and trunk neural crest cell behaviour following exposure to a low concentration of alcohol in vitro*. Archives of oral biology, 2014. **59**(5): p. 500-512.
22. Cartwright, M.M. and S.M. Smith, *Increased Cell Death and Reduced Neural Crest Cell Numbers in Ethanol-Exposed Embryos: Partial Basis for the Fetal Alcohol Syndrome Phenotype*. Alcoholism: Clinical and Experimental Research, 1995. **19**(2): p. 378-386.
23. Rovasio, R. and N. Battiato, *Role of early migratory neural crest cells in developmental anomalies induced by ethanol*. The International journal of developmental biology, 1995. **39**(2): p. 421-422.
24. Cavieres, M.F. and S.M. Smith, *Genetic and developmental modulation of cardiac deficits in prenatal alcohol exposure*. Alcoholism: Clinical and Experimental Research, 2000. **24**(1): p. 102-109.
25. Wang, G. and E. Bieberich, *Prenatal alcohol exposure triggers ceramide-induced apoptosis in neural crest-derived tissues concurrent with defective cranial development*. Cell death & disease, 2010. **1**(5): p. e46.
26. Kirby, M.L., *Cardiac Development*. 2007, Oxford University Press.
27. Leatherbury, L., et al., *Hemodynamic Changes. Wall stresses and pressure gradients in neural crest-ablated chick embryos*. Annals of the New York Academy of Sciences, 1990. **588**(1): p. 305-313.
28. Leatherbury, L., et al., *Microcinematography of the developing heart in neural crest-ablated chick embryos*. Circulation, 1990. **81**(3): p. 1047-57.
29. Leatherbury, L., et al., *Hemodynamic changes and compensatory mechanisms during early cardiogenesis after neural crest ablation in chick embryos*. Pediatric research, 1991. **30**(6): p. 509-512.
30. Conway, S.J., et al., *Neural crest is involved in development of abnormal myocardial function*. Journal of molecular and cellular cardiology, 1997. **29**(10): p. 2675-2685.
31. Nosek, T., et al., *Effect of cardiac neural crest ablation on contractile force and calcium uptake and release in chick heart*. American Journal of Physiology-Heart and Circulatory Physiology, 1997. **273**(3): p. H1464-H1471.
32. Waldo, K., et al., *A novel role for cardiac neural crest in heart development*. The Journal of Clinical Investigation, 1999. **103**(11): p. 1499-1507.

33. Nichols, C.A. and T.L. Creazzo, *L-type Ca<sup>2+</sup> channel function in the avian embryonic heart after cardiac neural crest ablation*. American Journal of Physiology-Heart and Circulatory Physiology, 2005. **288**(3): p. H1173-H1178.
34. Nakamura, T., M.C. Colbert, and J. Robbins, *Neural crest cells retain multipotential characteristics in the developing valves and label the cardiac conduction system*. Circulation research, 2006. **98**(12): p. 1547-1554.
35. Gurjarpadhye, A., et al., *Cardiac neural crest ablation inhibits compaction and electrical function of conduction system bundles*. American Journal of Physiology - Heart and Circulatory Physiology, 2007. **292**(3): p. H1291-H1300.
36. Mikawa, T. and R. Hurtado, *Development of the cardiac conduction system*. Seminars in Cell & Developmental Biology, 2007. **18**(1): p. 90-100.
37. Chi, N.C., et al., *Cardiac conduction is required to preserve cardiac chamber morphology*. Proceedings of the National Academy of Sciences, 2010. **107**(33): p. 14662-14667.
38. Reaume, A., et al., *Cardiac malformation in neonatal mice lacking connexin43*. Science, 1995. **267**(5205): p. 1831-1834.
39. Ewart, J.L., et al., *Heart and neural tube defects in transgenic mice overexpressing the Cx43 gap junction gene*. Development, 1997. **124**(7): p. 1281-1292.
40. Lo, C.W., *Role of Gap Junctions in Cardiac Conduction and Development: Insights From the Connexin Knockout Mice*. Circulation Research, 2000. **87**(5): p. 346-348.
41. Kirchhoff, S., et al., *Reduced cardiac conduction velocity and predisposition to arrhythmias in connexin40-deficient mice*. Current Biology, 1998. **8**(5): p. 299-302.
42. Hove, J.R., et al., *Intracardiac fluid forces are an essential epigenetic factor for embryonic cardiogenesis*. Nature, 2003. **421**(6919): p. 172-177.
43. Yashiro, K., H. Shiratori, and H. Hamada, *Haemodynamics determined by a genetic programme govern asymmetric development of the aortic arch*. Nature, 2007. **450**(7167): p. 285-288.
44. Granados-Riveron, J.T. and J.D. Brook, *The impact of mechanical forces in heart morphogenesis*. Circulation: Cardiovascular Genetics, 2012. **5**(1): p. 132-142.
45. Kain, K.H., et al., *The chick embryo as an expanding experimental model for cancer and cardiovascular research*. Developmental dynamics : an official publication of the American Association of Anatomists, 2014. **243**(2): p. 216-228.
46. Nishibatake, M., M.L. Kirby, and L.H. Van Mierop, *Pathogenesis of persistent truncus arteriosus and dextroposed aorta in the chick embryo after neural crest ablation*. Circulation, 1987. **75**(1): p. 255-64.
47. Viktor, H. and L.H. Howard, *A series of normal stages in the development of the chick embryo*. Developmental Dynamics, 1992. **195**(4): p. 231-272.
48. Watanabe, M., et al., *Probing the Electrophysiology of the Developing Heart*. Journal of Cardiovascular Development and Disease, 2016. **3**(1): p. 10.
49. Efimov, I.R., V.P. Nikolski, and G. Salama, *Optical Imaging of the Heart*. Circulation Research, 2004. **95**(1): p. 21-33.
50. Schaffer, P., et al., *Di-4-ANEPPS causes photodynamic damage to isolated cardiomyocytes*. Pflügers Archiv. **426**(6): p. 548-551.

51. Larsen, A.P., et al., *The voltage-sensitive dye di-4-ANEPPS slows conduction velocity in isolated guinea pig hearts*. Heart rhythm : the official journal of the Heart Rhythm Society, 2012. **9**(9): p. 1493-1500.
52. Loew, L.M., *Design and Use of Organic Voltage Sensitive Dyes*, in *Membrane Potential Imaging in the Nervous System and Heart*, M. Canepari, D. Zecevic, and O. Bernus, Editors. 2015, Springer International Publishing: Cham. p. 27-53.
53. Cohen, L.B., et al., *Changes in axon fluorescence during activity: Molecular probes of membrane potential*. The Journal of Membrane Biology. **19**(1): p. 1-36.
54. Fluhler, E., V.G. Burnham, and L.M. Loew, *Spectra, membrane binding, and potentiometric responses of new charge shift probes*. Biochemistry, 1985. **24**(21): p. 5749-5755.
55. Kee, M.Z.L., et al., *Imaging activity of neuronal populations with new long-wavelength voltage-sensitive dyes*. Brain Cell Biology, 2009. **36**(5): p. 157-172.
56. Shoham, D., et al., *Imaging Cortical Dynamics at High Spatial and Temporal Resolution with Novel Blue Voltage-Sensitive Dyes*. Neuron, 1999. **24**(4): p. 791-802.
57. Miller, E.W., et al., *Optically monitoring voltage in neurons by photo-induced electron transfer through molecular wires*. Proceedings of the National Academy of Sciences of the United States of America, 2012. **109**(6): p. 2114-2119.
58. Kuhn, B., P. Fromherz, and W. Denk, *High Sensitivity of Stark-Shift Voltage-Sensing Dyes by One- or Two-Photon Excitation Near the Red Spectral Edge*. Biophysical Journal, 2004. **87**(1): p. 631-639.
59. Cacciatore, T.W., et al., *Identification of Neural Circuits by Imaging Coherent Electrical Activity with FRET-Based Dyes*. Neuron, 1999. **23**(3): p. 449-459.
60. Tsutsui, H., et al., *Improving membrane voltage measurements using FRET with new fluorescent proteins*. Nat Meth, 2008. **5**(8): p. 683-685.
61. Hochbaum, D.R., et al., *All-optical electrophysiology in mammalian neurons using engineered microbial rhodopsins*. Nat Meth, 2014. **11**(8): p. 825-833.
62. Cacciatore, T.W., et al., *Identification of Neural Circuits by Imaging Coherent Electrical Activity with FRET-Based Dyes*. Neuron, 1999. **23**(3): p. 449-459.
63. Song, L., et al., *Photobleaching kinetics of fluorescein in quantitative fluorescence microscopy*. Biophysical Journal, 1995. **68**(6): p. 2588-2600.
64. Rohr, S. and B.M. Salzberg, *Multiple site optical recording of transmembrane voltage (MSORTV) in patterned growth heart cell cultures: assessing electrical behavior, with microsecond resolution, on a cellular and subcellular scale*. Biophysical Journal, 1994. **67**(3): p. 1301-1315.
65. Svoboda, K. and R. Yasuda, *Principles of Two-Photon Excitation Microscopy and Its Applications to Neuroscience*. Neuron, 2006. **50**(6): p. 823-839.
66. Jiang, J., K.B. Eisenthal, and R. Yuste, *Second Harmonic Generation in Neurons: Electro-Optic Mechanism of Membrane Potential Sensitivity*. Biophysical Journal, 2007. **93**(5): p. L26-L28.
67. Sacconi, L., et al. *Action potential detection by non-linear microscopy*. 2009.

68. Loew, L. and A. Lewis, *Second Harmonic Imaging of Membrane Potential*, in *Membrane Potential Imaging in the Nervous System*, M. Canepari and D. Zecevic, Editors. 2011, Springer New York. p. 147-155.
69. Theer, P., et al., *Second-Harmonic Generation Imaging of Membrane Potential with Retinal Analogues*. *Biophysical Journal*, 2011. **100**(1): p. 232-242.
70. Akemann, W., et al., *Imaging brain electric signals with genetically targeted voltage-sensitive fluorescent proteins*. *Nat Meth*, 2010. **7**(8): p. 643-649.
71. Tsutsui, H., et al., *Visualizing voltage dynamics in zebrafish heart*. *The Journal of Physiology*, 2010. **588**(Pt 12): p. 2017-2021.
72. Canepari, M., D. Zecevic, and O. Bernus, *Membrane Potential Imaging in the Nervous System and Heart*. Vol. 859. 2015: Springer.
73. Davidenko, J.M., et al., *Sustained vortex-like waves in normal isolated ventricular muscle*. *Proceedings of the National Academy of Sciences*, 1990. **87**(22): p. 8785-8789.
74. Davidenko, J.M., et al., *Stationary and drifting spiral waves of excitation in isolated cardiac muscle*. *Nature*, 1992. **355**(6358): p. 349-351.
75. Gray, R.A., A.M. Pertsov, and J. Jalife, *Spatial and temporal organization during cardiac fibrillation*. *Nature*, 1998. **392**(6671): p. 75-78.
76. Fujii, S., A. Hirota, and K. Kamino, *Optical signals from early embryonic chick heart stained with potential sensitive dyes: evidence for electrical activity*. *The Journal of Physiology*, 1980. **304**(1): p. 503-518.
77. Fujii, S., A. Hirota, and K. Kamino, *Optical recording of development of electrical activity in embryonic chick heart during early phases of cardiogenesis*. *The Journal of Physiology*, 1981. **311**(1): p. 147-160.
78. Fujii, S., A. Hirota, and K. Kamino, *Action potential synchrony in embryonic precontractile chick heart: optical monitoring with potentiometric dyes*. *The Journal of Physiology*, 1981. **319**(1): p. 529-541.
79. Kamino, K., A. Hirota, and S. Fujii, *Localization of Pacemaking Activity in Early Embryonic Heart Monitored Using Voltage-Sensitive Dye*. *Nature*, 1981. **290**(5807): p. 595-597.
80. Hirota, A., et al., *Initial development of conduction pattern of spontaneous action potential in early embryonic precontractile chick heart*. *Developmental Biology*, 1983. **99**(2): p. 517-523.
81. Bressan, M., G. Liu, and T. Mikawa, *Early Mesodermal Cues Assign Avian Cardiac Pacemaker Fate Potential in a Tertiary Heart Field*. *Science*, 2013. **340**(6133): p. 744-748.
82. Chuck, E.T., et al., *Transitions in ventricular activation revealed by two-dimensional optical mapping*. *The Anatomical Record Part A: Discoveries in Molecular, Cellular, and Evolutionary Biology*, 2004. **280A**(2): p. 990-1000.
83. Sedmera, D., et al., *Developmental transitions in electrical activation patterns in chick embryonic heart*. *The Anatomical Record Part A: Discoveries in Molecular, Cellular, and Evolutionary Biology*, 2004. **280A**(2): p. 1001-1009.
84. Sedmera, D., *Function and form in the developing cardiovascular system*. *Cardiovascular Research*, 2011. **91**(2): p. 252-259.

85. Bressan, M., et al., *Reciprocal myocardial-endocardial interactions pattern the delay in atrioventricular junction conduction*. Development, 2014: p. dev. 110007.
86. Panakova, D., A.A. Werdich, and C.A. MacRae, *Wnt11 patterns a myocardial electrical gradient through regulation of the L-type Ca<sup>2+</sup> channel*. Nature, 2010. **466**(7308): p. 874-U109.
87. Werdich, A.A., et al., *The zebrafish as a novel animal model to study the molecular mechanisms of mechano-electrical feedback in the heart*. Progress in Biophysics and Molecular Biology, 2012. **110**(2–3): p. 154-165.
88. Mosimann, C., et al., *Chamber identity programs drive early functional partitioning of the heart*. Nat Commun, 2015. **6**.
89. Laughner, J.I., et al., *Processing and analysis of cardiac optical mapping data obtained with potentiometric dyes*. American Journal of Physiology - Heart and Circulatory Physiology, 2012. **303**(7): p. H753-H765.
90. Gu, S., et al., *Mapping conduction velocity of early embryonic hearts with a robust fitting algorithm*. Biomedical Optics Express, 2015. **6**(6): p. 2138-2157.
91. Salama, G., A. Kanai, and I.R. Efimov, *Subthreshold stimulation of Purkinje fibers interrupts ventricular tachycardia in intact hearts. Experimental study with voltage-sensitive dyes and imaging techniques*. Circulation Research, 1994. **74**(4): p. 604-19.
92. Bayly, P.V., et al., *Estimation of conduction velocity vector fields from epicardial mapping data*. IEEE Transactions on Biomedical Engineering, 1998. **45**(5): p. 563-571.
93. Sakai, T., *Cytochalasin D as the Depressant of Contraction for the Optical Monitoring of Action Potentials in Isolated Rat Atrium*. The Journal of Physiological Sciences, 2006. **56**(5): p. 385-388.
94. Fedorov, V.V., et al., *Application of blebbistatin as an excitation–contraction uncoupler for electrophysiologic study of rat and rabbit hearts*. Heart Rhythm, 2007. **4**(5): p. 619-626.
95. Shoji, K., et al., *Cytochalasin D acts as an inhibitor of the actin–cofilin interaction*. Biochemical and Biophysical Research Communications, 2012. **424**(1): p. 52-57.
96. Kettlewell, S., et al., *The electrophysiological and mechanical effects of 2,3-butanedione monoxime and cytochalasin-D in the Langendorff perfused rabbit heart*. Experimental Physiology, 2004. **89**(2): p. 163-172.
97. Brack, K.E., et al., *The mechanical uncoupler blebbistatin is associated with significant electrophysiological effects in the isolated rabbit heart*. Experimental Physiology, 2013. **98**(5): p. 1009-1027.
98. Salama, G., R. Lombardi, and J. Elson, *Maps of optical action potentials and NADH fluorescence in intact working hearts*. American Journal of Physiology - Heart and Circulatory Physiology, 1987. **252**(2): p. H384-H394.
99. Tai, D.C.-S., et al., *Correction of motion artifact in transmembrane voltage-sensitive fluorescent dye emission in hearts*. American Journal of Physiology - Heart and Circulatory Physiology, 2004. **287**(3): p. H985-H993.

100. Rohde, G.K., B.M. Dawant, and L. Shien-Fong, *Correction of motion artifact in cardiac optical mapping using image registration*. Biomedical Engineering, IEEE Transactions on, 2005. **52**(2): p. 338-341.
101. Knisley, S.B., et al., *Ratiometry of transmembrane voltage-sensitive fluorescent dye emission in hearts*. American Journal of Physiology - Heart and Circulatory Physiology, 2000. **279**(3): p. H1421-H1433.
102. Caldwell, B.J., et al., *Intramural Measurement of Transmembrane Potential in the Isolated Pig Heart: Validation of a Novel Technique*. Journal of Cardiovascular Electrophysiology, 2005. **16**(9): p. 1001-1010.
103. Hooks, D.A., et al., *Intramural Multisite Recording of Transmembrane Potential in the Heart*. Biophysical Journal, 2001. **81**(5): p. 2671-2680.
104. Walton, R.D., et al., *Dual excitation wavelength epifluorescence imaging of transmural electrophysiological properties in intact hearts*. Heart Rhythm, 2010. **7**(12): p. 1843-1849.
105. Khait, V.D., et al., *Method for the three-dimensional localization of intramyocardial excitation centers using optical imaging*. Journal of Biomedical Optics, 2006. **11**(3): p. 034007-034007-12.
106. Mitrea, B.G., B.J. Caldwell, and A.M. Pertsov, *Imaging electrical excitation inside the myocardial wall*. Biomedical Optics Express, 2011. **2**(3): p. 620-633.
107. Lin, S.-F. and J.J.P. Wikswo, *Panoramic Optical Imaging of Electrical Propagation in Isolated Heart*. Journal of Biomedical Optics, 1999. **4**(2): p. 200-207.
108. Kay, M.W., P.M. Amison, and J.M. Rogers, *Three-dimensional surface reconstruction and panoramic optical mapping of large hearts*. Biomedical Engineering, IEEE Transactions on, 2004. **51**(7): p. 1219-1229.
109. Qu, F., et al., *Three-dimensional panoramic imaging of cardiac arrhythmias in rabbit heart*. Journal of Biomedical Optics, 2007. **12**(4): p. 044019-044019.
110. Hou, J.H., et al., *Simultaneous mapping of membrane voltage and calcium in zebrafish heart in vivo reveals chamber-specific developmental transitions in ionic currents*. Frontiers in physiology, 2014. **5**.
111. Elharrar, V. and B. Surawicz, *Cycle length effect on restitution of action potential duration in dog cardiac fibers*. American Journal of Physiology-Heart and Circulatory Physiology, 1983. **244**(6): p. H782-H792.
112. Eloff, B.C., et al., *High resolution optical mapping reveals conduction slowing in connexin43 deficient mice*. Cardiovascular Research, 2001. **51**(4): p. 681-690.
113. Morley, G.E., et al., *Characterization of Conduction in the Ventricles of Normal and Heterozygous Cx43 Knockout Mice Using Optical Mapping*. Journal of Cardiovascular Electrophysiology, 1999. **10**(10): p. 1361-1375.
114. Josephson, M.E., et al., *Recurrent sustained ventricular tachycardia. 2. Endocardial mapping*. Circulation, 1978. **57**(3): p. 440-7.
115. Mason, J.W. and R.A. Winkle, *Electrode-catheter arrhythmia induction in the selection and assessment of antiarrhythmic drug therapy for recurrent ventricular tachycardia*. Circulation, 1978. **58**(6): p. 971-85.
116. Fork, R.L., *Laser Stimulation of Nerve Cells in Aplysia*. Science, 1971. **171**(3974): p. 907-908.

117. Smith, N.I., et al., *A femtosecond laser pacemaker for heart muscle cells*. Optics Express, 2008. **16**(12): p. 8604-8616.
118. Jenkins, M.W., et al., *Optical pacing of the adult rabbit heart*. Biomedical Optics Express, 2013. **4**(9): p. 1626-1635.
119. Wang, Y.T., et al., *Optical stimulation enables paced electrophysiological studies in embryonic hearts*. Biomedical Optics Express, 2014. **5**(4): p. 1000-1013.
120. Jenkins, M.W., et al., *Optical pacing of the embryonic heart*. Nat Photon, 2010. **4**(9): p. 623-626.
121. Huang, D., et al., *Optical coherence tomography*. Science, 1991. **254**(5035): p. 1178-1181.
122. Drexler, W. and J.G. Fujimoto, *Retinal Optical Coherence Tomography*, in *Optical Coherence Tomography: Technology and Applications*, W. Drexler and J.G. Fujimoto, Editors. 2008, Springer Berlin Heidelberg: Berlin, Heidelberg. p. 983-1045.
123. Huang, D., Y. Li, and M. Tang, *Anterior Eye Imaging with Optical Coherence Tomography*, in *Optical Coherence Tomography: Technology and Applications*, W. Drexler and J.G. Fujimoto, Editors. 2008, Springer Berlin Heidelberg: Berlin, Heidelberg. p. 961-981.
124. Qi, X., M.V. Sivak, and A.M. Rollins, *Optical Coherence Tomography for Gastrointestinal Endoscopy*, in *Optical Coherence Tomography: Technology and Applications*, W. Drexler and J.G. Fujimoto, Editors. 2008, Springer Berlin Heidelberg: Berlin, Heidelberg. p. 1047-1081.
125. Tearney, G.J., I.-K. Jang, and B.E. Bouma, *Imaging Coronary Atherosclerosis and Vulnerable Plaques with Optical Coherence Tomography*, in *Optical Coherence Tomography: Technology and Applications*, W. Drexler and J.G. Fujimoto, Editors. 2008, Springer Berlin Heidelberg: Berlin, Heidelberg. p. 1083-1101.
126. Welzel, J., et al., *OCT in Dermatology*, in *Optical Coherence Tomography: Technology and Applications*, W. Drexler and J.G. Fujimoto, Editors. 2008, Springer Berlin Heidelberg: Berlin, Heidelberg. p. 1103-1122.
127. de Boer, J.F., *Spectral/Fourier Domain Optical Coherence Tomography*, in *Optical Coherence Tomography: Technology and Applications*, W. Drexler and G.J. Fujimoto, Editors. 2015, Springer International Publishing: Cham. p. 165-193.
128. Hu, Z. and A.M. Rollins, *Fourier domain optical coherence tomography with a linear-in-wavenumber spectrometer*. Optics Letters, 2007. **32**(24): p. 3525-3527.
129. Wang, S., et al., *Direct four-dimensional structural and functional imaging of cardiovascular dynamics in mouse embryos with 1.5-MHz optical coherence tomography*. Optics Letters, 2015. **40**(20): p. 4791-4794.
130. Singh, M., et al., *Phase-sensitive optical coherence elastography at 1.5 million A-Lines per second*. Optics Letters, 2015. **40**(11): p. 2588-2591.
131. Zhi, Z., et al., *4D optical coherence tomography-based micro-angiography achieved by 1.6-MHz FDML swept source*. Optics Letters, 2015. **40**(8): p. 1779-1782.
132. Choma, M., et al., *Sensitivity advantage of swept source and Fourier domain optical coherence tomography*. Optics Express, 2003. **11**(18): p. 2183-2189.

133. de Boer, J.F., et al., *Improved signal-to-noise ratio in spectral-domain compared with time-domain optical coherence tomography*. Optics Letters, 2003. **28**(21): p. 2067-2069.
134. Leitgeb, R., C. Hitzenberger, and A. Fercher, *Performance of fourier domain vs. time domain optical coherence tomography*. Optics Express, 2003. **11**(8): p. 889-894.
135. Boppart, S.A., et al., *Imaging developing neural morphology using optical coherence tomography*. Journal of Neuroscience Methods, 1996. **70**(1): p. 65-72.
136. Boppart, S.A., et al., *Investigation of Developing Embryonic Morphology Using Optical Coherence Tomography*. Developmental Biology, 1996. **177**(1): p. 54-63.
137. Boppart, S.A., et al., *In vivo cellular optical coherence tomography imaging*. Nat Med, 1998. **4**(7): p. 861-865.
138. Adler, D.C., et al., *Optical coherence tomography contrast enhancement using spectroscopic analysis with spectral autocorrelation*. Optics Express, 2004. **12**(22): p. 5487-5501.
139. Kagemann, L., et al., *Repeated, noninvasive, high resolution spectral domain optical coherence tomography imaging of zebrafish embryos*. Molecular Vision, 2008. **14**: p. 2157-2170.
140. Divakar Rao, K., et al., *Noninvasive Imaging of Ethanol-Induced Developmental Defects in Zebrafish Embryos Using Optical Coherence Tomography*. Birth Defects Research Part B: Developmental and Reproductive Toxicology, 2012. **95**(1): p. 7-11.
141. Gladys, F.M., et al., *Developmental and morphological studies in Japanese medaka with ultra-high resolution optical coherence tomography*. Biomedical Optics Express, 2015. **6**(2): p. 297-308.
142. Larina, I.V., et al., *Live imaging of rat embryos with Doppler swept-source optical coherence tomography*. Journal of Biomedical Optics, 2009. **14**(5): p. 050506-050506-3.
143. Larina, I.V., et al., *Optical Coherence Tomography for live imaging of mammalian development*. Current Opinion in Genetics & Development, 2011. **21**(5): p. 579-584.
144. Larina, I.V., et al., *Optical coherence tomography for live phenotypic analysis of embryonic ocular structures in mouse models*. Journal of Biomedical Optics, 2012. **17**(8): p. 0814101-0814104.
145. Syed, S.H., et al., *Optical coherence tomography for high-resolution imaging of mouse development in utero*. Journal of Biomedical Optics, 2011. **16**(4): p. 046004-046004-6.
146. Boppart, S.A., et al., *Noninvasive assessment of the developing Xenopus cardiovascular system using optical coherence tomography*. Proceedings of the National Academy of Sciences, 1997. **94**(9): p. 4256-4261.
147. Tobita, K. and B.B. Keller, *Right and left ventricular wall deformation patterns in normal and left heart hypoplasia chick embryos*. American Journal of Physiology - Heart and Circulatory Physiology, 2000. **279**(3): p. H959-H969.

148. Yelbuz, T.M., et al., *Optical Coherence Tomography: A New High-Resolution Imaging Technology to Study Cardiac Development in Chick Embryos*. *Circulation*, 2002. **106**(22): p. 2771-2774.
149. Rollins, A.M., et al., *In vivo video rate optical coherence tomography*. *Optics Express*, 1998. **3**(6): p. 219-229.
150. Yazdanfar, S., M.D. Kulkarni, and J.A. Izatt, *High resolution imaging of in vivo cardiac dynamics using color Doppler optical coherence tomography*. *Optics Express*, 1997. **1**(13): p. 424-431.
151. Yang, V.X.D., et al., *High speed, wide velocity dynamic range Doppler optical coherence tomography (Part II): Imaging in vivo cardiac dynamics of Xenopus laevis*. *Optics Express*, 2003. **11**(14): p. 1650-1658.
152. Chen, Z., et al., *Noninvasive imaging of in vivo blood flow velocity using optical Doppler tomography*. *Optics Letters*, 1997. **22**(14): p. 1119-1121.
153. Jenkins, M.W., et al., *Ultrahigh-speed optical coherence tomography imaging and visualization of the embryonic avian heart using a buffered Fourier Domain Mode Locked laser*. *Opt. Express*, 2007. **15**(10): p. 6251-6267.
154. Jenkins, M.W., et al., *In vivo gated 4D imaging of the embryonic heart using optical coherence tomography*. *Journal of Biomedical Optics*, 2007. **12**(3): p. 030505-030505-3.
155. Männer, J., et al., *High-resolution in vivo imaging of the cross-sectional deformations of contracting embryonic heart loops using optical coherence tomography*. *Developmental Dynamics*, 2008. **237**(4): p. 953-961.
156. Liu, A., et al., *Efficient postacquisition synchronization of 4-D nongated cardiac images obtained from optical coherence tomography: application to 4-D reconstruction of the chick embryonic heart*. *Journal of Biomedical Optics*, 2009. **14**(4): p. 044020-044020-11.
157. Happel, C.M., et al., *Rotationally acquired four-dimensional optical coherence tomography of embryonic chick hearts using retrospective gating on the common central A-scan*. *Journal of Biomedical Optics*, 2011. **16**(9): p. 096007-096007-6.
158. Jenkins, M.W., et al., *4D embryonic cardiography using gated optical coherence tomography*. *Optics Express*, 2006. **14**(2): p. 736-748.
159. Gargsha, M., et al., *High temporal resolution OCT using image-based retrospective gating*. *Optics express*, 2009. **17**(13): p. 10786-10799.
160. Bhat, S., et al., *4D Reconstruction of the Beating Embryonic Heart From Two Orthogonal Sets of Parallel Optical Coherence Tomography Slice-Sequences*. *IEEE Transactions on Medical Imaging*, 2013. **32**(3): p. 578-588.
161. Jenkins, M.W., et al., *Measuring hemodynamics in the developing heart tube with four-dimensional gated Doppler optical coherence tomography*. *Journal of Biomedical Optics*, 2010. **15**(6): p. 066022-066022-4.
162. Ma, Z., et al., *Measurement of absolute blood flow velocity in outflow tract of HH18 chicken embryo based on 4D reconstruction using spectral domain optical coherence tomography*. *Biomedical Optics Express*, 2010. **1**(3): p. 798-811.
163. Sandra, R., et al., *Changes in wall motion and blood flow in the outflow tract of chick embryonic hearts observed with optical coherence tomography after outflow*

- tract banding and vitelline-vein ligation*. *Physics in Medicine and Biology*, 2008. **53**(18): p. 5077.
164. Larina, I.V., et al., *Hemodynamic measurements from individual blood cells in early mammalian embryos with Doppler swept source OCT*. *Optics Letters*, 2009. **34**(7): p. 986-988.
  165. Sudheendran, N., et al., *Speckle variance OCT imaging of the vasculature in live mammalian embryos*. *Laser Physics Letters*, 2011. **8**(3): p. 247.
  166. Liu, A., et al., *Dynamic variation of hemodynamic shear stress on the walls of developing chick hearts: computational models of the heart outflow tract*. *Engineering with Computers*, 2009. **25**(1): p. 73-86.
  167. Choma, M.A., et al., *Heart wall velocimetry and exogenous contrast-based cardiac flow imaging in *Drosophila melanogaster* using Doppler optical coherence tomography*. *Journal of Biomedical Optics*, 2010. **15**(5): p. 056020-056020-6.
  168. Li, P., et al., *Measurement of Strain and Strain Rate in Embryonic Chick Heart In Vivo Using Spectral Domain Optical Coherence Tomography*. *IEEE Transactions on Biomedical Engineering*, 2011. **58**(8): p. 2333-2338.
  169. Liu, A., et al., *Quantifying blood flow and wall shear stresses in the outflow tract of chick embryonic hearts*. *Computers & Structures*, 2011. **89**(11–12): p. 855-867.
  170. Li, P. and R.K. Wang, *Optical coherence tomography provides an ability to assess mechanical property of cardiac wall of developing outflow tract in embryonic heart in vivo*. *Journal of Biomedical Optics*, 2012. **17**(12): p. 120502-120502.
  171. Li, P., et al., *In vivo functional imaging of blood flow and wall strain rate in outflow tract of embryonic chick heart using ultrafast spectral domain optical coherence tomography*. *Journal of Biomedical Optics*, 2012. **17**(9): p. 0960061-0960068.
  172. Liu, A., et al., *Biomechanics of the Chick Embryonic Heart Outflow Tract at HH18 Using 4D Optical Coherence Tomography Imaging and Computational Modeling*. *PLoS ONE*, 2012. **7**(7): p. e40869.
  173. Peterson, L.M., et al., *4D shear stress maps of the developing heart using Doppler optical coherence tomography*. *Biomedical Optics Express*, 2012. **3**(11): p. 3022-3032.
  174. Jenkins, M.W., et al., *Phenotyping transgenic embryonic murine hearts using optical coherence tomography*. *Appl. Opt.*, 2007. **46**(10): p. 1776-1781.
  175. Gu, S., et al., *Optical coherence tomography captures rapid hemodynamic responses to acute hypoxia in the cardiovascular system of early embryos*. *Developmental Dynamics*, 2012. **241**(3): p. 534-544.
  176. Ma, L., et al., *Arrhythmia Caused by a *Drosophila* Tropomyosin Mutation Is Revealed Using a Novel Optical Coherence Tomography Instrument*. *PLoS ONE*, 2010. **5**(12): p. e14348.
  177. Happel, C.M., et al., *Integration of an optical coherence tomography (OCT) system into an examination incubator to facilitate in vivo imaging of cardiovascular development in higher vertebrate embryos under stable physiological conditions*. *Annals of Anatomy - Anatomischer Anzeiger*, 2011. **193**(5): p. 425-435.

178. Jenkins, M.W., M. Watanabe, and A.M. Rollins, *Longitudinal Imaging of Heart Development With Optical Coherence Tomography*. Selected Topics in Quantum Electronics, IEEE Journal of, 2012. **18**(3): p. 1166-1175.
179. Men, J., et al., *Optical coherence tomography for brain imaging and developmental biology*. IEEE Journal of Selected Topics in Quantum Electronics, 2016. **PP**(99): p. 1-1.
180. Karunamuni, G., et al., *Using optical coherence tomography to rapidly phenotype and quantify congenital heart defects associated with prenatal alcohol exposure*. Developmental Dynamics, 2015. **244**(4): p. 607-618.
181. Larina, I.V., et al. *Enhanced OCT imaging of embryonic tissue with optical clearing*. 2009.
182. Huisken, J. and D.Y. Stainier, *Selective plane illumination microscopy techniques in developmental biology*. Development, 2009. **136**(12): p. 1963-1975.
183. Huisken, J., et al., *Optical sectioning deep inside live embryos by selective plane illumination microscopy*. Science, 2004. **305**(5686): p. 1007-1009.
184. Huisken, J. and D.Y. Stainier, *Even fluorescence excitation by multidirectional selective plane illumination microscopy (mSPIM)*. Optics letters, 2007. **32**(17): p. 2608-2610.
185. Keller, P.J., et al., *Reconstruction of Zebrafish Early Embryonic Development by Scanned Light Sheet Microscopy*. Science, 2008. **322**(5904): p. 1065-1069.
186. Planchon, T.A., et al., *Rapid three-dimensional isotropic imaging of living cells using Bessel beam plane illumination*. Nature methods, 2011. **8**(5): p. 417-423.
187. Fahrbach, F.O., et al., *Light-sheet microscopy in thick media using scanned Bessel beams and two-photon fluorescence excitation*. Optics Express, 2013. **21**(11): p. 13824-13839.
188. Vettenburg, T., et al., *Light-sheet microscopy using an Airy beam*. Nat Meth, 2014. **11**(5): p. 541-544.
189. Philipp J Keller<sup>1</sup>, Annette D Schmidt<sup>3</sup>, Anthony Santella<sup>4</sup>, Khaled Khairy<sup>1</sup>, Zhirong Bao<sup>4</sup>, Joachim Wittbrodt<sup>3,5</sup> & Ernst H K Stelzer, *Fast, high-contrast imaging of animal development with scanned light sheet-based structured-illumination microscopy*. Nat Meth, 2010. **7**(8): p. 6.
190. Chen, B.-C., et al., *Lattice light-sheet microscopy: Imaging molecules to embryos at high spatiotemporal resolution*. Science, 2014. **346**(6208): p. 1257998.
191. Dodt, H.-U., et al., *Ultramicroscopy: three-dimensional visualization of neuronal networks in the whole mouse brain*. Nature methods, 2007. **4**(4): p. 331-336.
192. Wu, Y., et al., *Spatially isotropic four-dimensional imaging with dual-view plane illumination microscopy*. Nature biotechnology, 2013. **31**(11): p. 1032-1038.
193. Silvestri, L., et al., *Confocal light sheet microscopy: micron-scale neuroanatomy of the entire mouse brain*. Optics express, 2012. **20**(18): p. 20582-20598.
194. Yang, Z., et al., *Dual-slit confocal light sheet microscopy for in vivo whole-brain imaging of zebrafish*. Biomedical Optics Express, 2015. **6**(5): p. 1797-1811.
195. Keller, P.J. and E.H.K. Stelzer, *Quantitative in vivo imaging of entire embryos with Digital Scanned Laser Light Sheet Fluorescence Microscopy*. Current Opinion in Neurobiology, 2008. **18**(6): p. 624-632.

196. Wu, Y., et al., *Inverted selective plane illumination microscopy (iSPIM) enables coupled cell identity lineaging and neurodevelopmental imaging in Caenorhabditis elegans*. Proceedings of the National Academy of Sciences, 2011. **108**(43): p. 17708-17713.
197. Holekamp, T.F., D. Turaga, and T.E. Holy, *Fast three-dimensional fluorescence imaging of activity in neural populations by objective-coupled planar illumination microscopy*. Neuron, 2008. **57**(5): p. 661-672.
198. Swoger, J., et al., *Multi-view image fusion improves resolution in three-dimensional microscopy*. Optics express, 2007. **15**(13): p. 8029-8042.
199. Verveer, P.J., et al., *High-resolution three-dimensional imaging of large specimens with light sheet-based microscopy*. Nature methods, 2007. **4**(4): p. 311-313.
200. Fahrbach, F.O., et al., *Rapid 3D light-sheet microscopy with a tunable lens*. Optics Express, 2013. **21**(18): p. 21010-21026.
201. Dunsby, C., *Optically sectioned imaging by oblique plane microscopy*. Opt. Express, 2008. **16**(25): p. 20306-20316.
202. Bouchard, M.B., et al., *Swept confocally-aligned planar excitation (SCAPE) microscopy for high-speed volumetric imaging of behaving organisms*. Nat Photon, 2015. **advance online publication**.
203. Keller, P.J., F. Pampaloni, and E.H.K. Stelzer, *Life sciences require the third dimension*. Current Opinion in Cell Biology, 2006. **18**(1): p. 117-124.
204. Keller, Philipp J. and Misha B. Ahrens, *Visualizing Whole-Brain Activity and Development at the Single-Cell Level Using Light-Sheet Microscopy*. Neuron, 2015. **85**(3): p. 462-483.
205. Mickoleit, M., et al., *High-resolution reconstruction of the beating zebrafish heart*. Nature methods, 2014.
206. Trivedi, V., et al., *Dynamic structure and protein expression of the live embryonic heart captured by 2-photon light sheet microscopy and retrospective registration*. Biomedical Optics Express, 2015. **6**(6): p. 2056-2066.
207. Gualda, E.J., et al., *OpenSpinMicroscopy: an open-source integrated microscopy platform*. Nature methods, 2013. **10**(7): p. 599-600.
208. Gualda, E.J., et al., *SPIM-fluid: open source light-sheet based platform for high-throughput imaging*. Biomedical Optics Express, 2015. **6**(11): p. 4447-4456.
209. Pitrone, P.G., et al., *OpenSPIM: an open-access light-sheet microscopy platform*. Nat Meth, 2013. **10**(7): p. 598-599.
210. Gourdie, R.G., S. Kubalak, and T. Mikawa, *Conducting the Embryonic Heart: Orchestrating Development of Specialized Cardiac Tissues*. Trends in Cardiovascular Medicine, 1999. **9**(1–2): p. 18-26.
211. Sedmera, D., *Form follows function: developmental and physiological view on ventricular myocardial architecture*. European Journal of Cardio-Thoracic Surgery, 2005. **28**(4): p. 526-528.
212. Kamino, K., *Optical approaches to ontogeny of electrical activity and related functional organization during early heart development*. Physiological Reviews, 1991. **71**(1): p. 53-91.

213. Rentschler, S., et al., *Visualization and functional characterization of the developing murine cardiac conduction system*. *Development*, 2001. **128**(10): p. 1785-1792.
214. Hirota, A., et al., *Early events in development of electrical activity and contraction in embryonic rat heart assessed by optical recording*. *The Journal of Physiology*, 1985. **369**(1): p. 209-227.
215. Argüello, C., et al., *Electrophysiological and ultrastructural study of the atrioventricular canal during the development of the chick embryo*. *Journal of Molecular and Cellular Cardiology*, 1986. **18**(5): p. 499-510.
216. Kamino, K., et al., *Functional pacemaking area in the early embryonic chick heart assessed by simultaneous multiple-site optical recording of spontaneous action potentials*. *The Journal of General Physiology*, 1988. **91**(4): p. 573-591.
217. Rothenberg, F., et al., *Emerging patterns of cardiac conduction in the chick embryo: Waveform analysis with photodiode array-based optical imaging*. *Developmental Dynamics*, 2005. **233**(2): p. 456-465.
218. Salameh, A., K. Blanke, and I. Daehnert, *Role of connexins in human congenital heart disease: the chicken and egg problem*. *Front Pharmacol*, 2013. **4**: p. 70.
219. Kirchhoff, S., et al., *Abnormal cardiac conduction and morphogenesis in connexin40 and connexin43 double-deficient mice*. *Circ Res*, 2000. **87**(5): p. 399-405.
220. Sedmera, D., et al., *Optical Mapping of Electrical Activation in the Developing Heart*. *Microscopy and Microanalysis*, 2005. **11**(03): p. 209-215.
221. Pennisi, D.J., et al., *Induction and patterning of the cardiac conduction system*. *International Journal of Developmental Biology*, 2002. **46**(6): p. 765-775.
222. Filas, B.A., I.R. Efimov, and L.A. Taber, *Optical Coherence Tomography as a Tool for Measuring Morphogenetic Deformation of the Looping Heart*. *The Anatomical Record: Advances in Integrative Anatomy and Evolutionary Biology*, 2007. **290**(9): p. 1057-1068.
223. Männer, J., *Cardiac looping in the chick embryo: A morphological review with special reference to terminological and biomechanical aspects of the looping process*. *The Anatomical Record*, 2000. **259**(3): p. 248-262.
224. Ainsworth, S.J., R.L. Stanley, and D.J. Evans, *Developmental stages of the Japanese quail*. *J Anat*, 2010. **216**(1): p. 3-15.
225. Wang, Y.T., et al., *Optical Stimulation Enables Paced Electrophysiological Studies in Embryonic Hearts*. *Biomedical optics Express (In preparation)*, 2014.
226. Kroon, D.J. and C.H. Slump. *MRI modalitiy transformation in demon registration*. in *Biomedical Imaging: From Nano to Macro, 2009. ISBI '09. IEEE International Symposium on*. 2009.
227. Rueckert, D., et al., *Nonrigid registration using free-form deformations: application to breast MR images*. *Medical Imaging, IEEE Transactions on*, 1999. **18**(8): p. 712-721.
228. Sutherland, I.E., R.F. Sproull, and R.A. Schumacker, *A Characterization of Ten Hidden-Surface Algorithms*. *ACM Comput. Surv.*, 1974. **6**(1): p. 1-55.

229. Hu, Z. and A. Rollins, *Quasi-telecentric optical design of a microscope-compatible OCT scanner*. Optics Express, 2005. **13**(17): p. 6407-6415.
230. Bayly, P.V., et al., *Estimation of conduction velocity vector fields from epicardial mapping data*. Biomedical Engineering, IEEE Transactions on, 1998. **45**(5): p. 563-571.
231. Kaufman, M.H., *The atlas of mouse development*. Vol. 428. 1992: Academic press London.
232. Adams, D., et al., *Bloomsbury report on mouse embryo phenotyping: recommendations from the IMPC workshop on embryonic lethal screening*. Disease Models & Mechanisms, 2013. **6**(3): p. 571-579.
233. Polo-Parada, L., X. Zhang, and A. Modgi, *Cardiac cushions modulate action potential phenotype during heart development*. Developmental Dynamics, 2009. **238**(3): p. 611-623.
234. Christoffels, V.M. and A.F.M. Moorman, *Development of the Cardiac Conduction System: Why Are Some Regions of the Heart More Arrhythmogenic Than Others?* Circulation: Arrhythmia and Electrophysiology, 2009. **2**(2): p. 195-207.
235. Singh, R., et al., *Tbx2 and Tbx3 induce atrioventricular myocardial development and endocardial cushion formation*. Cellular and Molecular Life Sciences, 2012. **69**(8): p. 1377-1389.
236. Ford, B.D., J.A. Loeb, and G.D. Fischbach, *Neuregulin Stimulates DNA Synthesis in Embryonic Chick Heart Cells*. Developmental Biology, 1999. **214**(1): p. 139-150.
237. Milan, D.J., et al., *Notch1b and neuregulin are required for specification of central cardiac conduction tissue*. Development, 2006. **133**(6): p. 1125-1132.
238. Benson, D.W., *Genetics of atrioventricular conduction disease in humans*. The Anatomical Record Part A: Discoveries in Molecular, Cellular, and Evolutionary Biology, 2004. **280A**(2): p. 934-939.
239. Ma, P., et al., *Three-dimensional correction of conduction velocity in the embryonic heart using integrated optical mapping and optical coherence tomography*. Journal of Biomedical Optics, 2014. **19**(7): p. 076004-076004.
240. Kolega, J., *Phototoxicity and photoinactivation of blebbistatin in UV and visible light*. Biochemical and Biophysical Research Communications, 2004. **320**(3): p. 1020-1025.
241. Herron, T.J., P. Lee, and J. Jalife, *Optical Imaging of Voltage and Calcium in Cardiac Cells & Tissues*. Circulation Research, 2012. **110**(4): p. 609-623.
242. Swoger, J., F. Pampaloni, and E.H.K. Stelzer, *Light-Sheet-Based Fluorescence Microscopy for Three-Dimensional Imaging of Biological Samples*. Cold Spring Harbor Protocols, 2014. **2014**(1): p. pdb.top080168.
243. Stelzer, E.H.K., *Light-sheet fluorescence microscopy for quantitative biology*. Nat Meth, 2015. **12**(1): p. 23-26.
244. Keller, P.J., M.B. Ahrens, and J. Freeman, *Light-sheet imaging for systems neuroscience*. Nat Meth, 2015. **12**(1): p. 27-29.
245. Baker, L.C., et al., *Effects of mechanical uncouplers, diacetyl monoxime, and cytochalasin-D on the electrophysiology of perfused mouse hearts*. American

- Journal of Physiology - Heart and Circulatory Physiology, 2004. **287**(4): p. H1771-H1779.
246. Sonka, M. and J.M. Fitzpatrick. *Handbook of medical imaging(Volume 2, Medical image processing and analysis)*. 2000. SPIE- The international society for optical engineering.
  247. Control, C.f.D. and Prevention, *Update on overall prevalence of major birth defects--Atlanta, Georgia, 1978-2005*. MMWR. Morbidity and mortality weekly report, 2008. **57**(1): p. 1.
  248. Kirby, M.L., K.L. Turnage, and B.M. Hays, *Characterization of conotruncal malformations following ablation of "cardiac" neural crest*. The Anatomical Record, 1985. **213**(1): p. 87-93.
  249. Kirby, M.L. and D.E. Bockman, *Neural crest and normal development: A new perspective*. The Anatomical Record, 1984. **209**(1): p. 1-6.
  250. Kirby, M.L. and K.L. Waldo, *Role of neural crest in congenital heart disease*. Circulation, 1990. **82**(2): p. 332-40.
  251. Tomita, H., et al., *Relation of early hemodynamic changes to final cardiac phenotype and survival after neural crest ablation in chick embryos*. Circulation, 1991. **84**(3): p. 1289-95.
  252. Franz, T., *Persistent truncus arteriosus in the Splotch mutant mouse*. Anatomy and Embryology, 1989. **180**(5): p. 457-464.
  253. Dal-Bianco, J.P., et al., *Basic Mechanisms of Mitral Regurgitation*. Canadian Journal of Cardiology, 2014. **30**(9): p. 971-981.
  254. Enriquez-Sarano, M., et al., *Echocardiographic prediction of survival after surgical correction of organic mitral regurgitation*. Circulation, 1994. **90**(2): p. 830-837.
  255. Enriquez-Sarano, M., et al., *Valve repair improves the outcome of surgery for mitral regurgitation a multivariate analysis*. Circulation, 1995. **91**(4): p. 1022-1028.
  256. Plein, A., A. Fantin, and C. Ruhrberg, *Chapter Six - Neural Crest Cells in Cardiovascular Development*, in *Current Topics in Developmental Biology*, A.T. Paul, Editor. 2015, Academic Press. p. 183-200.
  257. Besson, W.T., et al., *Effects of the size of lesions of the cardiac neural crest at various embryonic ages on incidence and type of cardiac defects*. Circulation, 1986. **73**(2): p. 360-4.
  258. Jain, R., et al., *Cardiac neural crest orchestrates remodeling and functional maturation of mouse semilunar valves*. The Journal of clinical investigation, 2011. **121**(1): p. 422.
  259. Nomura-Kitabayashi, A., et al., *Outflow tract cushions perform a critical valve-like function in the early embryonic heart requiring BMPRIA-mediated signaling in cardiac neural crest*. American Journal of Physiology - Heart and Circulatory Physiology, 2009. **297**(5): p. H1617-H1628.
  260. Karunamuni, G.H., et al., *Connecting teratogen-induced congenital heart defects to neural crest cells and their effect on cardiac function*. Birth Defects Research Part C: Embryo Today: Reviews, 2014. **102**(3): p. 227-250.

261. Stewart, D.E., M.L. Kirby, and K.K. Sulik, *Hemodynamic changes in chick embryos precede heart defects after cardiac neural crest ablation*. *Circulation Research*, 1986. **59**(5): p. 545-50.
262. Vermot, J., et al., *Reversing blood flows act through *klf2a* to ensure normal valvulogenesis in the developing heart*. *PLoS biology*, 2009. **7**(11): p. e1000246.
263. Li, Y.-X., et al., *Cardiac neural crest in zebrafish embryos contributes to myocardial cell lineage and early heart function*. *Developmental Dynamics*, 2003. **226**(3): p. 540-550.
264. Karunamuni, G.H., et al., *Capturing structure and function in an embryonic heart with biophotonic tools*. *Frontiers in Physiology*, 2014. **5**.
265. Kuwajima, T., et al., *ClearT: a detergent-and solvent-free clearing method for neuronal and non-neuronal tissue*. *Development*, 2013. **140**(6): p. 1364-1368.
266. Jenkins, M.W., *Imaging the Embryonic Heart with Optical Coherence Tomography*. 2008, Case Western Reserve University.
267. Kirby, M.L., et al., *Backtransplantation of chick cardiac neural crest cells cultured in LIF rescues heart development*. *Developmental Dynamics*, 1993. **198**(4): p. 296-311.
268. Waldo, K.L., D. Kumiski, and M.L. Kirby, *Cardiac neural crest is essential for the persistence rather than the formation of an arch artery*. *Developmental Dynamics*, 1996. **205**(3): p. 281-292.
269. Kirby, M.L., *Nodose placode contributes autonomic neurons to the heart in the absence of cardiac neural crest*. *The Journal of neuroscience*, 1988. **8**(4): p. 1089-1095.
270. Bellairs, R. and M. Osmond, *Atlas of chick development*. 2005: Academic Press.
271. Männer, J., W. Seidl, and G. Steding, *Experimental study on the significance of abnormal cardiac looping for the development of cardiovascular anomalies in neural crest-ablated chick embryos*. *Anatomy and Embryology*, 1996. **194**(3): p. 289-300.
272. S Basu, P., H. Elsebaie, and M. Noordeen, *Congenital Spinal Deformity: A Comprehensive Assessment at Presentation*. *Spine*, 2002. **27**(20): p. 2255-2259.
273. Liu, Y.-t., et al., *A retrospective study of congenital scoliosis and associated cardiac and intraspinal abnormalities in a Chinese population*. *European Spine Journal*, 2011. **20**(12): p. 2111-2114.
274. Combs, M.D. and K.E. Yutzey, *Heart valve development regulatory networks in development and disease*. *Circulation research*, 2009. **105**(5): p. 408-421.
275. Clouthier, D.E., et al., *Cranial and cardiac neural crest defects in endothelin-A receptor-deficient mice*. *Development*, 1998. **125**(5): p. 813-824.
276. Kirby, M.L., *Cellular and molecular contributions of the cardiac neural crest to cardiovascular development*. *Trends in cardiovascular medicine*, 1993. **3**(1): p. 18-23.
277. Stottmann, R.W., et al., *BMP receptor IA is required in mammalian neural crest cells for development of the cardiac outflow tract and ventricular myocardium*. *Development*, 2004. **131**(9): p. 2205-2218.

278. Hinton, R.B. and K.E. Yutzey, *Heart valve structure and function in development and disease*. Annual review of physiology, 2011. **73**: p. 29.
279. Phoon, C.K.L., et al., *Embryonic Heart Failure in NFATc1<sup>-/-</sup> Mice: Novel Mechanistic Insights From In Utero Ultrasound Biomicroscopy*. Circulation Research, 2004. **95**(1): p. 92-99.
280. Fishman, M.C. and K.R. Chien, *Fashioning the vertebrate heart: earliest embryonic decisions*. Development, 1997. **124**(11): p. 2099-2117.
281. Beis, D., et al., *Genetic and cellular analyses of zebrafish atrioventricular cushion and valve development*. Development, 2005. **132**(18): p. 4193-4204.
282. Butcher, J.T., et al., *Transitions in early embryonic atrioventricular valvular function correspond with changes in cushion biomechanics that are predictable by tissue composition*. Circulation research, 2007. **100**(10): p. 1503-1511.
283. Hove, J.R., et al., *Intracardiac fluid forces are an essential epigenetic factor for embryonic cardiogenesis*. Nature, 2003. **421**(6919): p. 172-177.
284. Groenendijk, B.C.W., et al., *Changes in Shear Stress-Related Gene Expression After Experimentally Altered Venous Return in the Chicken Embryo*. Circulation Research, 2005. **96**(12): p. 1291-1298.
285. Reckova, M., et al., *Hemodynamics Is a Key Epigenetic Factor in Development of the Cardiac Conduction System*. Circulation Research, 2003. **93**(1): p. 77-85.
286. Heckel, E., et al., *Oscillatory Flow Modulates Mechanosensitive *klf2a* Expression through *trpv4* and *trpp2* during Heart Valve Development*. Current Biology, 2015. **25**(10): p. 1354-1361.
287. Scherz, P.J., et al., *High-speed imaging of developing heart valves reveals interplay of morphogenesis and function*. Development, 2008. **135**(6): p. 1179-1187.
288. Auman, H.J., et al., *Functional modulation of cardiac form through regionally confined cell shape changes*. PLoS biology, 2007. **5**(3): p. e53.
289. Shu, X., et al., *Na<sup>+</sup> K-ATPase is essential for embryonic heart development in the zebrafish*. Development, 2003. **130**(25): p. 6165-6173.
290. Ford, S. *Altering Hemodynamics in Early Heart Development with Optical Pacing Leads to Congenital Heart Defects*. in 2014 AAP National Conference and Exhibition. 2014. American Academy of Pediatrics.
291. Karunamuni, G., et al., *Using optical coherence tomography to rapidly phenotype and quantify congenital heart defects associated with prenatal alcohol exposure*. Developmental Dynamics, 2014.
292. Hogers, B., et al., *Unilateral Vitelline Vein Ligation Alters Intracardiac Blood Flow Patterns and Morphogenesis in the Chick Embryo*. Circulation Research, 1997. **80**(4): p. 473-481.
293. Armstrong, E.J. and J. Bischoff, *Heart Valve Development: Endothelial Cell Signaling and Differentiation*. Circulation Research, 2004. **95**(5): p. 459-470.
294. Peterson, L.M., et al., *Orientation-independent rapid pulsatile flow measurement using dual-angle Doppler OCT*. Biomedical optics express, 2014. **5**(2): p. 499-514.
295. Chow, B.Y., et al., *High-performance genetically targetable optical neural silencing by light-driven proton pumps*. Nature, 2010. **463**(7277): p. 98-102.